AN ABSTRACT OF THE THESIS OF

Joshua P. Herrera for the degree of Master of Science in Radiation Health Physics presented on May 15, 2018.

Title: Human Eye Dosimetry: Air Gap Analysis by Shield Placement and Photon Energy

Abstract approved:

David M. Hamby

Abstract:

When the ICRP updated their recommended limits for eye dose, they ignited a renewed interest in eye dosimetry. Especially, how the updated eye dose estimates affect current regulations and what that would mean to a radiation worker. Radiation workers are commonly required to wear leaded eyeglasses to reduce their dose to the eyes, especially the lens. However, it was unknown if additional shield placements in front of the leaded eyeglasses would result in additional protection factors over additive expectation. The goal of this study was to use a comprehensive deterministic eye model to analyze how dose to the lens of the eye would change as shielding placement changes. Stationary shields were designed to mimic a user wearing eyeglasses, and dynamic shields were placed in various positions in front of the stationary shield. With each shield placement iteration, the photon energy and shield thickness were changed from 0.25 MeV through 2.5 MeV with additional iterations with 0.662 MeV, 1.173 MeV and 1.332 MeV. The dose to the unshielded lens is compared to the dose of the lens with both shields, stationary and dynamic, to calculate a protection factor. Another protection factor was calculated but the dose to the eye was compared between the stationary shield and both the stationary and dynamic shield. These two protection factors were then compared to each other to determine the influence of shield positioning in front of the eye.

Human Eye Dosimetry: Air Gap Analysis by Shield Placement and Photon Energy

by
Joshua P. Herrera

A THESIS

submitted to

Oregon State University

in partial fulfillment of
the requirements for the
degree of

Master of Science

Presented May 15, 2018
Commencement June 2018

Master of Science thesis by Joshua P. Herrera presented on May 15, 2018.

APPROVED:

____

Major Professor, representing Radiation Health Physics

____

Head of the School of Nuclear Science and Engineering

____

Dean of the Graduate School

I understand that my thesis will become part of the permanent collection of Oregon State University libraries. My signature below authorizes release of my thesis to any reader upon request.

____

Joshua P. Herrera, Author

ACKNOWLEDGEMENTS

There were several people that helped me complete this research. I would like to express my gratitude to my advisor Dr. Hamby. His instruction, guidance, and knowledge of the subject provided the perfect compass for which I set my goals. I would also like to thank David Boozer. Even though he is a LT in the Navy, he was an invaluable source in helping me with MCNP coding and modeling the head and eye. Finally, I would like to thank Ian Trakowski. He was a great friend and sounding block for me to discuss ideas and collaborate with during the planning, execution, and writing of this paper.

TABLE OF CONTENTS

TABLE OF CONTENTS (CONTINUED)

Page

LIST OF FIGURES

LIST OF TABLES

LIST OF APPENDICIES

LIST OF APPENDIX FIGURES

LIST OF APPENDIX FIGURES (CONTINUED)

LIST OF APPENDIX FIGURES (CONTINUED)

Figure Page

LIST OF APPENDIX TABLES

DEDICATION

This work is dedicated to my beautiful wife Mallory, my daughter Vivienne, and my son Jameson.

Human Eye Dosimetry: Air Gap Analysis by Shield Placement and Photon Energy

CHAPTER 1 – INTRODUCTION

1.1 Overview

Before the 1890s, the atom and its configuration was just a concept. Physicists pondered what could possibly be that small and how it played a role in chemistry and physics. However, as the discovery of individual particles helped them update the model of the atom, it also opened the door to the research of particle physics. In 1895, Wilhelm Roentgen discovered X-rays while experimenting with a cathode ray tube. He was able to create a simple image of his wife's hand using what he called X-rays (Chodos, 2018). Soon after his discovery, many physicists around the world duplicated his experiment and noticed an immediate usefulness in the medical profession. J.J. Thompson discovered the electron in 1897. Ernest Rutherford concluded that radiation could be divided into two types, alpha and beta rays, in 1899. In 1900, Pierre Curie observed and recorded gamma rays for the first time (Sutton, 2017). With the discovery of new particles and their fascinating use, the dangers of such particles, in an era before exposure limits, quickly became a realization. The discovery of these particles is the discovery of ionizing radiation. These pioneers in physics knew little about the dangers of their experiments, and as a result used little to no shielding. Some lost their lives as a direct result of exposing themselves to high levels of radiation. Madam Curie is a great example: the notebook she used over 100 years ago is still radioactive today (Tasch, 2015).

Years later, much is known about particle interactions, but physicists are still trying to grasp the concepts of how radiation affects the body. One of the most radiosensitive portions of the body is the eyes, especially the lens (Hamada, 2016). In 2007, the ICRP published recommendations in Publication 103, but they still did not consider any changes to the lens dose, which was previously 50-200 rad. (ICRP, 2007). In 2011, they issued a statement updating their recommendation for the absorbed dose threshold for the lens to be 50 rad for occupational exposure. They changed the equivalent dose for occupational workers from 15 rem per year to 2.0 rem per year averaged over five consecutive years and 5.0 rem in any single year. They did not update their exposure limit for the public. The limit remained the same at 1.5 rem per year (ICRP, 2007). Since many nations base their exposure limits off these recommendations, it is important to understand the implications of these changes, especially when concerned about cataracts.

The most economical way to limit eye exposure and decrease the possibility of cataracts is shielding. Lead equivalent eye protection and shields are often used (Anastasian, 2011). This shielding is intended to provide a level of protection from energies typically seen in a lab or medical environment. It is important to know the best radiation protection factor while using lead equivalent eye protection and other forms of shielding when concerned about eye dosimetry. Knowing the protection factor for a given shielding configuration will allow users to update their standard operating procedures to achieve a higher protection factor.

Creating a comprehensive deterministic eye model will allow researchers to model the eye with precision and simulate particles of different types and energies interacting with it. The source particles of concern are electrons, photons, neutrons, protons, alpha particles, and heavy charged particles. The energy of an alpha particle required to penetrate the dead layer of skin (0.007 cm) is about 10 MeV. That energy is well above the normal energies typically seen in a laboratory setting. Since the energy of an alpha particle required to penetrate the dead layer of skin is so high, the assumption can be made that the energies of heavy charged particles will also be very high. Therefore, alpha particles, heavy charged particles, and protons are not considered in this comprehensive model. However, electrons, neutrons, and photons are capable of contributing significant dose to the eye and be found in laboratory settings. While other researchers may focus their efforts on modeling the comprehensive deterministic model of the eye with electrons and neutrons, this paper will focus on mono-energetic photons and their contributions to lens dose.

1.2 Research Objectives

Traditionally, the shield placement of multiple shields of the same material should not affect the dose to a target on the opposite side of a source. However, this study seeks to determine if there is a difference in shield placement and how that might affect the dose to the lens of a human eye. The objectives of this research are: 1) to investigate how shielding scenario variables, such as shield thickness and distance between shields, affect the performance of radiation shielding; and 2) to develop a method to quantify the overall protection factor for different eye shield characteristics. These objectives will be addressed with computer simulations of several eye shield scenarios using MCNP6.

CHAPTER 2 – BACKGROUND

2.1 Eye Anatomy

The eyes are the organs of the human body that convert light into electrical pulses and send those signals to the brain for interpretation ("The Human Eye", 2018). The size of each eye varies from person to person, but they average about 24mm in diameter and weigh about 8 grams (Snell, 1998). The eye is primarily comprised of the retina, choroid, sclera, vitreous humor, optic nerve, iris, cornea, and the lens as shown in Figure 1. Of the components of the eye, the lens is the most radiosensitive and must be protected.

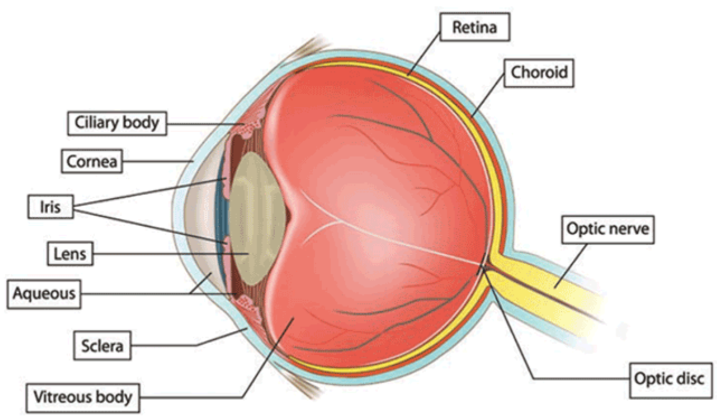

Figure 1: Eye Anatomy ("Eye Anatomy",2017)

The lens is located in the anterior hemisphere of the eye, behind the cornea and iris and is surrounded by the aqueous humor (anterior) and vitreous body (posterior) (Ainsbury, 2016). The lens is elastic and transparent, which allows it to focus on objects near and far. The lens also has its own particular anatomy. In Figure 2, the lens epithelium is divided into four areas of concern: the central zone (CZ), the germinative zone (GZ), the transitional zone (TZ), and the meridional rows (MR). This division is based on the different types of cell populations that exist in the epithelium. The CZ is essentially non-mitotic, while the GZ is the main site of mitotic activity. The equatorial cells are the progeny of the GZ. After cell division occurs, the epithelial cells differentiate and form the MR (Nogueira, 2011). This anatomy is important in the transparency of the lens.

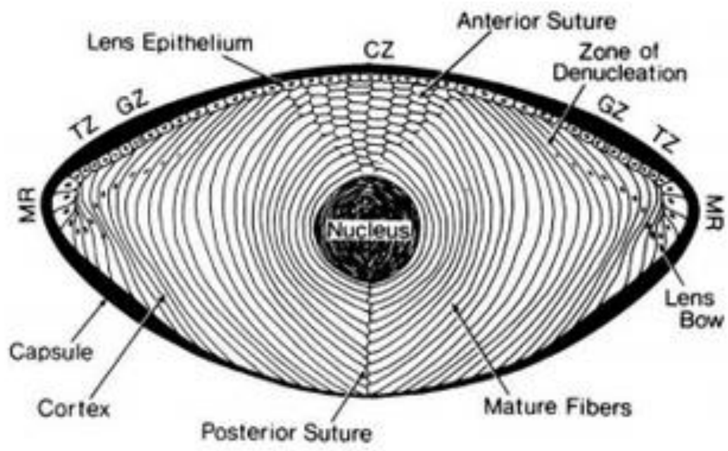

Figure 2: Lens Anatomy (Nogueira, 2011)

2.2 Cataracts

The main concern with radiation dose to the eye is cataractogenesis or the formation of cataracts. A cataract is a clouding of what is normally a clear lens of the eye (Hall, 2012, p. 188). While cataracts may result from aging, injury, or disease, high levels of ionizing radiation can be the cause as well (IAEA, Radiation Protection of Medical Staff from Cataract, 2017). There are three main forms of cataracts: cortical, nuclear, and posterior sub-capsular (PSC). Each form is based on their anatomical location. Cortical cataracts occur in the cortex portion of the lens. Nuclear cataracts occur in the nucleus. And posterior sub-capsular occurs underneath the back portion of the lens. Ionizing radiation is generally, but not exclusively, associated with posterior sub-capsular and sometimes cortical opacities (IAEA, Radiation Protection of Medical Staff from Cataract, 2017).

The lens consists largely of fiber cells and is covered with an epithelium anteriorly. When a cell divides, it is limited to the pre-equitorial region of the epithelium. Cell division occurs throughout life, however, there is no mechanism for cell removal. If dividing cells are injured by radiation, the abnormal fibers are not removed from the lens. Instead, they migrate toward the posterior pole. Since they are not translucent, they begin to form a cataract (Hall, 2012, p. 188). The best way to prevent cataracts from ionizing radiation is by using shielding. Shielding limits the fluence of incident particles and decreases the possibility of cellular damage, which in this case is cataractogenesis.

2.3 Photon Interactions

Photons interact with matter in a different manner than charged particles. There are three major mechanisms in which photons interacts with matter: photoelectric effect, Compton scatter, and pair production. A consequence of these interactions is that as the photons interact with matter the individual photons are removed from the beam. Thus, the beam energy does not degrade over the medium, but the intensity of the beam falls exponentially as shown in Equation 1.

$$I = I_0 e^{-\mu x} \qquad \text{Equation 1}$$

In Equation 1, I_o is the initial photon intensity, and I is the photon intensity after traveling through a material of linear attenuation coefficient (μ) and thickness x. The linear attenuation coefficient is the sum of the probabilities for photoelectric effect (τ), Compton scatter (σ), and pair production (κ) per unit path length in the absorber. The linear attenuation coefficient is the measure of a photon that will be removed from the beam by one of these mechanisms as shown in Equation 2 (Knoll, 2000, p. 53). Using lead, which has a high linear attenuation coefficient, the final photon fluence after traveling through a material will be much less than the initial.

$$\mu = \tau\ (Photoelectric\ Effect) + \sigma\ (Compton\ Scatter) + \kappa\ (Pair\ Production) \qquad \text{Equation 2}$$

In the photoelectric effect, or photoelectric absorption, an incoming photon is completely absorbed by a target's atomic electron. The interaction results in ionization by subsequent ejection of the electron from the atom. The energy of the liberated electron is the difference between the photon energy and the binding energy of the electron as shown in Equation 3.

$$KE_e = h\nu - BE_e \qquad \text{Equation 3}$$

In Equation 3, KE_e is the kinetic of the liberated electron, $h\nu$ is the energy of the incident photon, and BE_e is the binding energy of the target electron. As the electrons rearrange, the atom will emit characteristic X-rays or auger electrons. If the resulting photoelectron has sufficient kinetic energy, it may be a source of secondary ionizations occurring along its trajectory (Meroli, "The Interaction of Photons with Matter").

If the incident photon is of high enough energy compared to the binding energy, then Compton scatter may occur. Compton scatter, also known as incoherent scatter, scatters an electron away in conjunction with a new photon of lower energy of the incident photon. The kinetic energy of the scattered electron is shown in Equation 4 and the energy of the scattered photon is shown in Equation 5.

$$KE_e = \frac{\alpha\,(1-\cos\theta)}{1+\alpha(1-\cos\theta)}\ ;\ where\ \alpha = {}^{h\upsilon}\!/_{0.511\text{ MeV}} \qquad \text{Equation 4}$$

$$h\upsilon' = h\upsilon\frac{1}{1+\alpha(1-\cos\theta)}\ ;\ where\ \alpha = {}^{h\upsilon}\!/_{0.511\text{ MeV}} \qquad \text{Equation 5}$$

In Equations 4 and 5, KE_e is the kinetic energy of the scattered electron, $h\upsilon$ is the energy of the incident photon, $h\upsilon'$ is the energy of the scattered photon, and θ is the photon scatter angle relative to the path of the incident photon. Analyzing Equation 5, the two extreme angles of the scattered photon occurs when $\theta = 0°$ and $\theta = 180°$. The scattered electron's kinetic energy is maximized when the photon scatter angle is $180°$. Similar to the photoelectric effect, if the scattered secondary photon is of high enough energy it can go on to cause additional interactions within the medium.

At energies above 1.022 MeV, pair production becomes an additional form of photon interaction. In lead, pair production becomes the dominate form for photon interaction at energies above 5 MeV (Hubbell, 1969, Table 3-22). In pair production, the photon experiences a Coulombic interaction with an electron or nucleus producing a positron-electron pair. The kinetic energy transferred to the two particles is shown in Equation 6.

$$\overline{E_{tr}^{k}} = hv - 1.022\ MeV \qquad \text{Equation 6}$$

In Equation 6, E_{tr}^{k} is the kinetic energy transferred to the positron-electron pair and hv is the energy of the incident photon. The two particles travel in the forward direction relative to the incident photon with roughly the same energy. The positron will attract the negative charge of a free electron. When the positron and free electron expel their kinetic energy, they will annihilate to form two annihilation photons. The two photons will travel in opposite directions, each with an energy of 511 keV. The photon interaction cross-sections for the lens of the eye are shown in Figure 3.

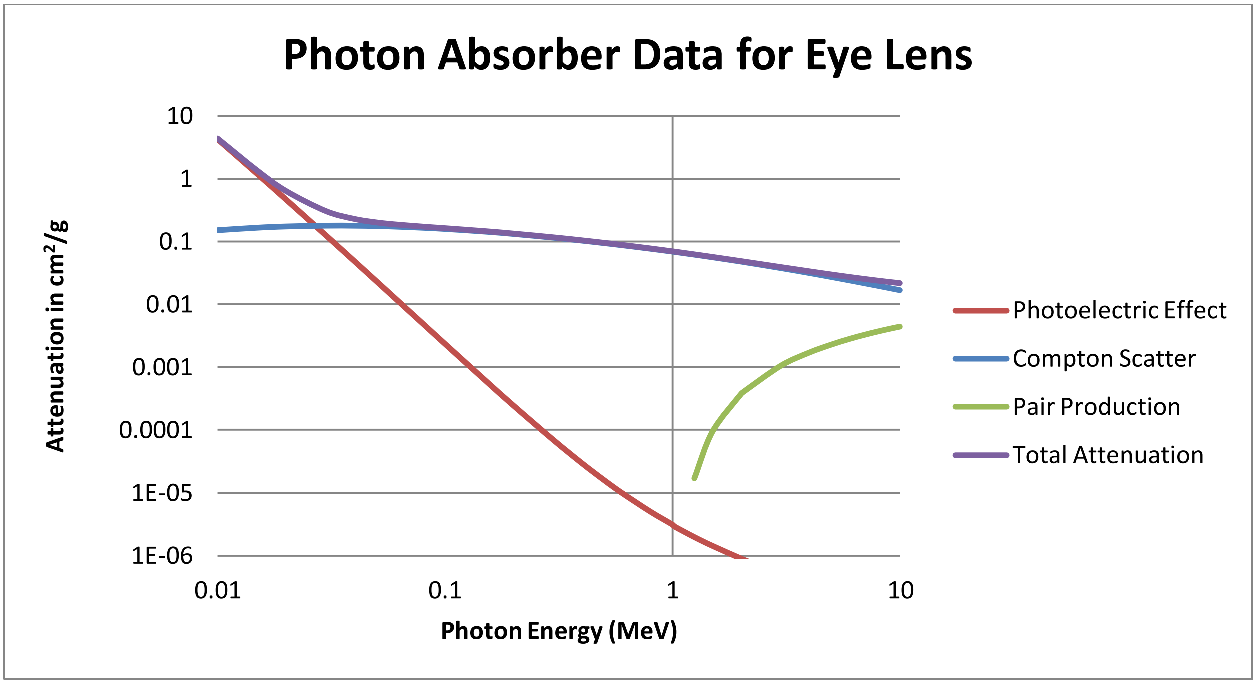

Figure 3: Photon Absorber Data for Eye Lens (Berger, 2005)

For the purpose of radiation protection from photons, the energy range for this study will be between 0.25 MeV and 2.5 MeV. Cesium-137 (Cs-137) is a common radionuclide from nuclear weapons testing and accidents. It emits a strong gamma ray of 0.662 MeV (Bentley, 2008, p. 1). Another common radionuclide found in medical and industrial settings is Cobalt-60 (Co-60). Co-60 radiates two strong gamma rays of 1.173 MeV and 1.332 MeV (Healy, 2017). Over these energy ranges and in tissue, photoelectric effect and Compton scatter dominate with pair production possible with energies greater than 1.022MeV. Photoelectric effect and Compton scatter will account for most of the reactions that lead to lens dose.

2.4 Photon Dosimetry and Shielding

In order to protect the lens of the eye from ionizing radiation, one must first understand the importance of how radiation is delivered to the lens and how to shield those photons. Absorbed dose is the quotient of mean energy imparted by ionizing radiation to the matter of unit mass (Shultis, 2008, p. 260). For photons, dose can be calculated by using Equation 13.

$$D = \varphi \, E \left(\frac{\mu_{ab}}{\rho}\right) \qquad \text{Equation 13}$$

In Equation 13, φ is the photon fluence, E is the photon energy, and $\left(\frac{\mu_{ab}}{\rho}\right)$ is the mass energy absorption coefficient (Shultis, 2008, p. 260). The mass energy absorption coefficient is the product of the mass energy transfer coefficient and (1-g) where g is the fraction of the energy of secondary charged particles that is lost to Bremsstrahlung in the material. The mass energy absorption coefficient is dependent on Z of the material and the photon energy. It is dependent on Z because μ, the linear attenuation coefficient, is related to the number of atoms in a cubic cm of material and the probability of a photon interaction with the nucleus or an electron (Shultis, 2008, p. 182). Therefore, as Z increases, and density increases, the linear attenuation coefficient does as well since there will be more atoms to attenuate a beam of photons.

The photoelectric absorption and Compton scatter also dictates the percentage of photons shielded. The probability of an interaction for photoelectric absorption increases with Z and decreases with photon energy. Compton scatter begins to dominate at higher energies. Since the energies used in this study will be between 0.25 MeV and 2.5 MeV, the photoelectric effect will dominate as the most probable photon interaction (Figure 4). The best shielding against photoelectric effect is high Z materials because of the electron density. Therefore, the shielding assumed for this study will be lead doped eyeglasses and plates.

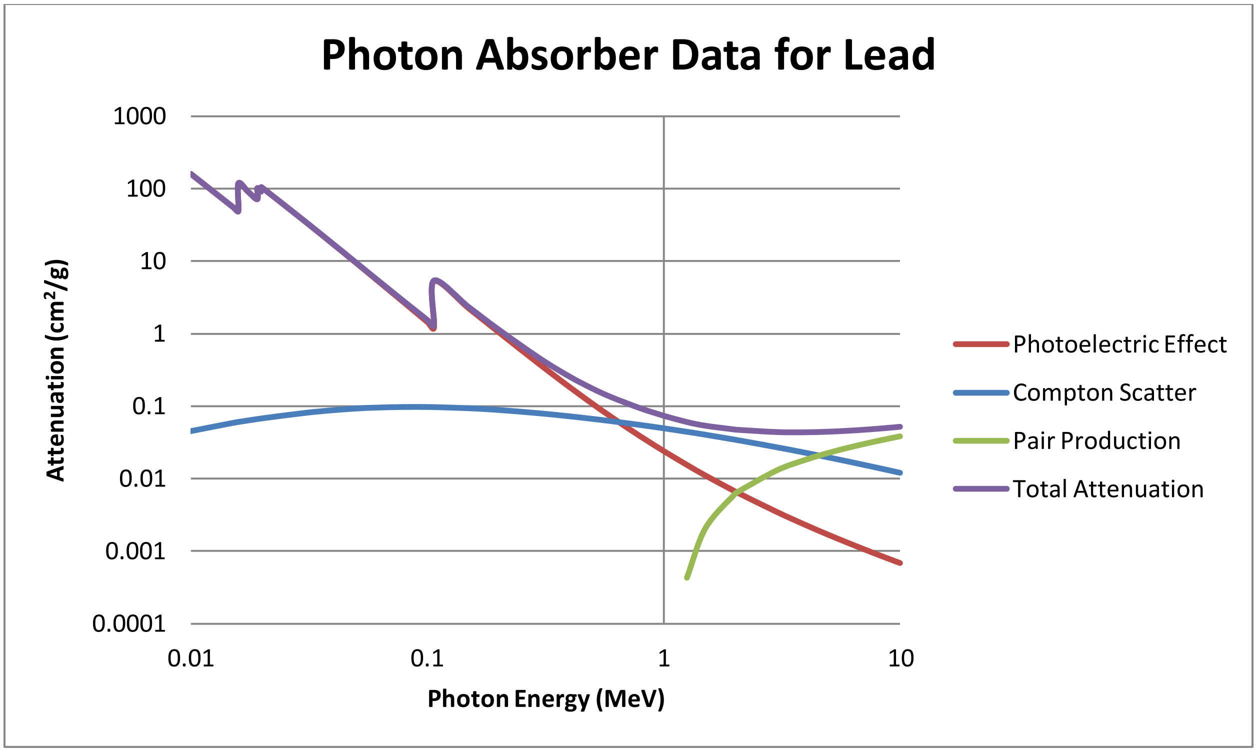

Figure 4: Photon Absorber Data for Lead (Berger, 2005)

2.5 Charged Particle Equilibrium

KERMA is the sum of all kinetic energy liberated by uncharged ionizing particles in matter as shown in Equation 7.

$$K = \varphi E \left(\frac{\mu_{tr}}{\rho}\right) \quad \text{Equation 7}$$

In Equation 7, φ is the photon flux, E is the energy of the photon, and $\left(\frac{\mu_{tr}}{\rho}\right)$ is the mass energy transfer coefficient. The mass energy transfer coefficient is defined as the ratio of the particles that transfer kinetic energy to charged particles by interaction while traveling an incremental distance divided by the density, ρ, of the material. Just like dose, the units of KERMA are joules per kilogram. However, KERMA is not measured in Grays. Charged particle equilibrium (CPE) exists for a small incremental volume, where every charged particle leaving the volume, another of the same type, energy, and direction replaces it. If CPE exists at a point, then dose is equal to KERMA and the losses due to Bremsstrahlung are negligible. The relationship between dose and KERMA is shown in Figure 5.

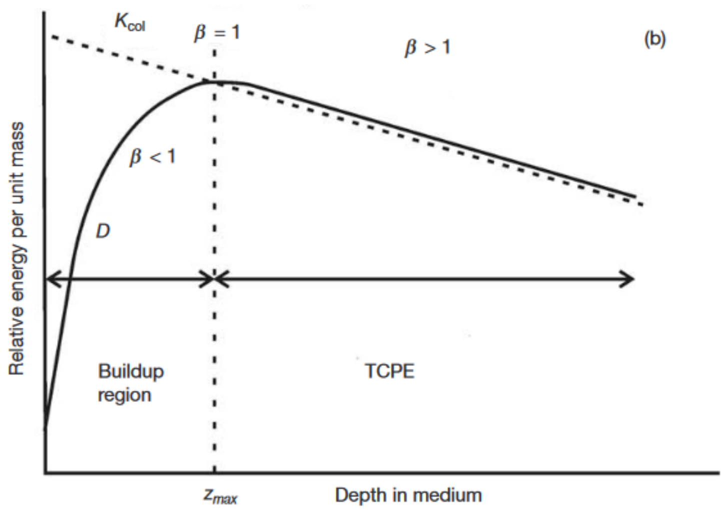

Figure 5: Buildup Region and CPE (Seuntjens, 2005, p. 59)

In Figure 5, dose is equal to KERMA where $\beta = 1$. At that point, CPE is established. The depth of the medium where this occurs is the range of an electron in that medium for a given energy. If a 1 MeV photon interacted with tissue by the photoelectric effect, it will result in a 1 MeV photoelectron because the energy of the incident photon is much larger than the binding energy of the electron. The range of a 1 MeV electron in tissue is about 0.4 cm. The depth of interest is 0.3 cm for the lens. Therefore, the 0.3 cm portion of the eye is still in the buildup region. This creates complications since most dose calculations assume CPE is established. However, using NUREG/CR-6918 Version 2, "VARSKIN 5: A Computer Code for Skin Contamination Dosimetry", Hamby et al formulated an equation to calculate the percentage of KERMA to estimate the dose in the buildup region (Hamby, 2014). Their value, f_{cpe} , which is the same as β from Figure 5, is shown in Equations 8, 9, 10, 11, and 12.

$$D = Kf_{CPE} \qquad \text{Equation 8}$$

$$f_{CPE}(x) = \frac{1}{a + bln(x) + {}^{c}/_{\sqrt{x}}} \qquad \text{Equation 9}$$

$$a = 19.78 + 0.1492Eln(E) - 0.008390E^{1.5} + 0.00003624E^2 + 3.343\sqrt{E}\ln(E) - {}^{10.72E}/_{\ln(E)}$$

$$b = 1.217x10^{-12}E^4 - 5.673x10^{-9}E^3 + 7.942x10^{-6}E^2 - 0.002028E + 0.3296$$

$$c = 9.694x10^{-13}E^4 - 4.861x10^{-9}E^3 + 7.765x10^{-6}E^2 - 0.001856E + 0.1467$$

Above, *x* (cm) is a function of energy and is equal to the point kernel distance between source point and dose point, and the coefficients *a*, *b*, and *c* are functions of energy (keV) (Hamby, 2014). Regarding dosimetry to the eye, *x* is equal to 0.3 cm. Using f_{CPE}, this report will estimate dose at 0.3cm in the eye using KERMA and f_{CPE}.

2.6 The Bragg Curve

When traveling through a medium, charge particles do not evenly deposit their energy until it comes to rest. Instead, charged particles deposit their energy with increasing depth until about the end of the track length it deposits a large quantity before coming to rest. (Figure 6).

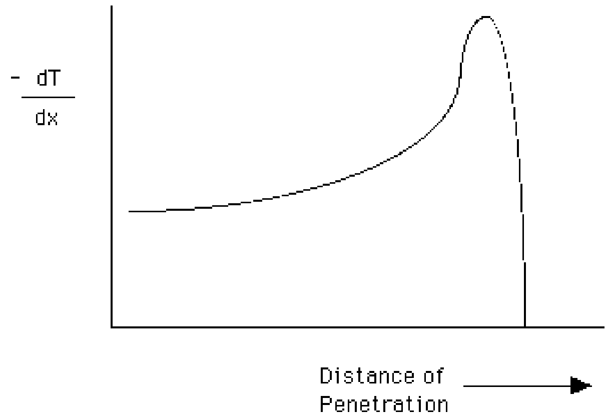

Figure 6: Bragg Curve (Wagenaar, 1995)

The Bragg curve shown in Figure 6 is ubiquitous of an alpha particle of several MeV. $-\frac{dT}{dx}$ is the differential energy loss for a particular particle within the material divided by the corresponding differential path length, also known as specific energy loss. For a majority of the track length, the specific energy loss increases roughly as 1/E. As the particle nears the end of its track, the charge is reduced through electronic pickup and the curve falls off (Knoll, 2000).

Electrons exhibit energy loss in a similar fashion but the Bragg peak is not as pronounced. The energy deposition of the electron increases more slowly with penetration distance. Electrons experience a more tortuous path than heavy charged particles and deposit their energy due to radiative and collisional losses. However, electrons do exhibit a Bragg peak but the peak occurs when the electron energy has been reduced to less than about 1 keV, and it accounts for only a small fraction of its total energy (Wagenaar, 1995).

2.7 Leaded acrylic and glass shielding

Leaded glasses and acrylics are the most practical way to shield a radiographer from exposure to the lens of the eye. Leaded glasses are doped with a small percentage of lead to create a lead thickness equivalent.

The typical lead thickness equivalent is 0.75 mm. That means when photons pass through the eyewear they will be attenuated the same as if they passed through a 0.75 mm sheet of lead. The benefit of using leaded glass versus leaded acrylic is that it will provide the same shielding properties as the leaded acrylic but will be about 5 times thinner.

CHAPTER 3 – MATERIALS AND METHODS

3.1 Software and Computing

3.1.1 MCNP

Eye exposure simulations were performed using a Monte Carlo code that was developed and is maintained by the Los Alamos National Laboratory. MCNP is a general-purpose, continuous-energy, generalized-geometry, time-dependent, Monte Carlo radiation-transport code designed to track many particle types over broad ranges of energies (MCNP6, 2013, p. 1-1). It can model particle transport across a wide range of energies, materials, and geometries. For photons, the code accounts for incoherent and coherent scattering, the possibility of fluorescent emission after photoelectric absorption, and absorption in electron-positron pair production. For electrons and positron transport, it can account for the angular deflection through multiple Coulomb scattering, collisional energy loss with optional straggling, and the production of secondary particles including K-shell X-rays, knock-on and Auger electrons, Bremsstrahlung, and annihilation gamma rays from positron annihilation at rest. Monte Carlo simulation software relies on a random number generator to determine an output based on the input probabilities. In any given MCNP run, particles are generated from a user-defined source and the software tracks them throughout their lifetime in the defined universe. Any secondary particles that are created from interactions are also tracked within the system.

In order to run an MCNP simulation, the user must create an input file. The input file defines all the parameters the user wants to define within MCNP. The input file is comprised of surface, cell, and data cards with additional cards available that allow the user to do specific functions. The surfaces (planes, spheres, cones, cylinders, etc.) listed in the surface card create the basis for which the user can define specific cells. MCNP uses a Cartesian coordinate system on which the surfaces are placed. The cell card uses the surfaces and their senses to define a closed space or cell. Each surface divides all space into two regions, once with positive sense with respect to the surface and the other with negative sense (MCNP6, 2013, p. 3-3). If a sphere is defined as a surface, the inside of the sphere would have a negative sense and the outside of the sphere would have a positive sense. The data block defines additional data for the cells. It contains information about the materials used in the system, the source definition, tally locations, physics specifications, and several other useful features of MCNP. A tally is the opportunity for the user to request specific type of information from the simulation. It can be used to request surface current or energy distribution of pulses created in a simulated detector (MCNP6, 2013, p. 1-13).

To execute an MCNP file, the user needs to create a well-defined input file. For complex input files, it can take minutes, hours, or even days to run a simulation. Upon completion, MCNP generates several output files detailing the run. MCNP automatically checks the results of the run with ten statistical tests. The statistical checks speak to the precision of the estimated output. MCNP can deliver a myriad of various types of outputs like surface flux, surface current, track length, flux at a point, track length estimate of energy deposition, and energy distribution of pulses created in a simulated detector. These outputs can be used to determine dose in a wide range of energies and materials. There are multiple versions of MCNP available. For this study, MCNP6 was used.

3.1.2 Computing Demands

The length of time for an input file to run depends on the processing power of the computer, the complexity of the file, and the level of precision of the output desired. The computer specifications used for this study is 6GB of RAM and a model AMD FX 6120 Six-Core processor rated at 3.5 GHz per core. The speed and number of processors is important as it will greatly cut down on computational time and allow for greater precision in the same amount of time.

3.1.3 MCNP6 Plotter

The MCNP6 geometry plotter was used to plot 2D slices of a problem geometry specified in the input file. The plotter gives the user an invaluable tool to troubleshoot problems in specific geometries. The eye and head models in this study were plotted in the MCNP plotter to verify the proper geometries and to rectify any possible problems from the improper formatting of the geometry input. MCNP requires the use of an X-Windows server and, for the purpose of this study, MobaXterm Personal Edition v10.5 Build 3582 was used.

3.1.4 MCNP Visual Editor

MCNP Visual Editor is designed to help the user easily display geometries and create MCNP input files. The program allows the user an interactive means of creating an input file with the help of two or more dynamic cross sectional views of the model (Schwarz, 2011). Visual Editor uses the surfaces and cells from the input card to create a two-dimensional (2D) and three-dimensional (3D) plot of the geometry. This format allows the user to visualize the geometries and to make any necessary changes to the input file. All of the 3D plots used in this study were created in Visual Editor.

3.2 Simulation Geometry and Materials

3.2.1 Head and Eye Model

In order to compare the results to other studies, especially ones analyzing the ICRP’s change to lens dose limit, the model used in this study needed to be as physiologically accurate with a lens depth of 300 mg/cm^2. Eckerman et al (Eckerman, 1996) created a phantom model for Oak Ridge National Laboratory

(ORNL) in 1996, and Krstic et al (Krstic, 2006, "Input Files with ORNL") modeled the phantom in MCNP. The human body and all organs are represented with equations of 3D geometrical bodies. The eye model is based on the work of Nogueira et al (Nogueira, 2011). They created an eye model based on NCRP Report no. 130 (NCRP, 1999) and the eye model from Charles and Brown (Charles, 1975). The model gives additional detail to the various portions of the lens. By combining these two models, this study will use a unique head phantom with a high level of detail in the eyes.

3.2.2 Geometry and Materials of the Head

The head phantom code used in this study came from Krstic et al (Krstic, 2006, "External Doses in Humans", "Input Files with ORNL", 2007) from ORNL. They created a male and female phantom with anatomical organs for use in MCNP-4B. The ORNL phantom consisted of three sections: (1) the trunk and arms were represented as elliptical cylinders; (2) legs and feet were two truncated circular cones; and (3) the neck and head were represented with a circular cylinder on which another elliptical cylinder, covered by half an ellipsoid was situated. For this study, only the head and neck portion of the male phantom was used. There was no difference between the male and female phantom once the trunk and extremities were removed.

Based on the analytical models of the human body from ORNL publications, Krstic et al (Krstic, 2006 "Input Files with ORNL") used 3D geometrical bodies to form their equations for each individual organ. They also used inequalities to represent some organs. The coordinate system uses the z-axis as vertically upward, the y-axis and x-axis as horizontally directed to the posterior side and towards the left-hand side of the phantom, respectively. The head portion of the phantom contains 6 cells and 28 surfaces. The phantom is shown in Figure 7.

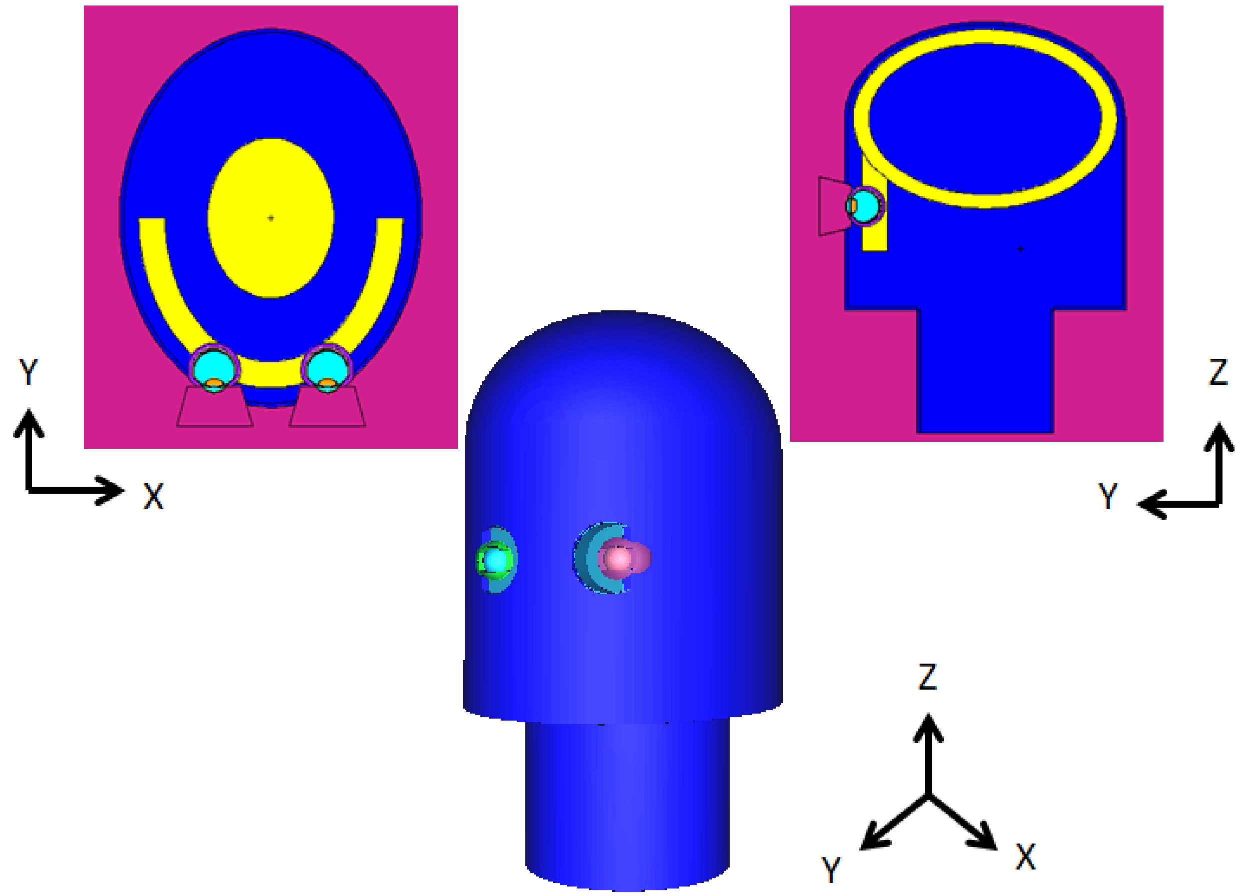

Figure 7: MCNP Model of the Phantom

Krstic et al (Krstic, 2006 “Input Files with ORNL”) validated their MCNP phantom model by comparing their data with ICRP 74 report. They calculated their own dose conversion factors as a function of photon energy in the range of 0.1 to 10 MeV for the liver, lung, and testes, and compared them with ICRP 74 (ICRP, 1996). The discrepancy between the model and ICRP 74 was larger in the lower energy region, below 1 MeV, where it reached 10%. If the energy was larger than 1 MeV, the difference was much smaller and in many cases less than 5%. They determined the model was in good agreement with ICRP 74. It is worth noting that the MIRD model used in ICRP 74 differs from the ORNL model by geometries and tissue densities.

3.2.3 Geometry and Materials of the Eyes

The geometry and materials of the eyes were taken from Nogueira et al (Nogueira, 2011). They based their eye model from Worgul (Worgul, 1991) and NCRP Report no 130 (NCRP, 1999). They created a detailed eye model including the cornea, lens, anterior chamber, sclera, choroid, retina, vitreous humour, macula, and optic nerve. The eye lid dimensions were taken from ICRP 89 (ICRP, 2002) model from Charles and Brown (Charles, 1975). With these dimensions, a model of the eye was developed by Nogueira et. al. as shown in Figure 8 (Nogueira, 2011). The eye model contains 13 cells and 33 surfaces. A few corrections were made to the equations listed in Figure 8 and can be found within the input file in Appendix F.

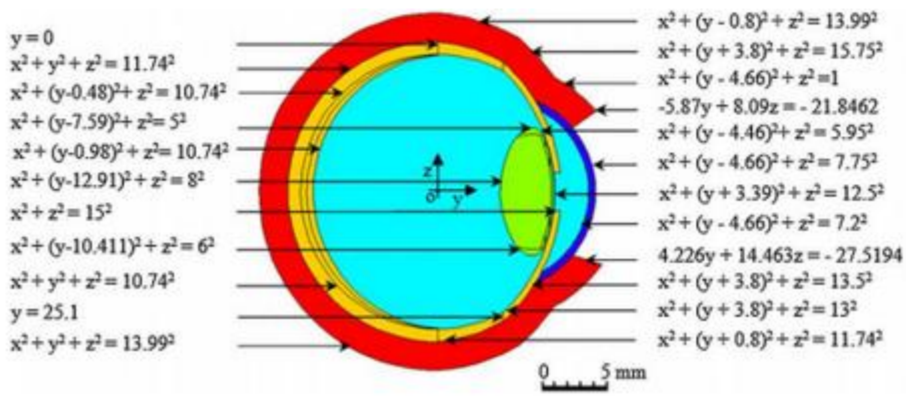

Figure 8: Nogueira et al Eye Model (Nogueira, 2011)

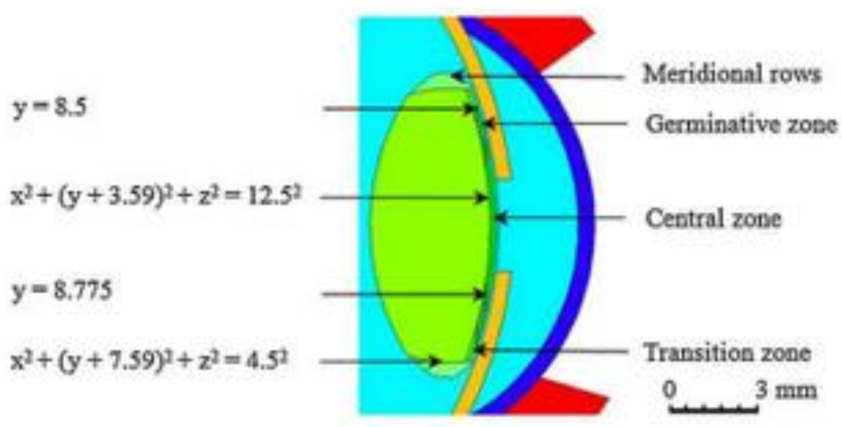

Figure 9: Close up view of lens regions by Nogueira et al (Nogueira, 2011)

Based on the regions of the lens from Figure 9, Nogueira et al (Nogueira, 2011) was able to model their lens with different epithelial cell populations: the central zone, the germanative zone, transitional zone, and the meridional rows (Figure 9). Based on the work from Merriam and Worgul (Merriam, 1983), the germanative zone is the primary site of cataract induction. Based on the equations provided by Nogueira et al (Nogueira, 2011), the MCNP model of the eye used in this study is shown in Figure 10. The view in the lower right quadrant of Figure 10 displays the Y/Z view of the eye and shows the target cell which is a sphere 0.3 cm deep into the eye.

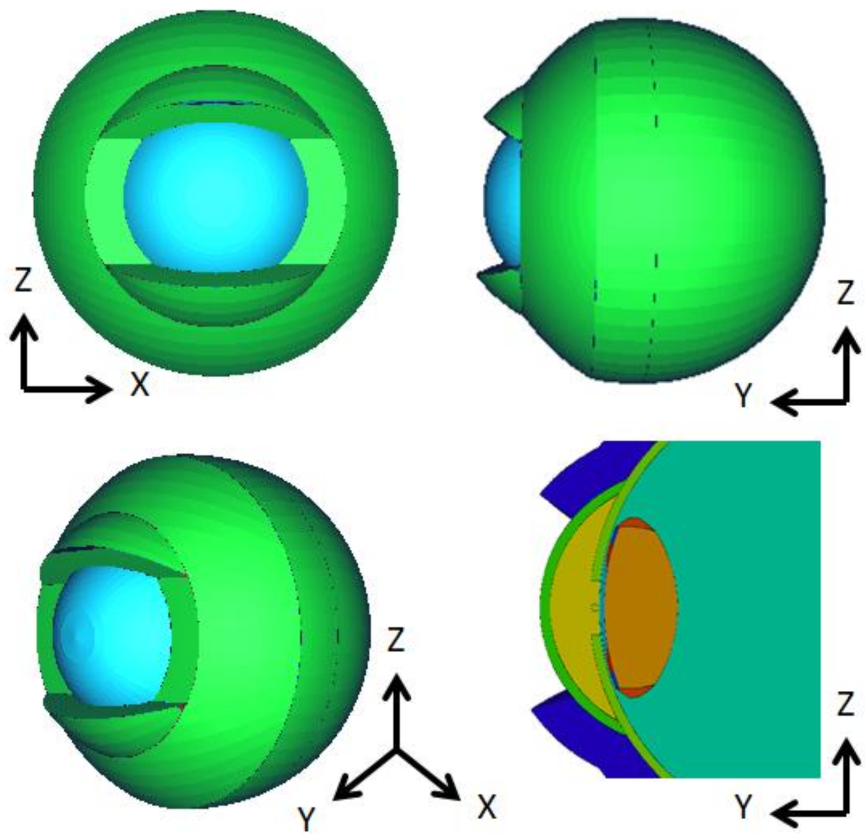

Figure 10: MCNP Eye Model Geometry

Table 1 displays the composition and density of the eye that this study used. They were taken from ICRP Publication 89 (ICRP, 2002), ICRP Publication 23 (ICRP, 1975), and ICRU Report 46 (ICRU, 1992). Since the target of concern is 300 mg/cm^2, or 0.3 cm, a cell was placed at that depth and will serve as the target for dose calculations.

Elemental Composition (% mass)											
Region	Density	H	C	N	O	Na	P	S	Cl	K	Color
Cornea	1.06	10.3	10.9	3.5	75.1			0.2			Dark Blue
Anterior Chamber	1.00	11.2			88.8						Light Blue
Lens	1.07	9.6	19.5	5.7	64.6	0.1	0.1	0.3	0.1		Green
Vitreous Humour	1.00	11.2			88.8						Light Blue
Retina and choroid	1.07	10.0	14.6	4.5	70.6			0.3			Orange
Sclera	1.07	10.0	14.6	4.5	70.6			0.3			Orange
Eye lid	1.09	10.0	19.9	4.2	65.0	0.2	0.1	0.2	0.3	0.1	Red

Table 1: Eye Composition and Densities (Nogueira, 2011)

3.3 Source Definition

3.3.1 Source Definition and Biasing

This study used mono-energetic photons for all of the MCNP runs. The energy range considered was 0.25 MeV to 2.5 MeV with runs completed for 0.25 MeV, 0.5 MeV, 0.662 MeV, 0.75 MeV, 1.0 MeV, 1.173 MeV, 1.332 MeV, 1.5 MeV, 1.75 MeV, 2.0 MeV and 2.5 MeV. The photons were emitted from a point source at a fixed point 25.0 cm in front of the phantom. Several biasing and variance reduction techniques were used in order to increase the probability of a photon interacting with the cells of interest without affecting the mean dose. First, the photons were forced to irradiate from the source in the shape of a cone in the direction of the phantom. This biasing was chosen to eliminate the unnecessary computation time of photons traveling in the opposite direction of the phantom and having a low probability of ever reaching the cells of interest. Second, weight windows were created using a mesh format to increase the importance of each photon (and resulting electrons) moving towards the cells of interest. Weight windows were used in conjunction with exponential transforms, which increase the distance between interactions and the probability that particles will travel farther through denser materials like lead.

The biasing of the source photons, without altering the results, was accomplished by altering their vector and direction. For this study, the photons are collimated into a cone along the y-axis towards the phantom. The SDEF card in the MCNP input file allows the user to modify the source term, particles, direction, and any biasing necessary for the problem. One of the SDEF cards used in this study is shown in Figure 11.

```
mode P E
SDEF  PAR=P ERG=0.75 POS 0 -25 0 VEC -3 24.059 0 DIR=D1    $ 5 degrees from (0,-25,0) to (-3,-.941,0)
SI1 -1.00 0.9961946981   1.00                              $ frac solid angle for each bin
SP1  0.00 0.998097349 0.001902650954                       $ source bias for each bin
SB1  0.00 0   1.00
```

Figure 11: SDEF Format

In the example SDEF card, the mode instructs MCNP to consider the interactions of primary photons and secondary electrons. The particles (PAR) emitted from the source were photons (P). Particle energies (ERG) were varied between 0.25 MeV and 2.5 MeV over multiple runs. The position of the source was located at (0, -25,0) which was 25.0 cm in front of the phantom and was level and centered between the eyes. In order to create the cone biasing, the input card needed to have the vector (VEC) and direction (DIR) modifiers added. The source information (SI1) modifier divides the histogram bin limits for the distribution. The bins range from -1 to 1 with a change of cos θ. The source probability (SP1) modifier defines the solid angle for the cone. The solid angles range from $\frac{1+\cos\theta}{2}$ to $\frac{1-\cos\theta}{2}$. The source biasing (SB1) modifier is 1 since each bin needs no bias. The results of this biasing for a point source 25 cm in front of the phantom's eyes radiated a cone of photons 5 degrees towards the phantom's right eye. Five degrees was used because it fully irradiated the right eye lens of the phantom while limiting the distribution of photons in unnecessary directions.

The MCNP6 weight window generator (WWG) was used to create a mesh around the phantom. Several iterations were utilized to create an appropriate mesh that increased the weights of particles traveling from the source point to the dose point. The dose point for this study is a 0.3 cm depth in the right eye. Once the mesh was created, the WWG could be turned off and the input altered for a specific energy and shield position. Weight windows, source biasing, and exponential transforms greatly reduced computational time needed to achieve reasonable relative errors when computing various tallies in MCNP6. Figure 12 shows the combination of source biasing and using weight windows for a 3 cm shield configuration. The color red depicts windows with a low weight. The blue windows contain a higher weight. So, a particle emitted from the source is rewarded for entering a window of higher weight which increases the probability that the particle will reach the target. If a particle enters a window of a lower weight, it is killed and MCNP will begin tracking a new particle.

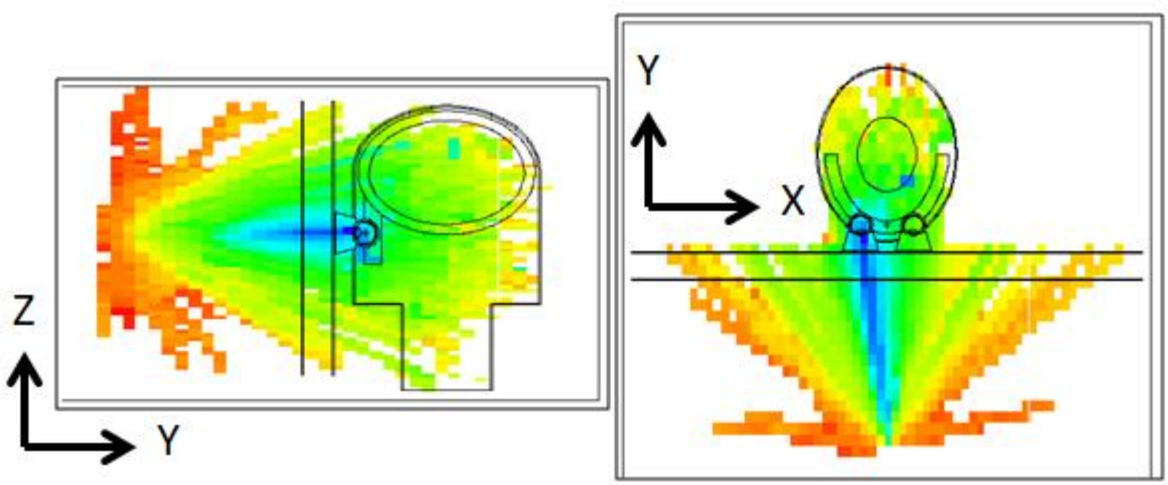

Figure 12: Source Biasing and Weight Windows with a 3 cm Dynamic Shield

3.4 MCNP6 Tallies

3.4.1 F5 Tally for the Lens

MCNP tallies are used to specify which result the Monte Carlo calculation will render. There are several tally types ranging from current across a surface to flux at a point. For the purpose of this study, an F5 tally was used. An F5 tally is a point "detector" tally and has units of particles per square centimeter. With an appropriate tally multiplier or dose energy/dose function (DE/DF) card, the F5 tally can calculate KERMA. The values of the DE/DF card are shown in Table 2.

Dose Energy (MeV)	DF	Dose Energy (MeV)	DF	Dose Energy (MeV)	DF	Dose Energy (MeV)	DF
0.01	7.43E-10	0.08	0.307E-10	0.6	2.84E-10	5.0	14.1E-10
0.015	3.12E-10	0.10	0.371E-10	0.8	3.69E-10	6.0	16.1E-10
0.02	1.68E-10	0.15	0.599E-10	1.0	4.47E-10	8.0	20.1E-10
0.03	0.712E-10	0.2	0.856E-10	1.5	6.14E-10	10.0	24.0E-10
0.04	0.429E-10	0.3	1.38E-10	2.0	7.55E-10		
0.05	0.323E-10	0.4	1.89E-10	3.0	9.96E-10		
0.06	0.289E-10	0.5	2.38E-10	4.0	12.1E-10		

Table 2: Dose Energy/Dose Function Values

The DE/DF card used in this study converts the F5 tally to Rads/Photon. MCNP uses the values in the DE/DF card and interpolates, for the necessary energies, the multiplication factor to convert the photon fluence to Joules/Kilogram or KERMA. Using Equation 8, the dose to the lens was estimated.

The region of interest is a cell located at a depth of 0.3 cm (300 mg/cm^2). Due to the geometry of the eye, the cell is located in the anterior chamber and not the lens itself. The Nuclear Regulatory Commission, NRC, defines lens dose at a depth of 0.3 cm, therefore, the target was maintained at a depth of 0.3 and not moved deeper into the eye where the lens is located (Standards for Protection Against Radiation, 2018). An F5 tally, or next event estimator, was chosen to calculate KERMA at a depth of 0.3 cm in the eye because an F5 tally does not rely on interactions within a given tally cell. The F5 tally considers all interactions and their probability to interact with the target cell. Since the target cell has a radius of only 0.02 cm, the probability a photon from 25 cm away interacting with it was very small. So, an F5 tally was chosen to estimate the KERMA at that depth.

3.5 Shield Design Methodology

3.5.1 Material of the Shields

Each shield was made of leaded glass. The material was defined in a Compendium of Material Composition Data (DHS, 2011) and its elemental constituents are given in Table 3. The Radiological Toolbox, Version 3.0 from Oak Ridge National Laboratory was used to determine the linear attenuation coefficients for the leaded glass (Table 3). Using the linear attenuation coefficients of leaded glass and elemental lead, the effective thickness of the glass was calculated for each photon energy and is shown in Table 4. Each leaded glass thickness will attenuate the same fraction of photons as a 0.075 cm thick slab of pure lead.

Leaded Glass Material Composition (% mass)	
Element	Weight Fraction
O	0.156453
Si	0.080866
Ti	0.008092
As	0.002651
Pb	0.751938

Table 3: Leaded Glass Material Composition and attenuation coefficient

Photon Energy (MeV)	Linear Attenuation Coefficient (cm^{-1})	Glass, Lead Thickness (cm)
0.1	25.203	0.1803
0.25	3.2384	0.1722
0.5	0.83472	0.1530
0.662	0.61738	0.1470
0.75	0.54373	0.1445
1	0.41586	0.1393
1.173	0.37206	0.1378
1.332	0.34154	0.1368
1.5	0.31759	0.1364
1.75	0.29905	0.1370
2	0.28052	0.1375
2.5	0.26604	0.1395

Table 4: Leaded Glass Shield Linear Attenuation Coefficients and Thickness

3.5.2 Shielding Scenarios for Comparison

For this study, several shield orientations were conducted in order to compare each to a configuration with no shield. The first standard simulation was the unshielded scenario where MCNP6 was executed without an eye shield defined in order to determine the dose to the cells of interest (the lens dose equivalent depth of 0.3 cm). Next, a leaded glass shield was modeled 2.3 cm in front of the phantom which is 2.6 cm in front of the 0.3 cm depth target cell in the eye. This distance was chosen to simulate a person wearing leaded glasses. The level of precision was chosen for the purposes of modeling the eye and shield in MCNP but actual distances may vary a few centimeters, as glasses tend to slip a little on the bridge of someone's nose. A second leaded glass shield was placed at various distances in front of the phantom and the stationary leaded glass eye shield. The distances used were 3, 5, 6, 7, 8, 9, 10, 11, 12, 13, 14, 15, 17, 19, and 20 cm in front of the first leaded glass shield as shown in Figure 13. The medium between the source, the shields, and the target is dry air near sea level (DHS, 2011).

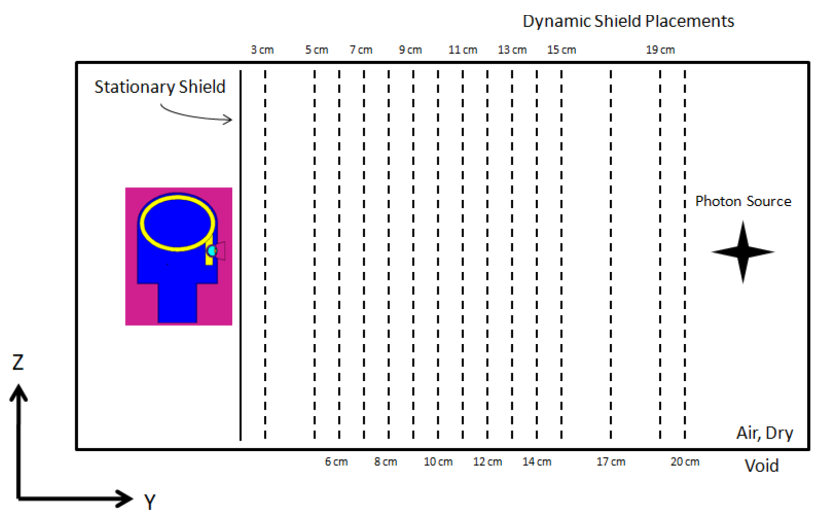

Figure 13: Shield Placements

3.6 Metrics for Shield Analysis

3.6.1 Protection Factor

In order to evaluate the shielding capabilities of each shield position, two different protection factors (PF) were calculated for each shield placement. The first protection factor (PF0) was calculated to be the ratio of the unshielded lens dose to the shielded lens dose, using both the stationary shield and dynamic shield. The second protection factor (PF1) was determined to be the ratio of the stationary shielded lens dose to the shielded lens dose, again, using both the stationary shield and dynamic shield. In all, fifteen dynamic shield placement distances in front of the stationary shield were used with each having two protection factors. These protection factors were chosen to compare the benefit of wearing leaded eye glasses to no shield versus a radiation worker wearing leaded eye-glasses and a standing behind a leaded panel to no shield. By comparing the outcome of the protection factors, one should be able to determine if shield placement has any affect on dose. While the point source used directional biasing towards the right eye, the dose to the left eye is assumed to be similar since the source was located equal distance between the eyes at a distance of 25 cm from the phantom. In addition, a weighted protection factor was not necessary because the location of the source and the location of the eye did not change. If the location of the source changed, then a weighted protection factor would be necessary to account for the fact that different source positions would contribute more lens dose to the total dose than other positions in the unshielded configuration.

CHAPTER 4- RESULTS AND DISCUSSION

4.1 No Shield

With the phantom unshielded from the source, the dose to the right eye is given in Table 5. Each dose located in Table 5 has a relative error less than 0.3%. The F5 tally from MCNP is an approximation of KERMA. Since the range of an electron with an energy of 0.25 MeV, 0.5 MeV, 0.662 MeV and 0.75 MeV is less than 0.3 cm, then the target at that depth has established CPE. However, for energies 1.0 MeV and greater, CPE has not been established at that depth. To correct the F5 tally for those energies, it was multiplied by f_{CPE} from Equation 9. The resulting product is eye dose (units of rad). For energies 0.25 MeV, 0.5 MeV, and 0.662 MeV KERMA will be used to approximate dose because CPE is already established. As the photon energy is increased from 0.25 MeV to 2.5 MeV the dose to the eye increases. This is because when the photons interact with matter, in this case air and the tissue of the eye, electrons are created by the three mechanisms discussed in Section 2.3. Those electrons will have higher energies and will be more penetrating, allowing them to deposit some or all of their energy at a depth of 0.3 cm resulting in a dose.

Unshielded Eye Dose			
Energy (MeV)	Dose (rad)	Energy (MeV)	Dose (rad)
0.25	1.59E-14	1.332	3.85E-14
0.5	3.29E-	1.5	3.79E-14
0.662	4.26E-14	1.75	3.61E-14
0.75	4.72E-14	2	3.37E-14
1	3.99E-14	2.5	2.54E-14
1.173	3.92E-14		

Table 5: Unshielded Dose to the Eye

4.2 Stationary Shield Configuration

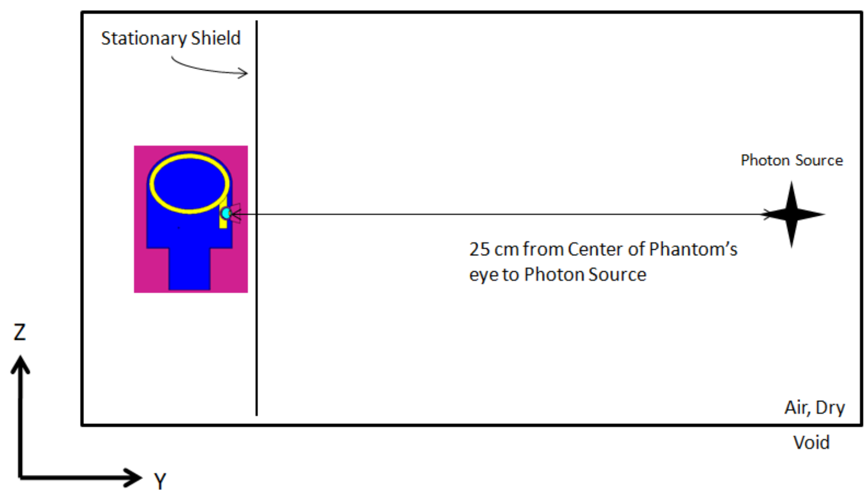

Figure 14: Stationary Shield Placement

With a single, stationary shield placed in front of the phantom (Figure 14), the dose to the right eye is calculated. Overall, the doses to the lens of the eye for each photon energy is lower (Table 6). The relative errors in Table 6 are all less than 0.3 %. This is expected because the leaded glass shield is attenuating photons decreasing the flux reaching the target depth of 0.3 cm and therefore decreasing the dose to that region.

Eye Dose with Stationary Shield			
Energy (MeV)	Dose (Rads)	Energy (MeV)	Dose (Rads)
0.25	1.02E-14	1.332	3.70E-14
0.5	2.88E-14	1.5	3.64E-14
0.662	3.91E-14	1.75	3.43E-14
0.75	4.41E-14	2	3.21E-14
1	3.81E-14	2.5	2.44E-14
1.173	3.75E-14		

Table 6: Dose to Eye with Stationary Shield

4.3 Dynamic Shield Placements

4.3.1 3 cm Shield Placement

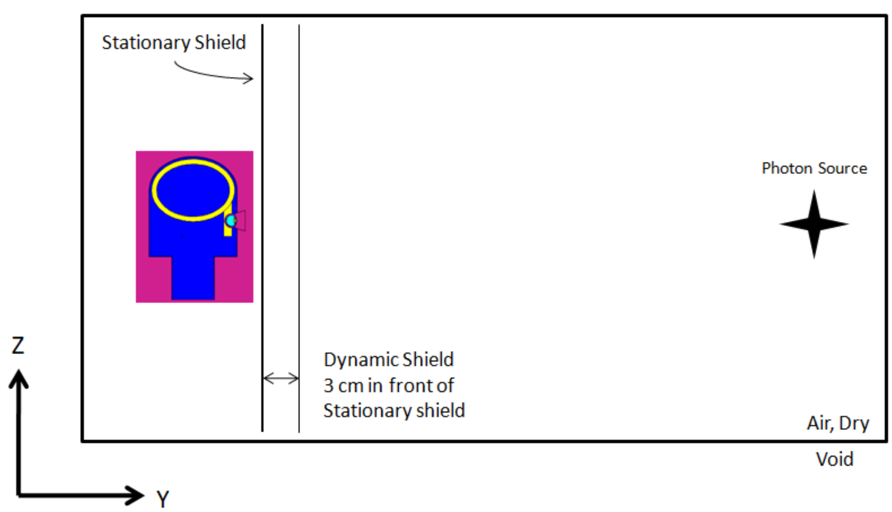

Figure 15: 3 cm Shield Placement

Figure 15 shows the placement of the first dynamic shield in front of the stationary shield. Dose as a function of energy for this shield placement is shown in Figure 16.

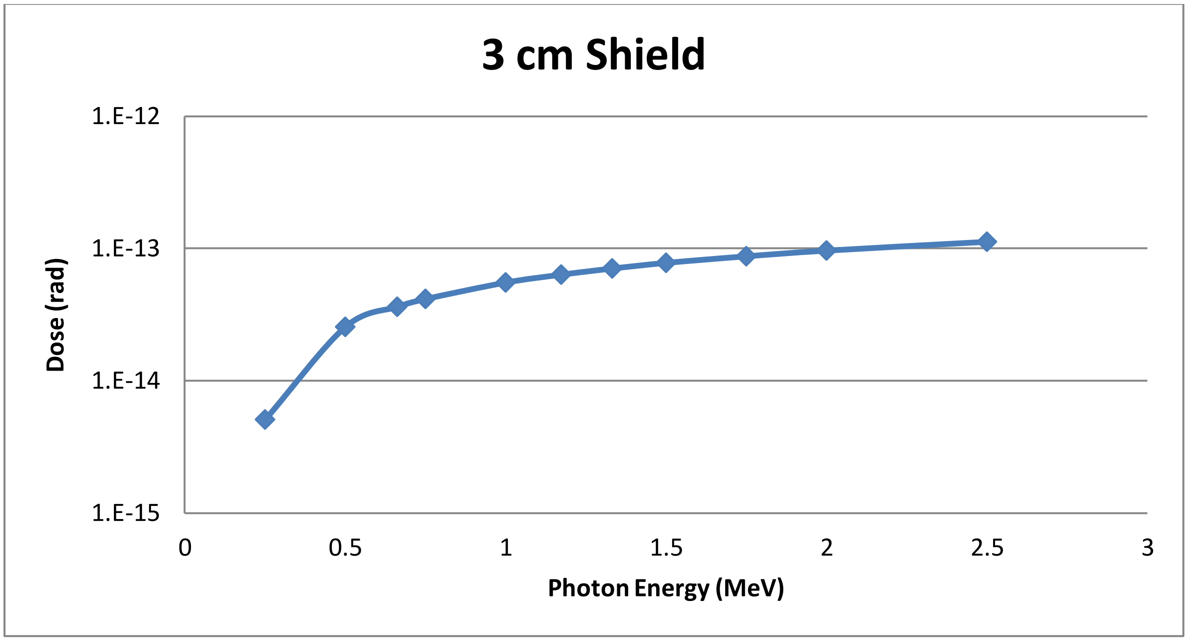

Figure 16: 3 cm Shield Placement Dose vs Energy Curve

As the photon energy increases from 0.25 MeV to 2.5 MeV the dose curve increases similar to a power function. This can be attributed to the relationship of mass attenuation coefficient to energy. Since Compton scatter is the dominate photon interaction mechanism for the energies used in this study, it is the dominate mechanism for the mass attenuation coefficient. Figure 17 follows a similar relationship because σ corresponds to the power rule, 1/E. As energy increases the shielding is becoming less effective. The relative error associated with this figure, and each subsequent dose to energy curve, are very small, equating to be about the width of the markers on the graph. Therefore, for each following shield placement the energy to dose curve will be placed in Appendix A and the table to accompany that curve will be placed in Appendix B. The relative errors for the tables in Appendix B are all less than 0.5 %.

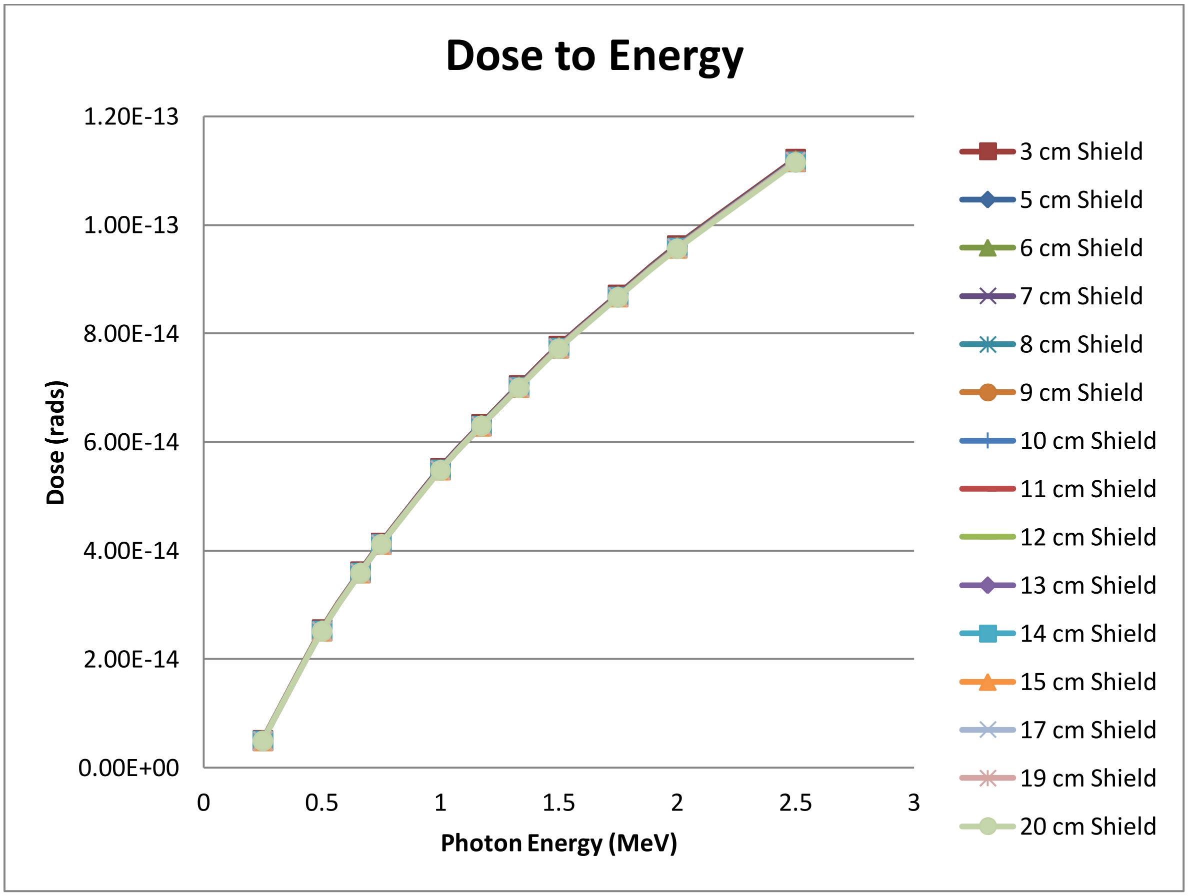

Figure 17: Energy to Dose Curve by Shield Placement

4.4 Shield Placement Analysis by Energy

Next, the dose resulting from a given shield placement was compared to various other shield placements for each iteration of photon energy. The eye dose by shield placement graph is shown in Figure 18 for photon energy of 0.25 MeV. Statistical error is shown as the upper and lower bars for each data point.

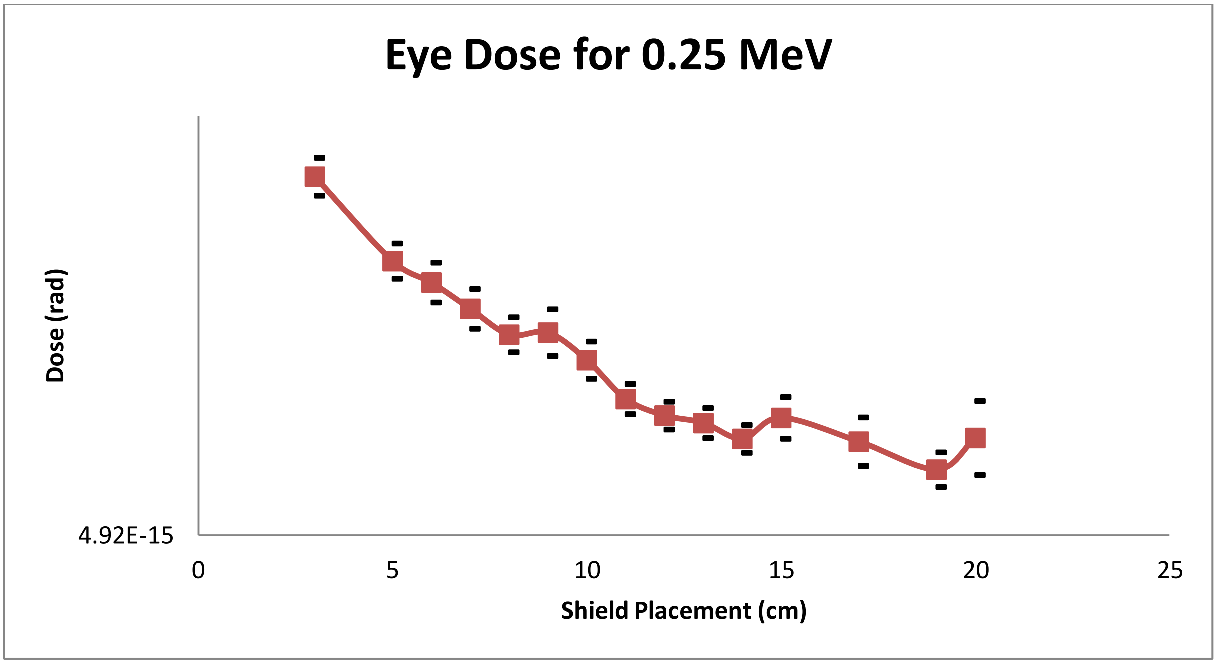

Figure 18: 0.25 MeV Photon Eye Dose

For each photon energy from 0.25 to 2.5 MeV, the dose to shield placement relationship demonstrates similar qualities. Dose for each energy decreases as the distance between the stationary shield and dynamic shield is increased. This is caused by the fact that as the dynamic shield is placed farther away from the target, the photons are scattered sooner, decreasing the overall fluence of photons reaching the target. When the dynamic shield is close to the stationary shield, the photons that are scattered have a higher probability of scattering towards the target than if the dynamic shield was placed closer to the source.

While there seems to be a relationship between shield placement and dose, the actual contribution from the shield placement is negligible. The difference between the dose with a 3 cm shield and a 20 cm shield for a 0.25 MeV photon only changes by 4.15E-06 rad/Ci. For dosimetric purposes, it is unlikely that a dose with that level of precision could be measured. The remaining dose to shield placement graphs are located in Appendix B.

4.5 Shield Protection Factors

Using the eye dose for each shield placement and photon energy, two protection factors were calculated. Figure 19 shows the two protection factors for a 3 cm shield configuration. When the photon interacts with the shield material it will likely undergo the photoelectric effect, Compton scatter, or pair production as discussed in Section 2.3. This will cause the secondary photon or electron to scatter, decreasing the probability it will reach the target, thus increasing the protection factor for that given energy. The protection factors for 0.25 MeV photons are about twice that of the other energies because an electron resulting from an interaction from this energy photon in leaded glass will not be able to penetrate the thickness of the shield. For a 0.25 MeV photon, the physical thickness of the leaded glass shield is 0.17 cm and the range of an electron created or liberated from a 0.25 MeV photon is 0.06 cm. This means that the electrons created or liberated on the surface of the shield will not be able to travel through the thickness of the shield. At energies greater than 0.5 MeV, the range of an electron is greater than the thickness of the shield. This means electrons can penetrate the shield thickness and possibly go on to deposit energy within the target cell resulting in a dose. This increase in the electron range slowly decreases the protection factor to unity (Figure 19). The fact that the protection factors remain constant after 0.75 MeV could be attributed to the Bragg curve. The depth of the target may be in the early region of the Bragg curve and have not reached the peak yet. If the target was deeper into the eye, around the range of an electron, the dose should be higher. The protection factors as a function of photon energy for each shield placement are shown in Appendix C.

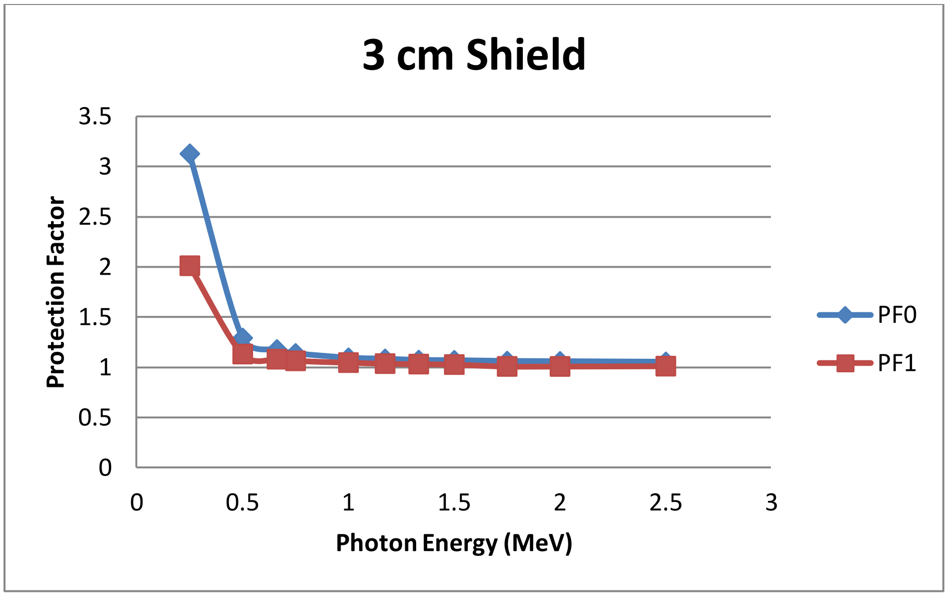

Figure 19: 3 cm Protection Factors by Energy

The protection factors, when compared to no shield (PF0), are higher than the protection factors compared to one shield (PF1) (Figure 20). This is expected because two leaded glass shields attenuate more photons than when compared to no shields. The difference between the protection factors for a 0.25 MeV photon is about 40 %. When compared to 2.5 MeV photons, the difference is even less (Figure 21).

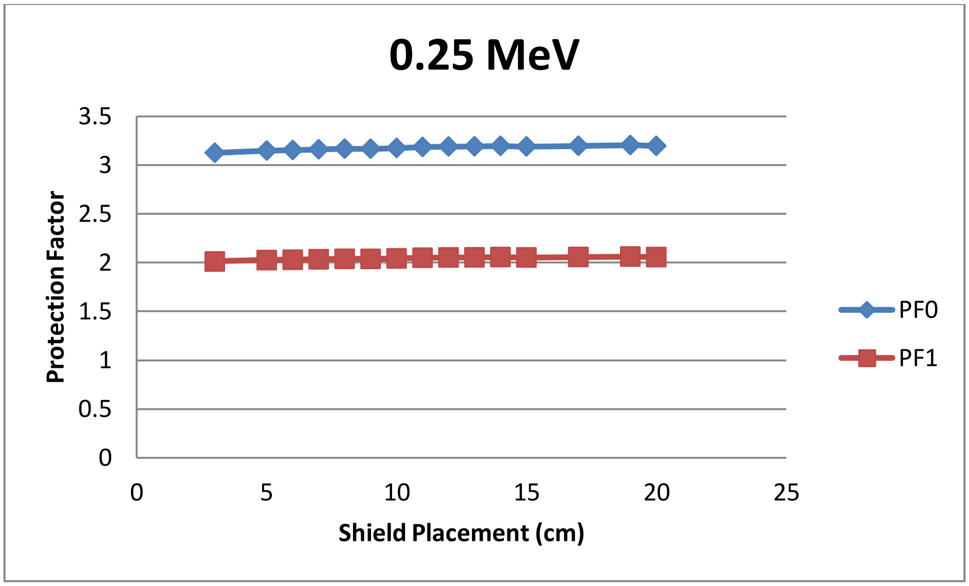

Figure 20: 0.25 MeV Photon Protection Factors by Shield Placement

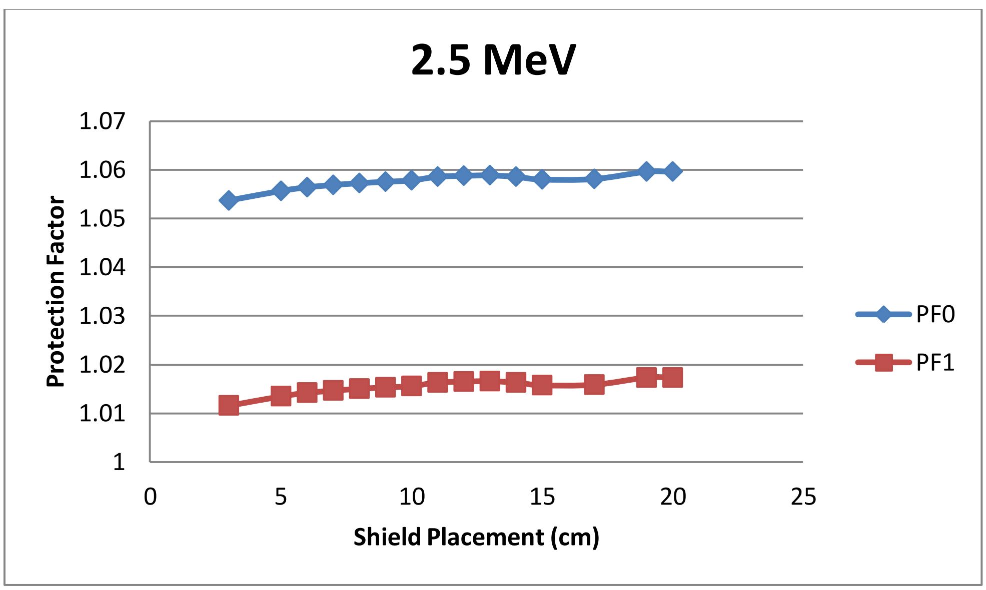

Figure21: 2.5 MeV Photon Protection Factors by Shield Placement

The difference between the protection factors in Figure 21 is about 5%. This can be attributed to the fact that high-energy photons are being attenuated very little by either leaded glass shields. This is related to the range of an electron created or liberated from high-energy photon interactions. These photons are less likely to interact with the shield material causing a fairly consistent fluence of photons reaching the eye regardless of shield placement or number of shields. The remaining protection factor to shield placement curves are located in Appendix D.

For both Figure 20 and 21, and each figure located in Appendix D, the protection faction slowly increases as shield placement is moved closer to the source. Traditional thinking believes that shield placement between a source and target should not affect the dose. However, by demonstrating that for each photon energy the protection faction slowly increases challenges that belief. The reason the protection factor increases may be due to the amount of scatter that is occurring when the photons are incident on the shield. If the shield is closer to the source, the scattered photons have a lower probability of reaching the target cell and thus decrease the chances it will contribute any energy to the target dose. Therefore, scatter does play a small part in how shield placement affects dose.

CHAPTER 5 – CONCLUSIONS

When the ICRP updated their recommendations for eye dose limits, they ignited a renewed interest in eye dosimetry, especially how the updated eye dose recommendations affect current regulations and what this means to a radiation worker. Cataracts are a common form of eye deformation and ionizing radiation can directly cause them beyond a threshold dose. Radiation workers are commonly required to wear leaded eyeglasses to reduce their eye dose, especially the lens. However, it was unknown if shield placement location in front of the leaded eyeglasses would result in additional eye protection.

The goal of this study was to use a comprehensive deterministic eye model to analyze how dose to the lens of the eye would change as shielding placement changes. The stationary shield was designed to mimic a user wearing eyeglasses and the dynamic shields were placed in various positions in front of the stationary shield. With each shield placement iteration, the photon energy was varied between 0.25 MeV and 2.5 MeV. The dose to the unshielded eye is compared to the eye dose with both shields, stationary and dynamic, to calculate one protection factor – 0 (PF0). Another protection factor was calculated, protection factor – 1 (PF1), but instead of using the unshielded dose, the eye with only the stationary shield was used as a comparator. These two protection factors were then compared to each other to determine the influence of shield positioning in front of the eye. The results of this study suggests that there is only a small change due to scatter in the dose to the eye as dynamic shield placement is changed from 3 cm in front of the stationary shield to 20 cm. Therefore, in a laboratory setting for a source emitting photons greater than 0.25 MeV it seems there is little benefit for a radiation worker to wear both leaded eyeglasses and be behind a leaded glass shield while conducting their work. As the photon energy is decreased, the multiple layers of lead shield greatly increase the protection factors regardless of shield placement. While this may be true, by following the concept of ALARA, any protection, regardless of how little, that will decrease dose is recommended.

With this study, there are several recommendations for future work to determine if shield placement plays any further part in photon eye dosimetry. First, the researcher could simplify this study by using a collimated beam source rather than a point source. A collimated beam would decrease the complexity of the SDEF card, probably eliminate the need for source biasing, and decrease the computational time for each shield placement iteration. Second, the researcher could change the scale of the shield placements to be on the orders of electron ranges and place the shields closer to the eye. This may change how CPE is established and how scattering affects the overall dose to the eye. Finally, the researcher could place the stationary shield on top of the cornea of the eye to simulate a radiation worker wearing contact lenses. By allowing radiation workers to wear prescription leaded contact lenses it may increase the likelihood that they will actually wear them.

REFERENCE LIST

Ainsbury, E. A., Barnard, S., Bright, S., & Dalke, C. (2016). Ionizing radiation induced cataracts: Recent biological and mechanistic developments and perspectives for future research. *Mutation Research, 770*, 238-261. Retrieved January 30, 2018, from https://www.sciencedirect.com/science/article/pii/S1383574216300801?via=ihub.

Anastasian, Z. H., Strozyk, D., Meyers, P. M., Wang, S., & Berman, M. F. (2011). Radiation Exposure of the Anesthesiologist in the Neurointerventional Suite. Anesthesiology, 114, 512-520.

Bentley, R. (2008). *A study of residual Cesium 137 contamination in southwestern Utah soil following the nuclear weapons tests at the Nevada Test Site in the 1950's and 1960's*. Oregon State University.

Berger, M.J. et al. (2005). XCOM: Photon Cross Section Database (ver.y1.3). [Online] Available: http://physics.nist.gov/xcom [2005, Dec. 6]. National Institute of Standards and Technology, Gaithersburg, MD.

Charles, M, W,. & Brown, N. (1975) Dimensions of the human eye relevant to radiation protection *Phys. Med. Biol.* **20** 202–18.

Chodos, A. (Ed.). (2018). November 8, 1895: Roentgen's Discovery of X-Rays. Retrieved January 15, 2018, from https://www.aps.org/publications/apsnews/200111/history.cfm

Eckerman, K.F., Cristy, M., & Ryman, J.C., (1996) *The ORNL mathematical phantom series*, available at: http://homer.ornl.gov/vlab/mird2.pdf

Eye Anatomy. (2017, October 29). Retrieved January 30, 2018, from https://www.glaucoma.org/glaucoma/anatomy-of-the-eye.php

Hall, E. J. & Giaccia, A. J. (2012). *Radiobiology for the Radiologist* (7th ed.). Philadelphia, PA: Wolters Kluwer Health/Lippincott Williams & Wilkins.

Hamada, N. & Sato, T. (2016) Cataractogenesis following high-LET radiation exposure [Electronic Version]. *Mutation Research*, 770, 262-291.

Hamby, D. M., Mangini, C, D., Caffrey, J. A., Tang, M. (2014). VARSKIN 5: A Computer Code for Skin Contamination Dosimetry. *NUREG/CR-6918 Revision 2*. Washington, DC: U.S. Nuclear Regulatory Commission.

Healy, Van Der Merwe, Christaki, & Meghzifene. (2017). Cobalt-60 Machines and Medical Linear Accelerators: Competing Technologies for External Beam Radiotherapy. *Clinical Oncology, 29*(2), 110-115.

Hubbell, J. (1969). *Photon Cross Sections, Attenuation Coefficients, and Energy Absorption Coefficients from 10 keV to 100 GeV*. Washinton, D.C: U.S Department of Commerce.

International Atomic Energy Agency. (2017). Radiation Protection of Medical Staff from Cataract. Radiation Protection of Patients (RPOP). Retrieved January 30, 2018. From https://www.iaea.org/resources/rpop/health-professionals/radiology/cataract/staff

International Commission on Radiological Protection. (1975) Reference Man: Anatomical, Physiological and Metabolic Characteristics *ICRP Publication 23* .Oxford: Pergamon.

International Commission on Radiological Protection. (1996) Conversion Coefficients for Use in Radiological Protection Against External Radiation, ICRP Publication, 74, Oxford: Pergamon Press.

International Commission on Radiological Protection. (2002) Basic anatomical and physiological data for use in radiological protection: reference values, Annals of ICRP23, Vol 89. Oxford: Pergamon Press.

International Commission on Radiological Protection. (2007). The 2007 Recommendations of the International Commission on Radiological Protection. ICRP Publication 103. Ann. ICRP 37 (2-4).

International Commission on Radiation Units. (1992) Photon, Electron, Proton and Neutron Interaction Data for Body Tissues *ICRU Report 46.* Bethesda, MD: ICRU.

Knoll, G. F. (2000). *Radiation Detection and Measurement* (3th ed.). Hoboken, NJ: John Wiley & Sons.

Krstic, D., Nikezic, D. (2006) External doses in humans from 137Cs in soil. Health Physics 91 (3): 249-257.

Krstic, D. & Nikezic, D. (2006) Input Files with ORNL-mathematical phantoms of the human body for MCNP-4B [Electronic Version]. *Computer Physics Communications*, 176, 33-37.

Krstic, D., Nikezic, D. (2007) Conversion coefficients for age dependent ORNL phantoms from 137Cs in soil as a source of external exposure. Nuclear Instruments and Methods A 580 (1) 540-543.

Meroli, S. The Interaction of Photons with the Matter. *Life of an Engineer at CERN Blog*. Retreived January 30, 2018, from http://meroli.web.cern.ch/Lecture_photon_interaction.html

Merriam, G. R. & Worgul, B. V. (1983) Experimental radiation cataract—its clinical relevance *Bull. N. Y. Acad. Med.* **59** 372–92.

Monte Carlo Team, MCNP6 User's Manual. MCNP-A General Purpose Monte Carlo N-Particle Transport Code, Version 6. LA-CP-13-00634, Rev. 0, Los Alamos National Laboratory, May 2013.

National Council on Radiation Protection and Measurements (1999) Biological effects and exposure limits for hot particles *Report No 130.* Bethesda, MD: NCRP

Nogueira, P., Zankl, M.,Schlattl, H., & Vaz, P. (2011). Dose conversion coefficients for monoenergetic electrons incident on a realistic human eye model with different lens cell populations. *Physics in Medicine and Biology*,65. Retrieved January 30, 2018, from http://iopscience.iop.org/article/10.1088/0031-9155/56/21/010/meta

Schwarz, A. L., Schwarz, R. A., & Carter, L. L. MCNP/MCNPX Visual Editor Computer Code Manual. Version 24E. February 2011.

Seuntjens, J., Strydom, W., & Shortt, K. (2005). Review of Radiation Oncology Physics: A Handbook for Teachers and Students. Vienna: Sales and Promotion Unit, Publishing Section, IAEA.

Shultis, J., & Faw, R. (2008). Fundamentals of Nuclear Science and Engineering. Boca Raton: CRC Press.

Snell, R., Lemp, Michael A, & Grunther, Ira. (1998). *Clinical anatomy of the eye* (2nd ed.). Oxford ; Malden, MA: Blackwell Science Ltd,.

Standards for Protection Against Radiation, 10 Fed. Reg. 20.1003 (2018)

Sutton, C. (2017, July 28). Subatomic particle. Retrieved January 15, 2018, from https://www.britannica.com/science/subatomic-particle

Tasch, B. (2015, August 31). Marie Curie's Belongings Will Be Radioactive For Another 1,500 Years. Retrieved January 15, 2018, from https://www.sciencealert.com/these-personal-effects-of-marie-curie-will-be-radioactive-for-another-1-500-years

The Human Eye, Its Functions, and Visual Impairment. (2018). Retrieved January 15, 2018, from http://www.afb.org/info/the-human-eye-its-functions-and-visual-impairment/5

U.S Department of Homeland Security (2011) Compendium of Material Composition Data for Radiation Transport Modeling. US. Customs and Boarder Protection and Domestic Nuclear Detection Office. PIET-43741-TM-963.

Wagenaar, D. J. (1995). The Bragg Curve. Radiation Physics Principles. Retrieved on May 01, 2018, from http://www.med.harvard.edu/jpnm/physics/nmltd/radprin/sect7/7.1/7_1.3.html

Worgul, B. V. (1991) *The Edward S Harkness Eye Institute Resident's Basic Science Study Guide.* New York: Columbia University Press.

APPENDICES

APPENDIX A

Photon Energy to Dose Curve

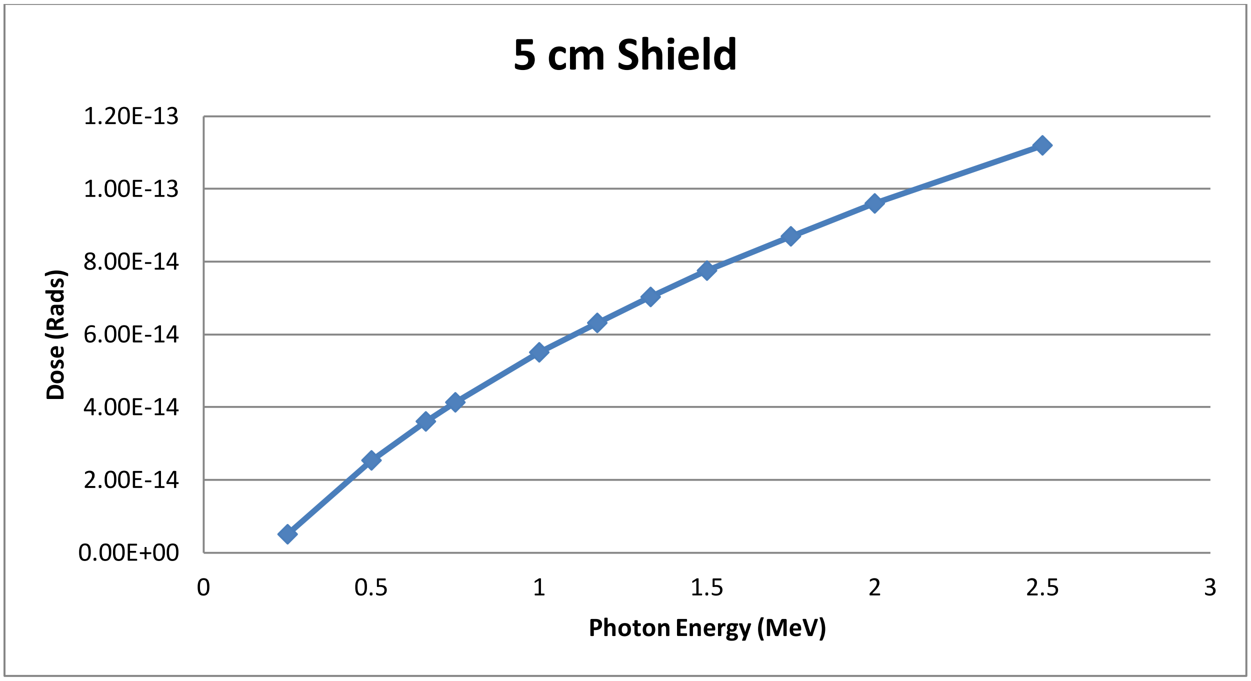

Appendix Figures A : 5 cm Photon Energy to Dose Curve

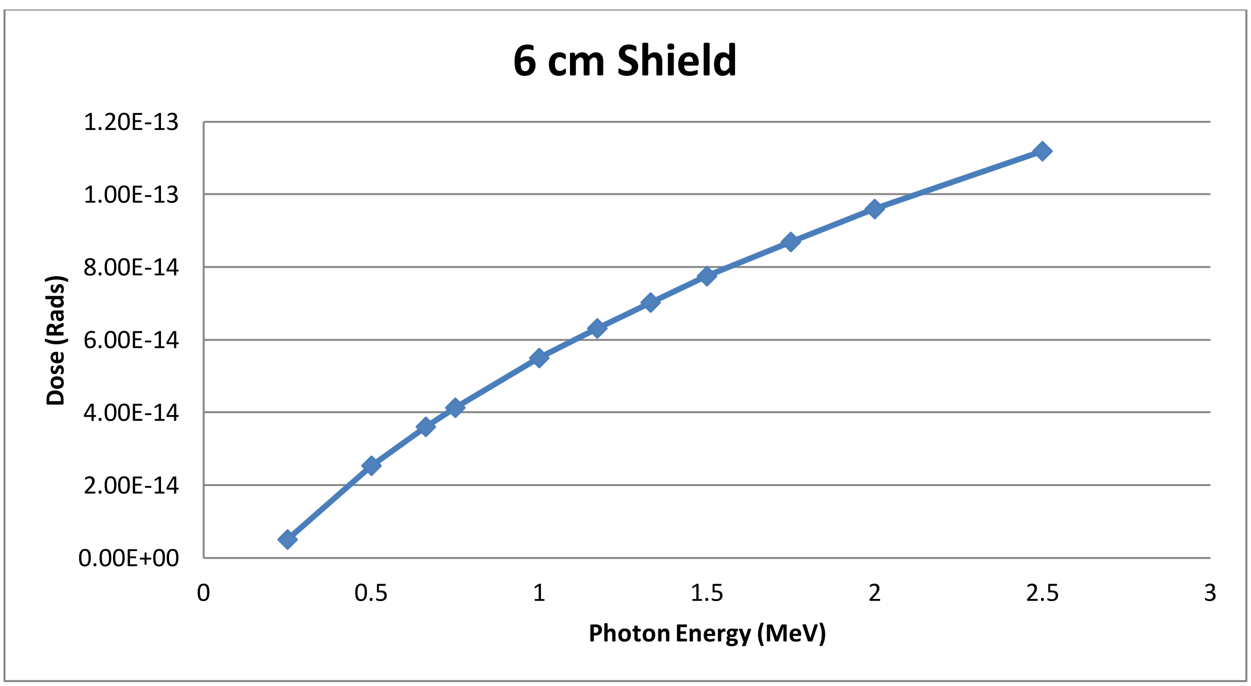

Appendix Figures B: 6 cm Photon Energy to Dose Curve

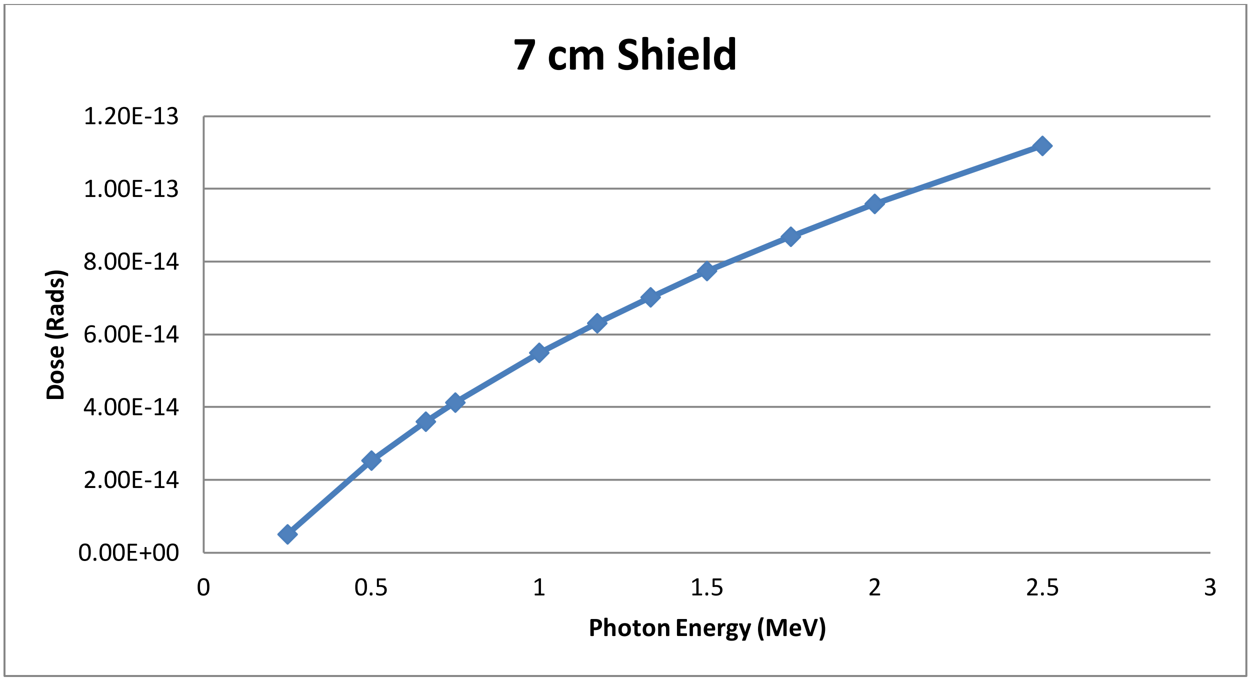

Appendix Figures C: 7 cm Photon Energy to Dose Curve

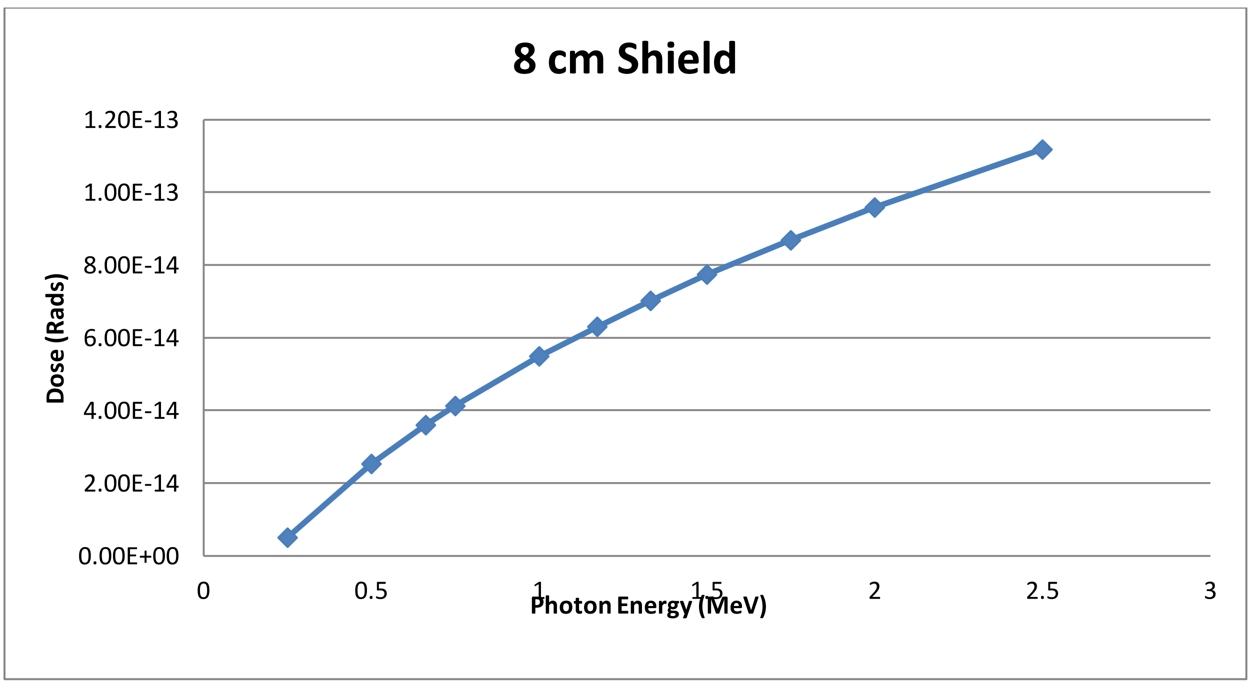

Appendix Figures D: 8 cm Photon Energy to Dose Curve

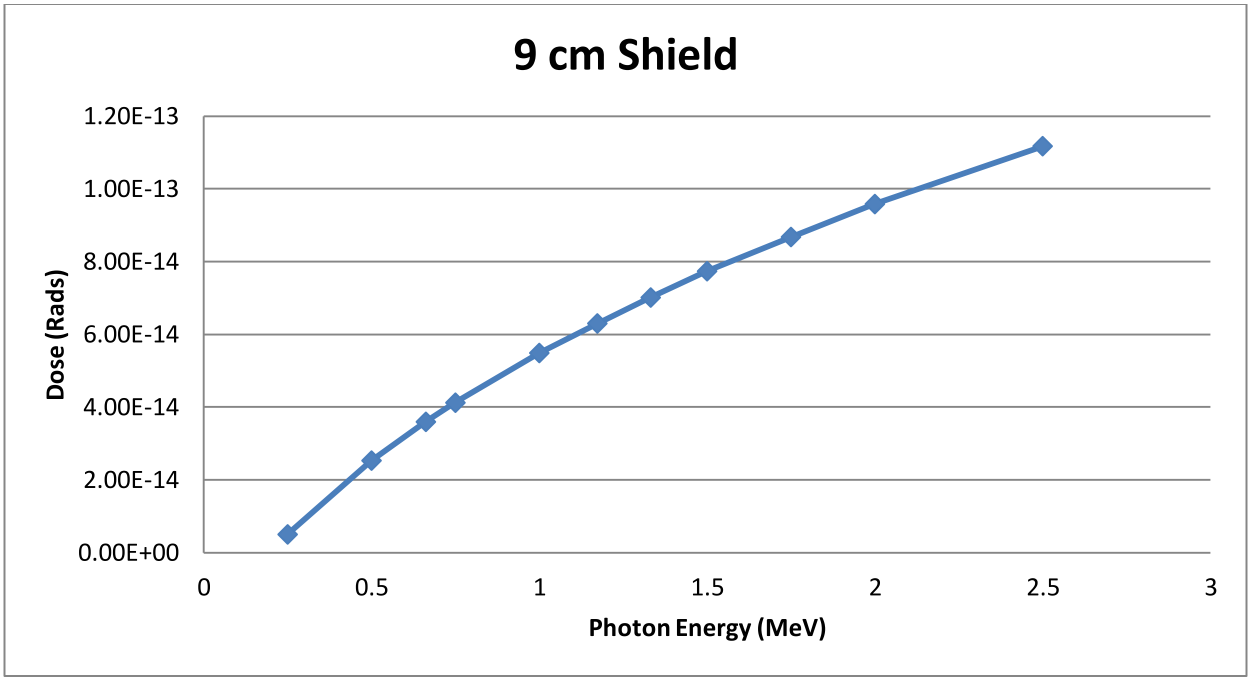

Appendix Figures E: 9 cm Photon Energy to Dose Curve

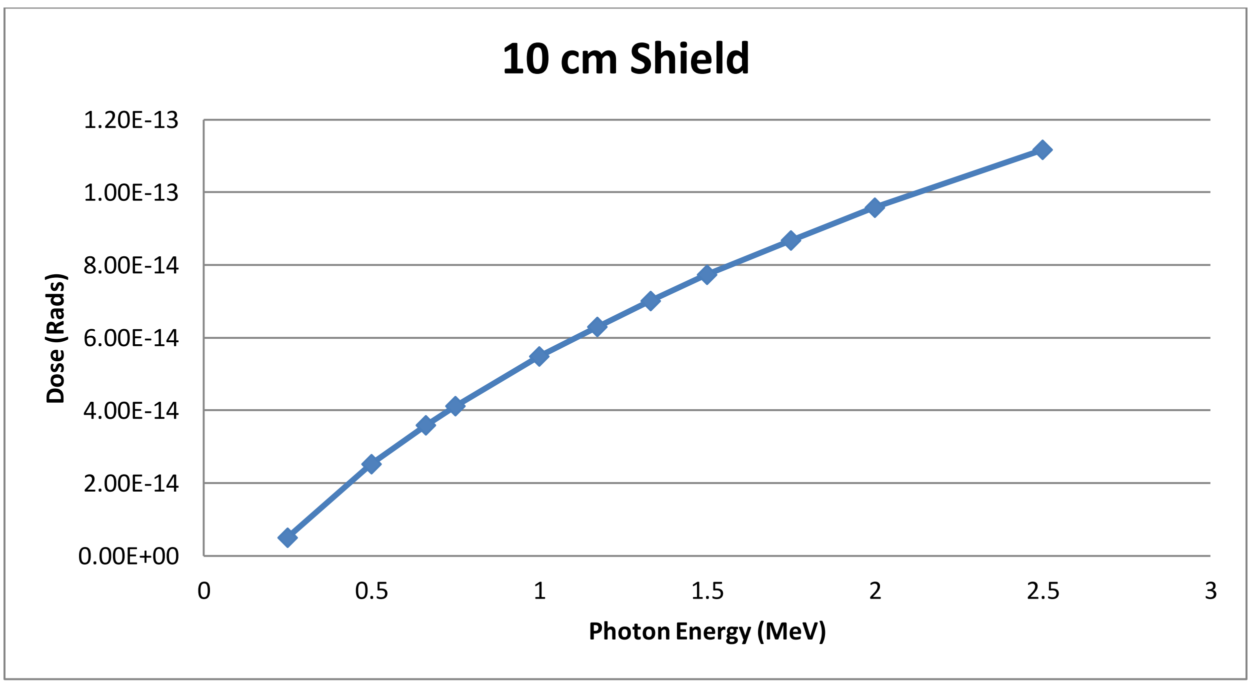

Appendix Figures F: 10 cm Photon Energy to Dose Curve

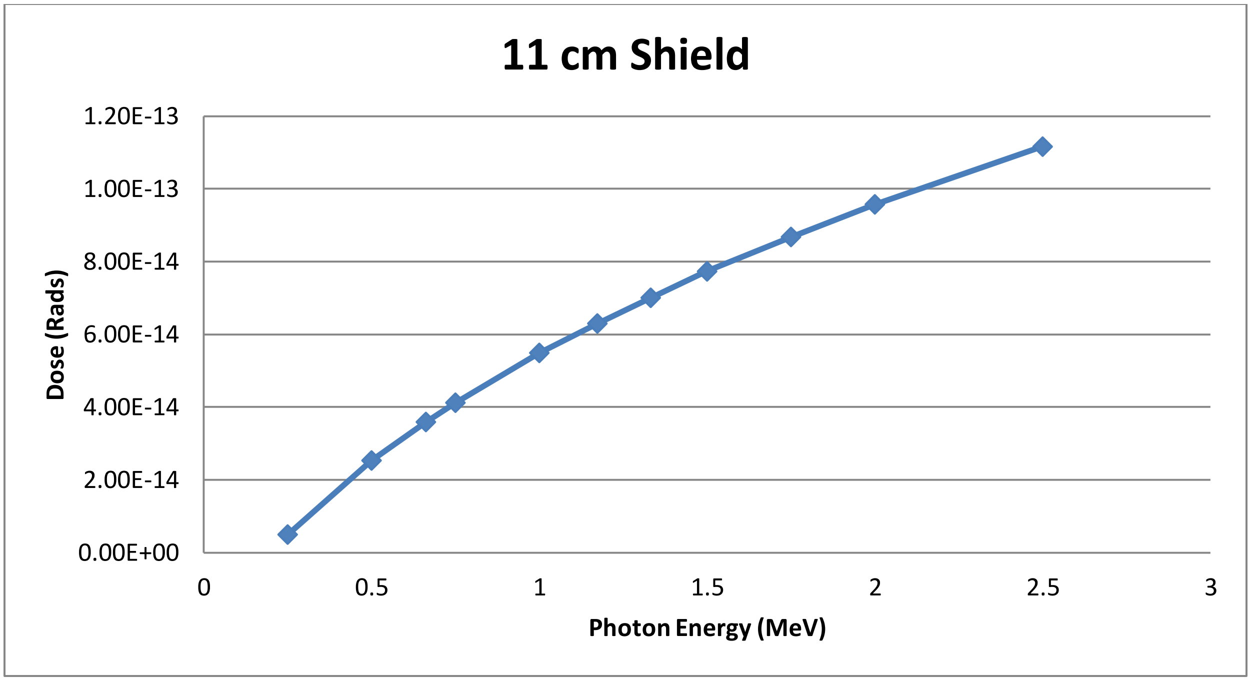

Appendix Figures G: 11 cm Photon Energy to Dose Curve

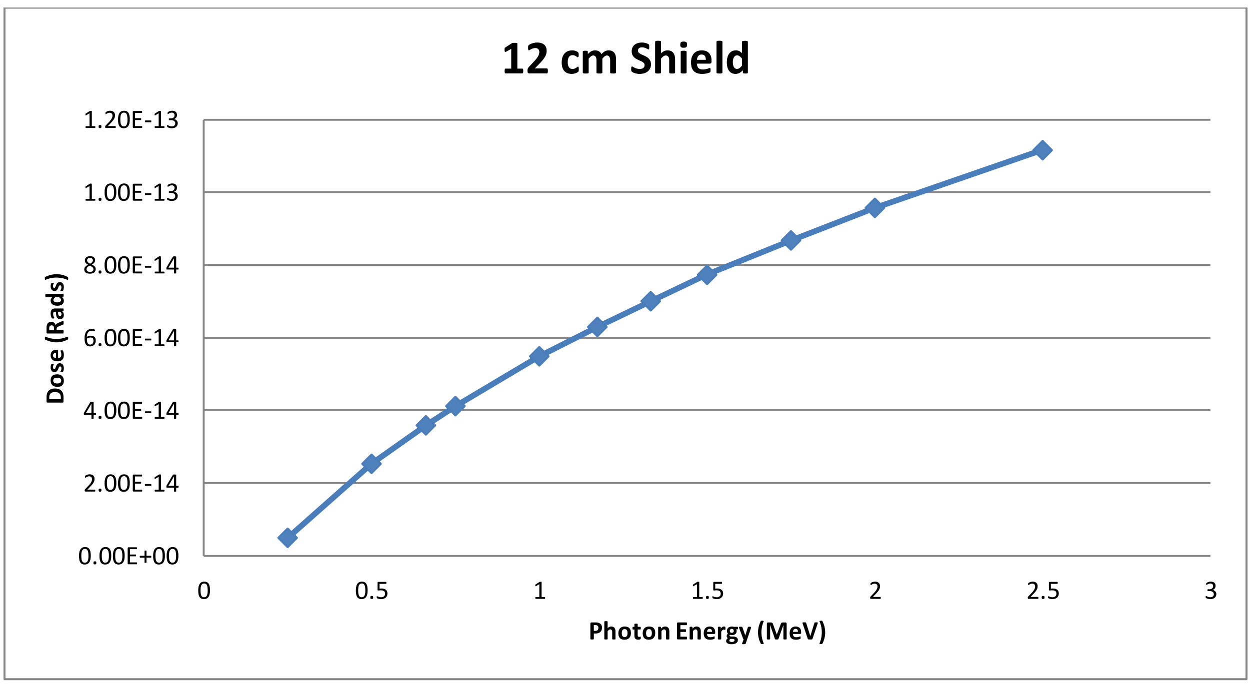

Appendix Figures H: 12 cm Photon Energy to Dose Curve

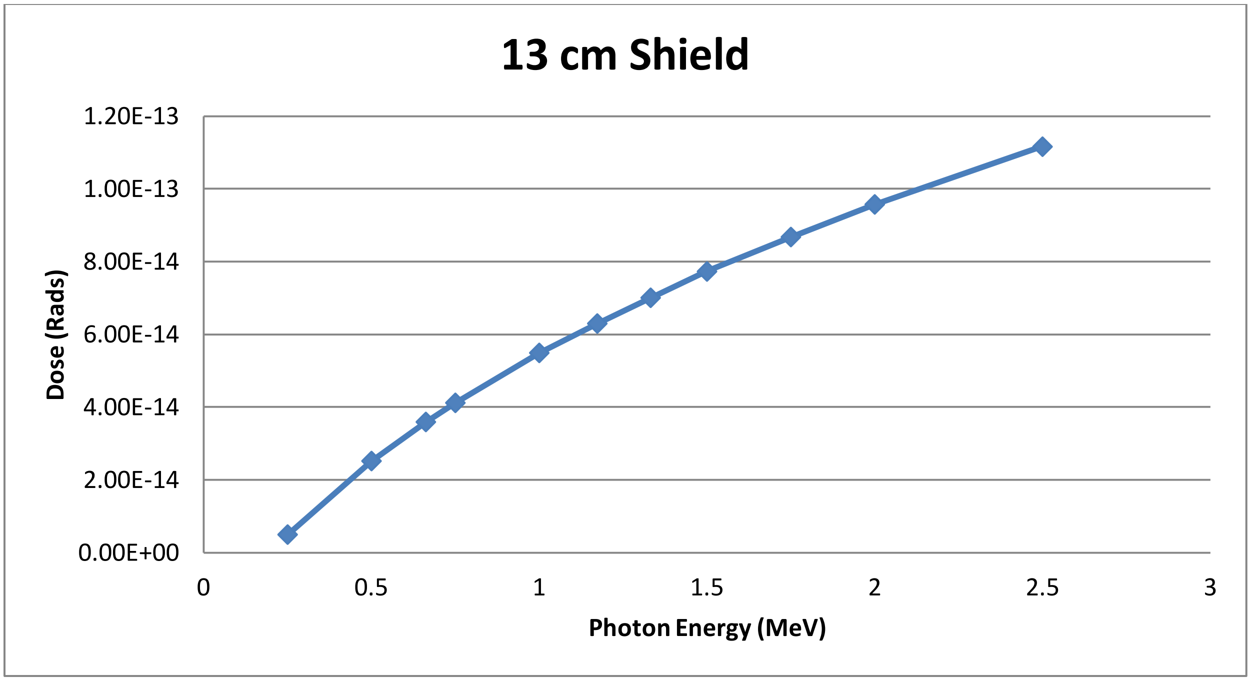

Appendix Figures I: 13 cm Photon Energy to Dose Curve

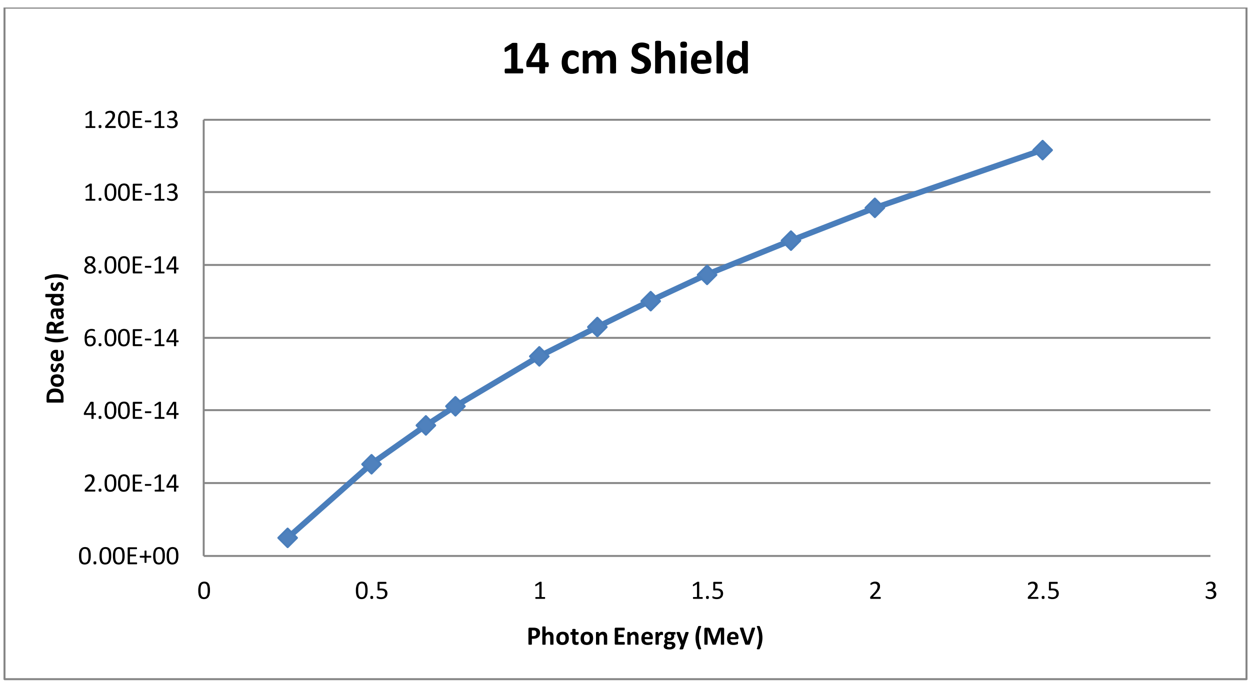

Appendix Figures J: 14 cm Photon Energy to Dose Curve

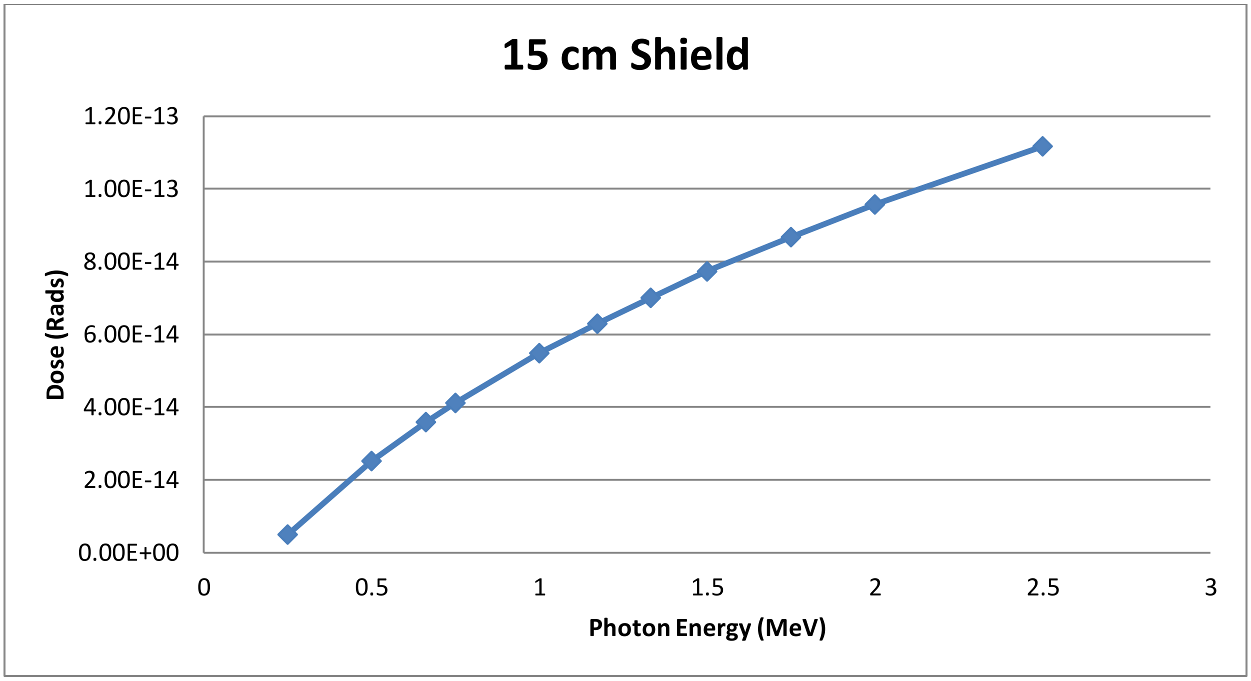

Appendix Figures K: 15 cm Photon Energy to Dose Curve

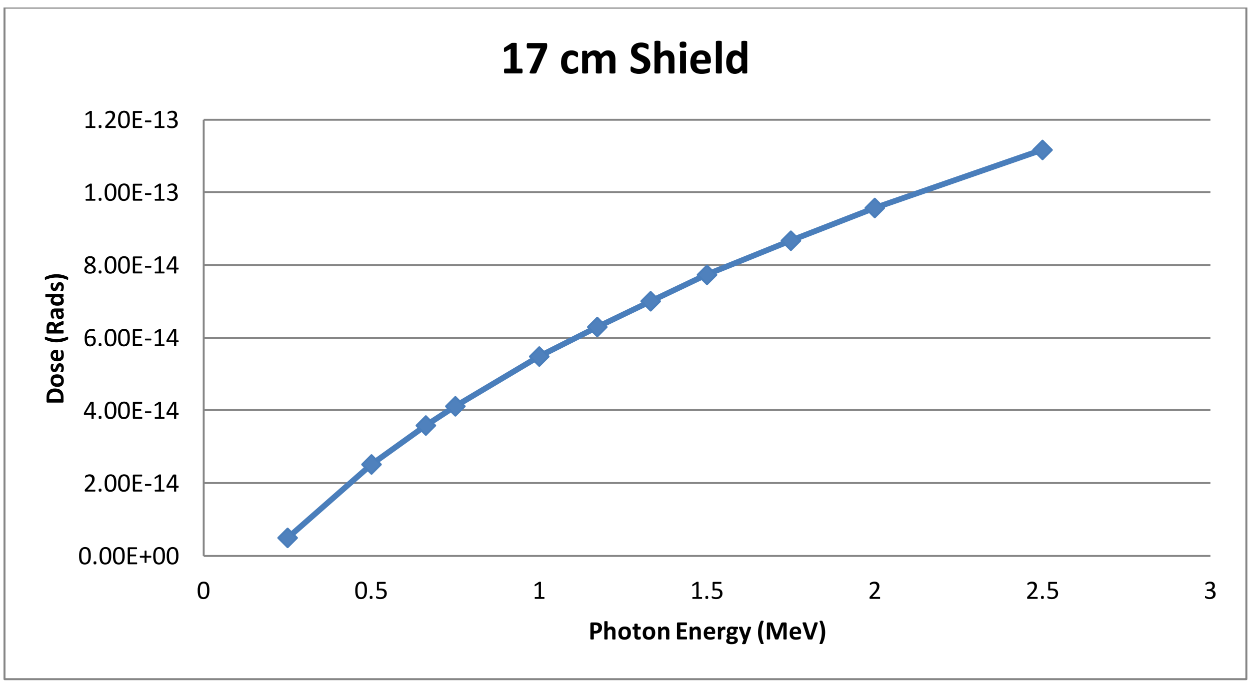

Appendix Figures L: 17 cm Photon Energy to Dose Curve

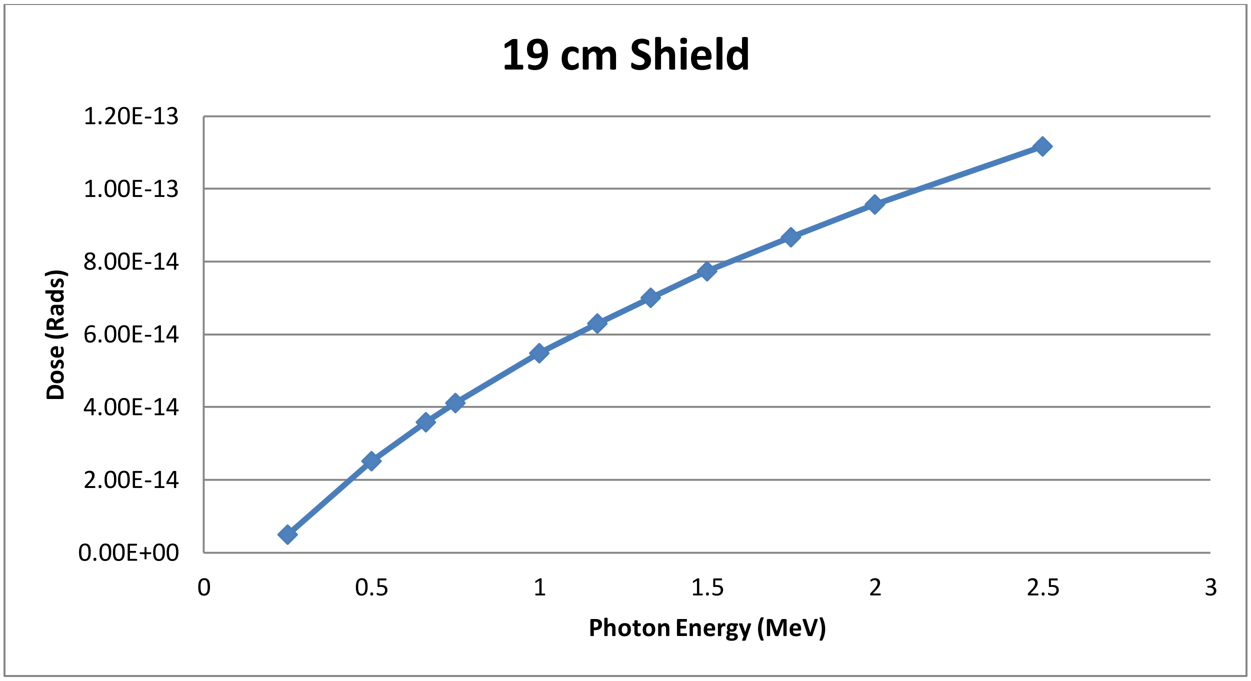

Appendix Figures M: 19 cm Photon Energy to Dose Curve

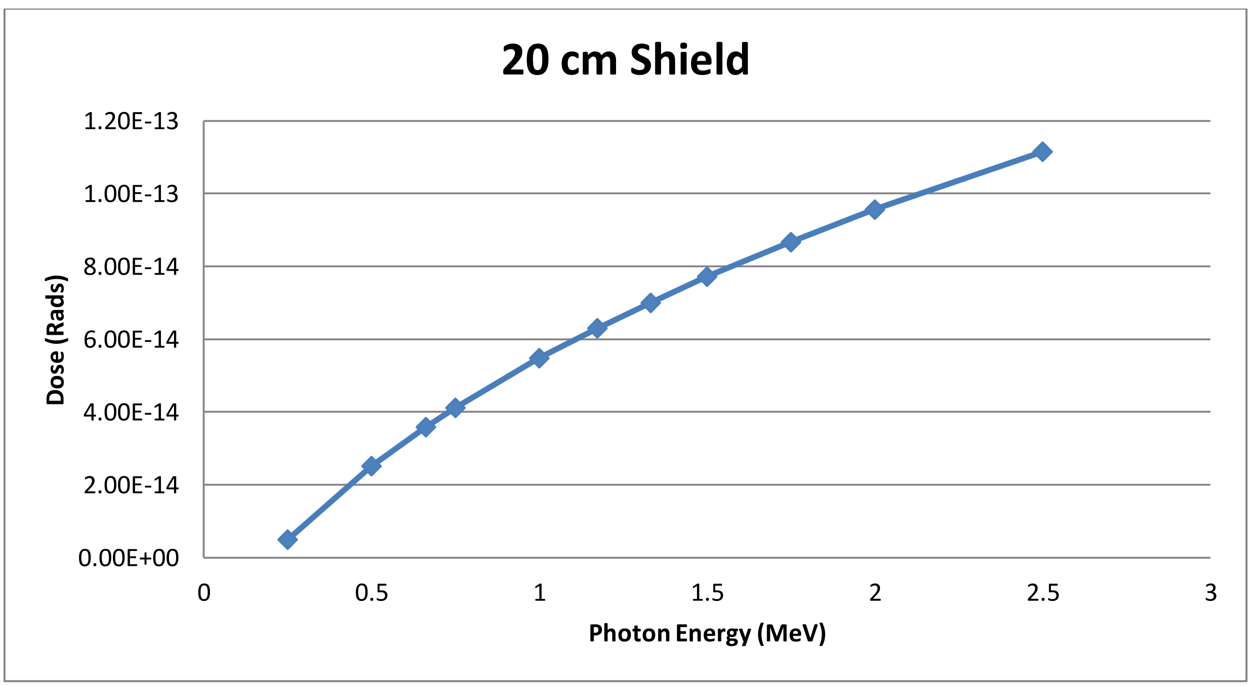

Appendix Figures N: 20 cm Photon Energy to Dose Curve

APPENDIX B

Dose to Shield Placement Tables

3 cm Shield			
Energy (MeV)	Dose (Rads)	Energy (MeV)	Dose (Rads)
0.25	5.07E-15	1.332	3.59E-14
0.5	2.55E-14	1.5	3.55E-14
0.662	3.61E-14	1.75	3.40E-14
0.75	4.14E-14	2	3.18E-14
1	3.64E-14	2.5	8.61E-05
1.173	3.62E-14		

Appendix Tables 1: 3 cm Shield Placement Doses

5 cm Shield			
Energy (MeV)	Dose (Rads)	Energy (MeV)	Dose (Rads)
0.25	5.04E-15	1.332	3.58E-14
0.5	2.53E-14	1.5	3.54E-14
0.662	3.61E-14	1.75	3.40E-14
0.75	4.13E-14	2	3.18E-14
1	3.63E-14	2.5	8.61E-05
1.173	3.61E-14		

Appendix Tables 2: 5 cm Shield Placement Doses

6 cm Shield			
Energy (MeV)	Dose (Rads)	Energy (MeV)	Dose (Rads)
0.25	5.03E-15	1.332	3.58E-14
0.5	2.53E-14	1.5	3.53E-14
0.662	3.60E-14	1.75	3.39E-14
0.75	4.13E-14	2	3.18E-14
1	3.63E-14	2.5	8.61E-05
1.173	3.61E-14		

Appendix Tables 3: 6 cm Shield Placement Doses

7 cm Shield			
Energy (MeV)	Dose (Rads)	Energy (MeV)	Dose (Rads)
0.25	5.02E-15	1.332	3.58E-14
0.5	2.53E-14	1.5	3.53E-14
0.662	3.60E-14	1.75	3.39E-14
0.75	4.13E-14	2	3.17E-14
1	3.63E-14	2.5	8.61E-05
1.173	3.61E-14		

Appendix Tables 4: 7 cm Shield Placement Doses

8 cm Shield			
Energy (MeV)	Dose (Rads)	Energy (MeV)	Dose (Rads)
0.25	5.01E-15	1.332	3.57E-14
0.5	2.53E-14	1.5	3.53E-14
0.662	3.60E-14	1.75	3.39E-14
0.75	4.12E-14	2	3.17E-14
1	3.62E-14	2.5	8.61E-05
1.173	3.61E-14		

Appendix Tables 5: 8 cm Shield Placement Doses

9 cm Shield			
Energy (MeV)	Dose (Rads)	Energy (MeV)	Dose (Rads)
0.25	5.01E-15	1.332	3.57E-14
0.5	2.53E-14	1.5	3.53E-14
0.662	3.60E-14	1.75	3.39E-14
0.75	4.12E-14	2	3.17E-14
1	3.62E-14	2.5	8.61E-05
1.173	3.60E-14		

Appendix Tables 6: 9 cm Shield Placement Doses

10 cm Shield			
Energy (MeV)	Dose (Rads)	Energy (MeV)	Dose (Rads)
0.25	5.00E-15	1.332	3.57E-14
0.5	2.52E-14	1.5	3.53E-14
0.662	3.59E-14	1.75	3.39E-14
0.75	4.12E-14	2	3.17E-14
1	3.62E-14	2.5	8.61E-05
1.173	3.60E-14		

Appendix Tables 7: 10 cm Shield Placement Doses

11 cm Shield			
Energy (MeV)	Dose (Rads)	Energy (MeV)	Dose (Rads)
0.25	4.98E-15	1.332	3.57E-14
0.5	2.53E-14	1.5	3.53E-14
0.662	3.59E-14	1.75	3.39E-14
0.75	4.12E-14	2	3.17E-14
1	3.63E-14	2.5	8.61E-05
1.173	3.60E-14		

Appendix Tables 8: 11 cm Shield Placement Doses

12 cm Shield			
Energy (MeV)	Dose (Rads)	Energy (MeV)	Dose (Rads)
0.25	4.97E-15	1.332	3.57E-14
0.5	2.53E-14	1.5	3.53E-14
0.662	3.59E-14	1.75	3.39E-14
0.75	4.12E-14	2	3.17E-14
1	3.63E-14	2.5	8.61E-05
1.173	3.60E-14		

Appendix Tables 9: 12 cm Shield Placement Doses

13 cm Shield			
Energy (MeV)	Dose (Rads)	Energy (MeV)	Dose (Rads)
0.25	4.97E-15	1.332	3.57E-14
0.5	2.52E-14	1.5	3.53E-14
0.662	3.59E-14	1.75	3.39E-14
0.75	4.12E-14	2	3.17E-14
1	3.63E-14	2.5	8.61E-05
1.173	3.60E-14		

Appendix Tables 10: 13 cm Shield Placement Doses

14 cm Shield			
Energy (MeV)	Dose (Rads)	Energy (MeV)	Dose (Rads)
0.25	4.96E-15	1.332	3.57E-14
0.5	2.52E-14	1.5	3.53E-14
0.662	3.59E-14	1.75	3.39E-14
0.75	4.12E-14	2	3.17E-14
1	3.62E-14	2.5	1.08E-04
1.173	3.60E-14		

Appendix Tables 11: 14 cm Shield Placement Doses

15 cm Shield			
Energy (MeV)	Dose (Rads)	Energy (MeV)	Dose (Rads)
0.25	4.97E-15	1.332	3.57E-14
0.5	2.52E-14	1.5	3.53E-14
0.662	3.59E-14	1.75	3.39E-14
0.75	4.12E-14	2	3.17E-14
1	3.62E-14	2.5	1.51E-04
1.173	3.60E-14		

Appendix Tables 12: 15 cm Shield Placement Doses

17 cm Shield			
Energy (MeV)	Dose (Rads)	Energy (MeV)	Dose (Rads)
0.25	4.96E-15	1.332	3.57E-14
0.5	2.52E-14	1.5	3.53E-14
0.662	3.59E-14	1.75	3.39E-14
0.75	4.12E-14	2	3.17E-14
1	3.62E-14	2.5	1.51E-04
1.173	3.60E-14		

Appendix Tables 13: 17 cm Shield Placement Doses

19 cm Shield			
Energy (MeV)	Dose (Rads)	Energy (MeV)	Dose (Rads)
0.25	4.95E-15	1.332	3.57E-14
0.5	2.52E-14	1.5	3.53E-14
0.662	3.59E-14	1.75	3.39E-14
0.75	4.11E-14	2	3.17E-14
1	3.62E-14	2.5	1.08E-04
1.173	3.60E-14		

Appendix Tables 14: 19 cm Shield Placement Doses

20 cm Shield			
Energy (MeV)	Dose (Rads)	Energy (MeV)	Dose (Rads)
0.25	4.96E-15	1.332	3.57E-14
0.5	2.52E-14	1.5	3.52E-14
0.662	3.59E-14	1.75	3.39E-14
0.75	4.12E-14	2	3.16E-14
1	3.62E-14	2.5	1.08E-04
1.173	3.61E-14		

Appendix Tables 15: 20 cm Shield Placement Doses

APPENDIX C

Dose to Shield Placement Curve

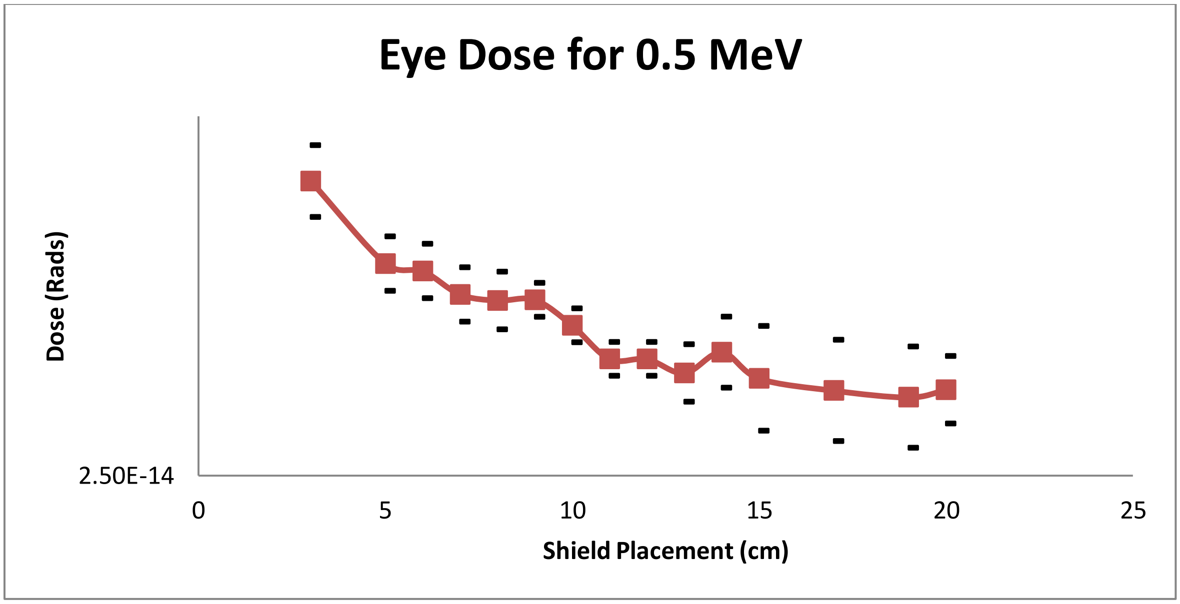

Appendix Figures O: 0.5 MeV Photon Energy to Dose Curve

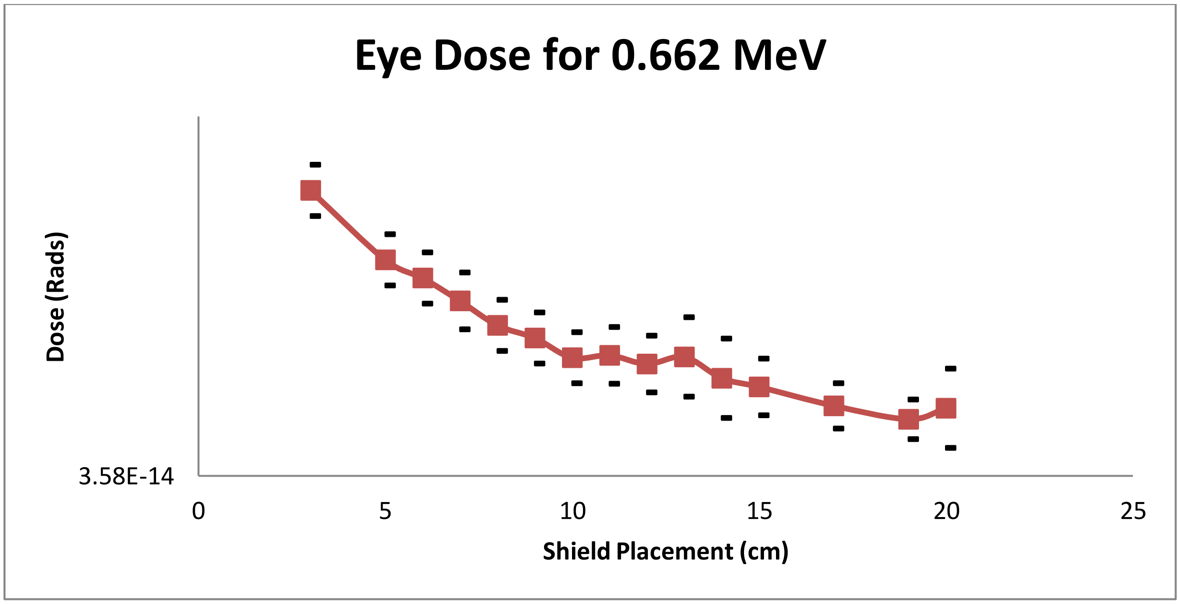

Appendix Figures P: 0.662 MeV Photon Energy to Dose Curve

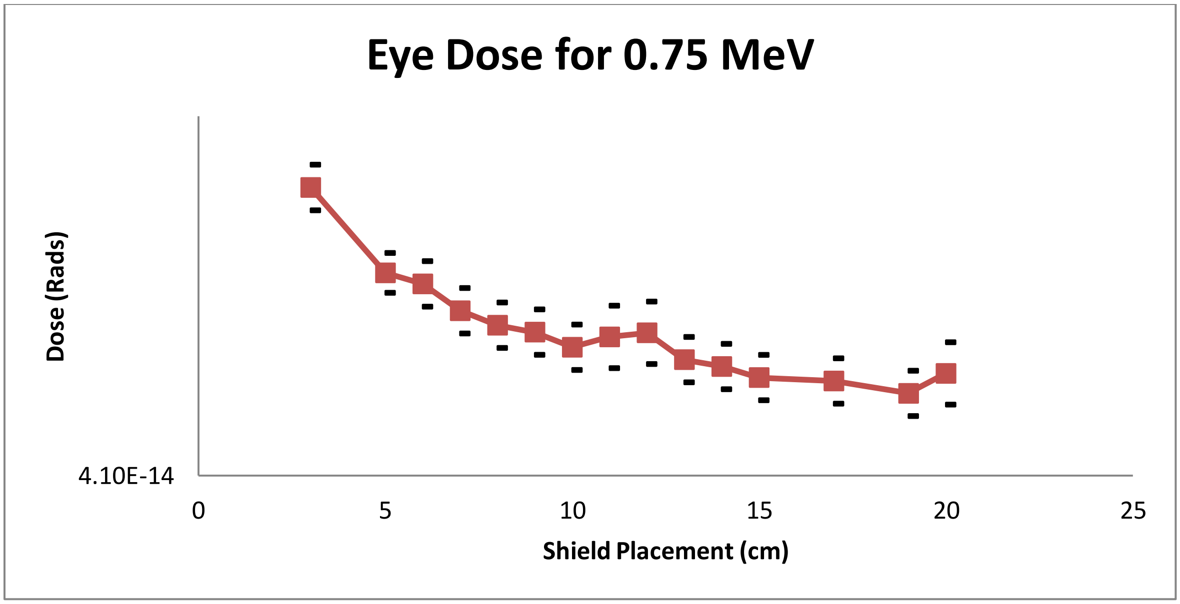

Appendix Figures Q: 0.75 MeV Photon Energy to Dose Curve

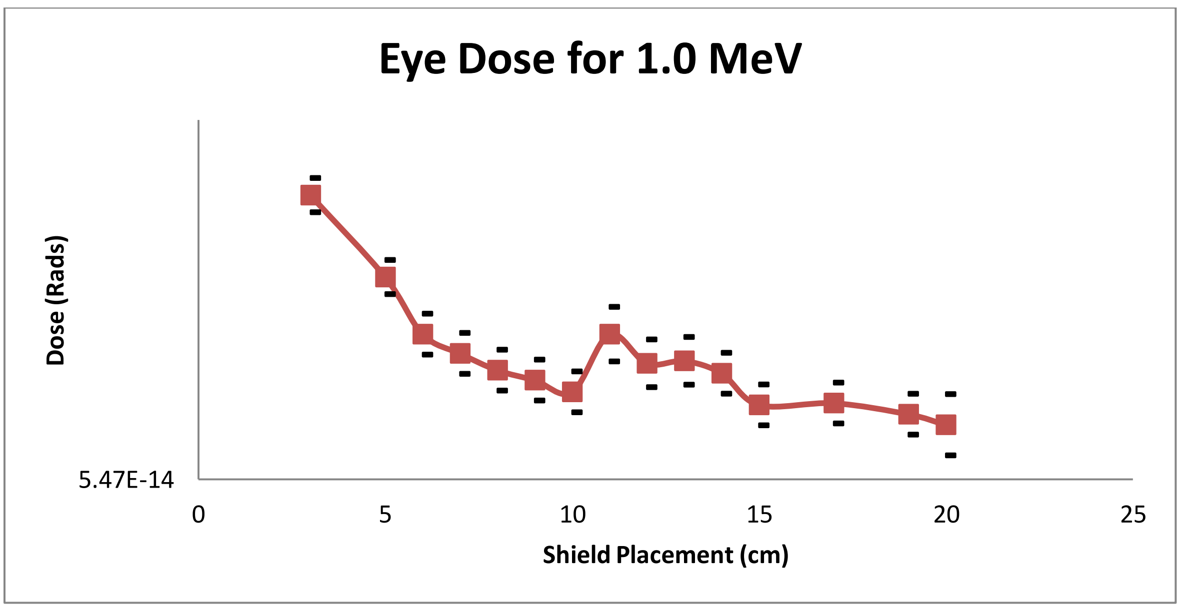

Appendix Figures R: 1.0 MeV Photon Energy to Dose Curve

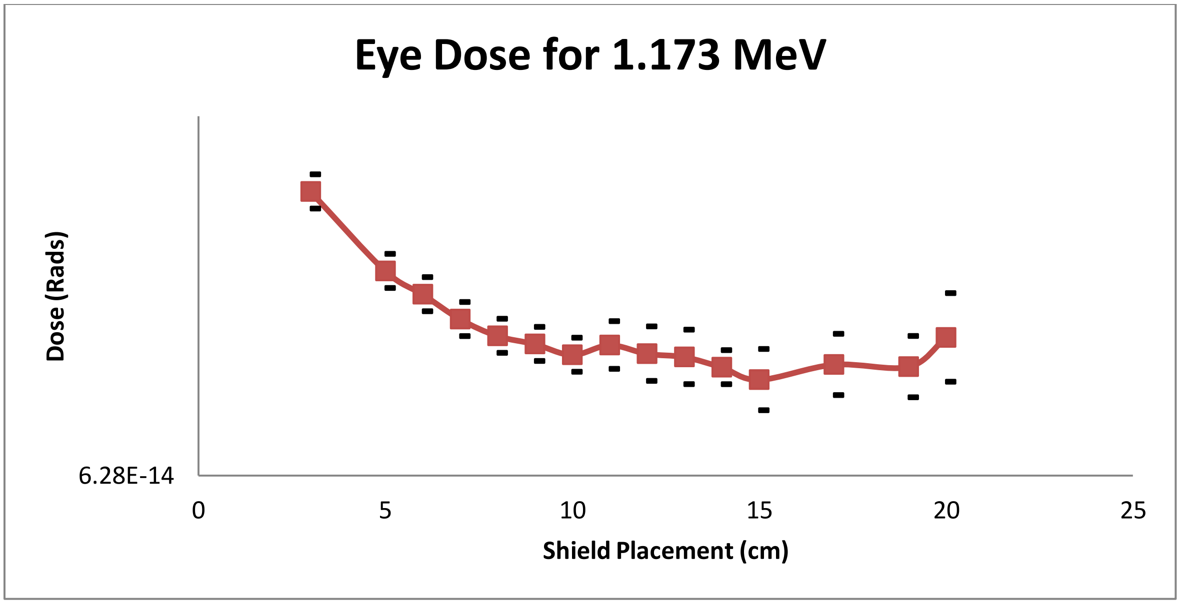

Appendix Figures S: 1.173 MeV Photon Energy to Dose Curve

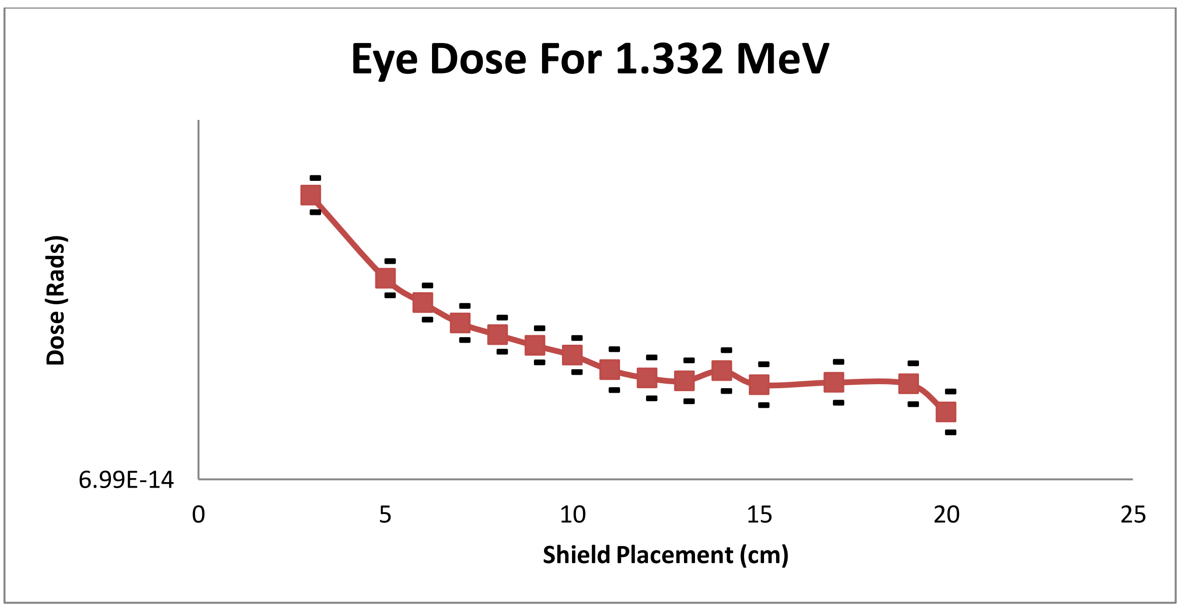

Appendix Figures T: 1.332 MeV Photon Energy to Dose Curve

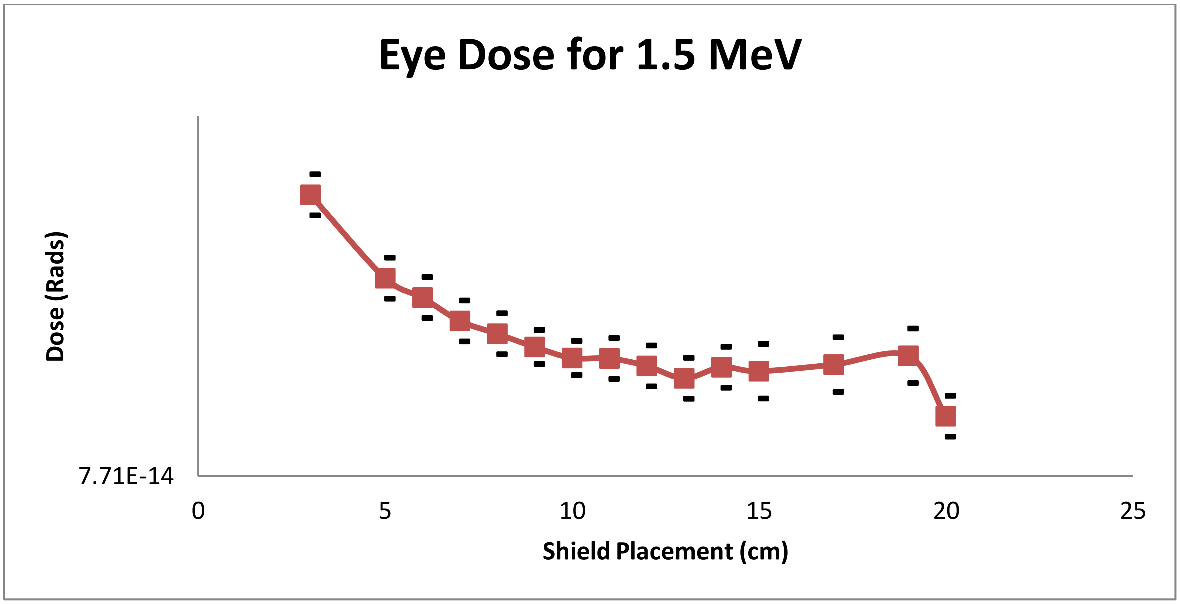

Appendix Figures U: 1.5 MeV Photon Energy to Dose Curve

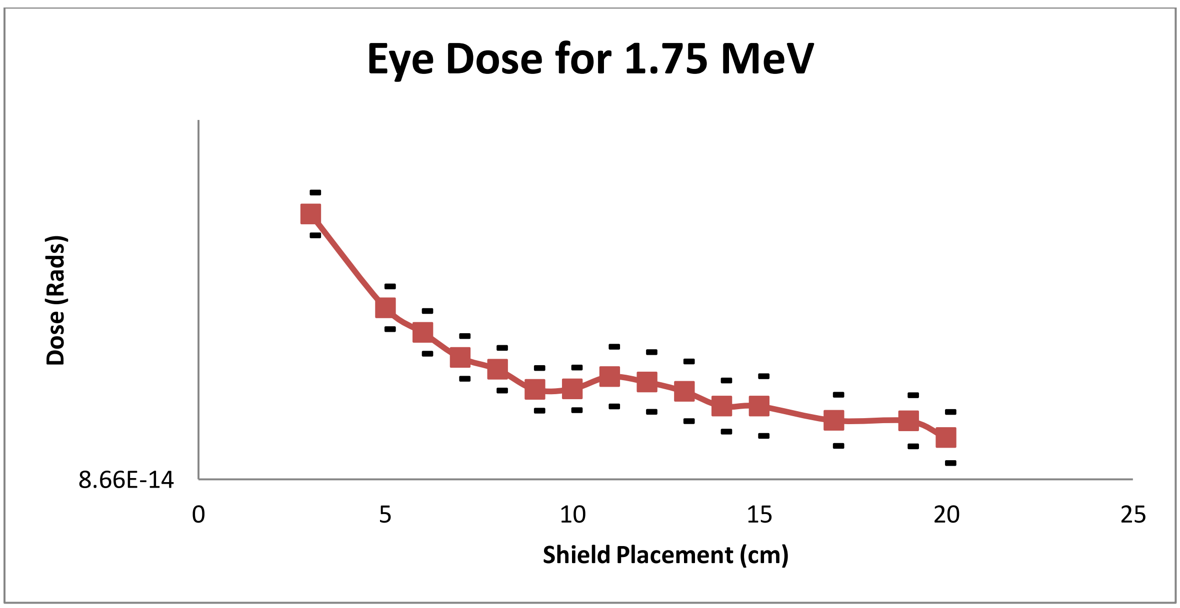

Appendix Figures V: 1.75 MeV Photon Energy to Dose Curve

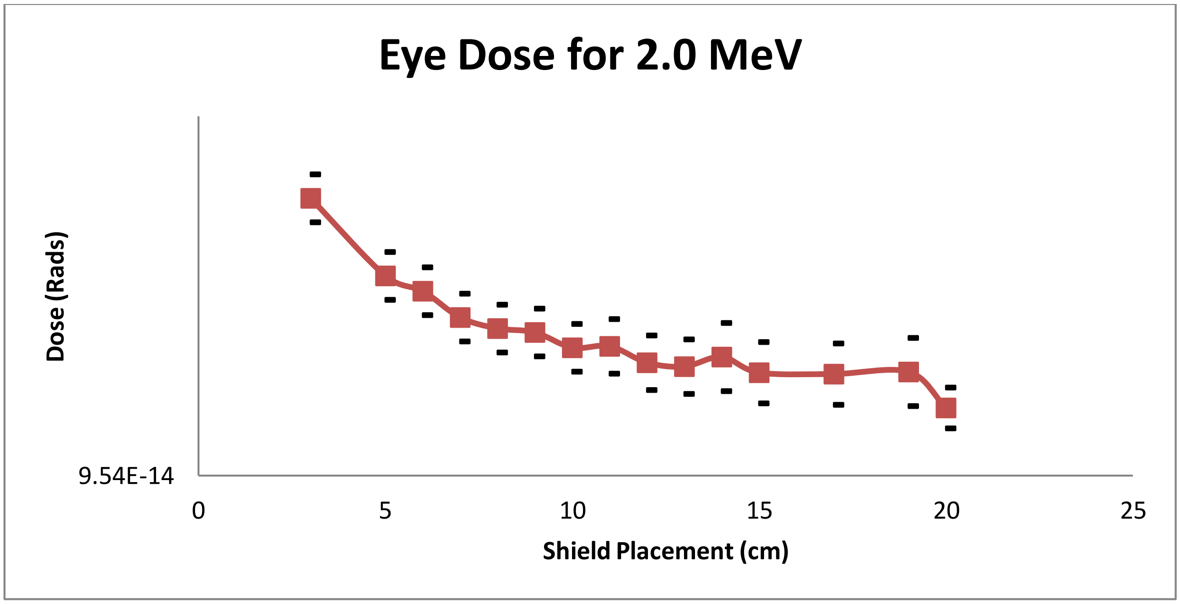

Appendix Figures W: 2.0 MeV Photon Energy to Dose Curve

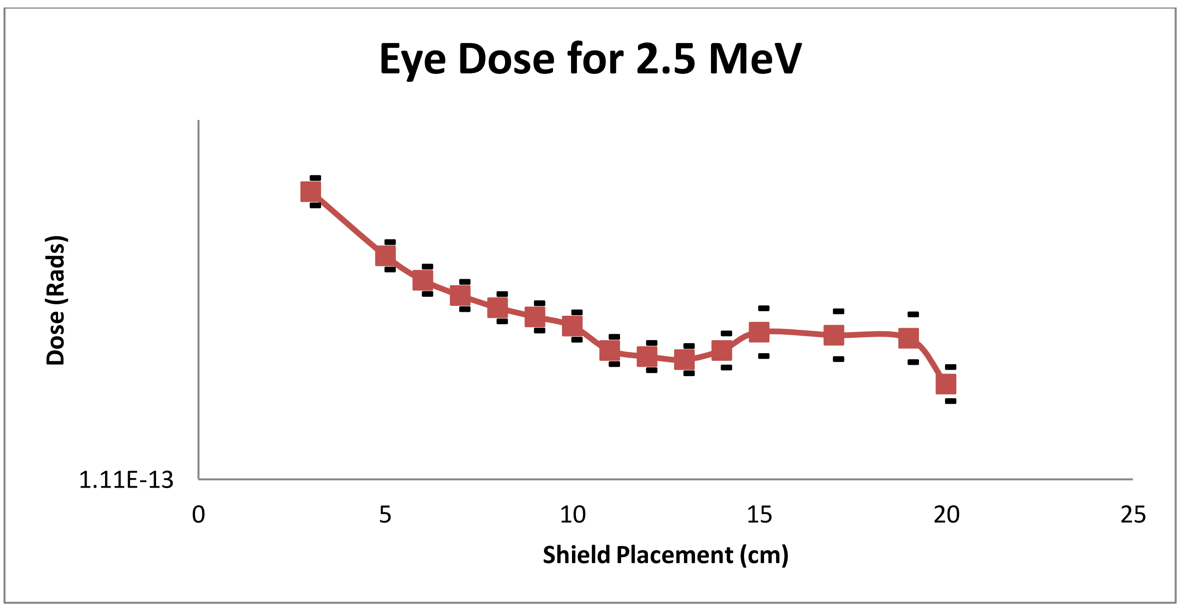

Appendix Figures X: 2.5 MeV Photon Energy to Dose Curve

APPENDIX D

Protection Factor to Photon Energy Curve

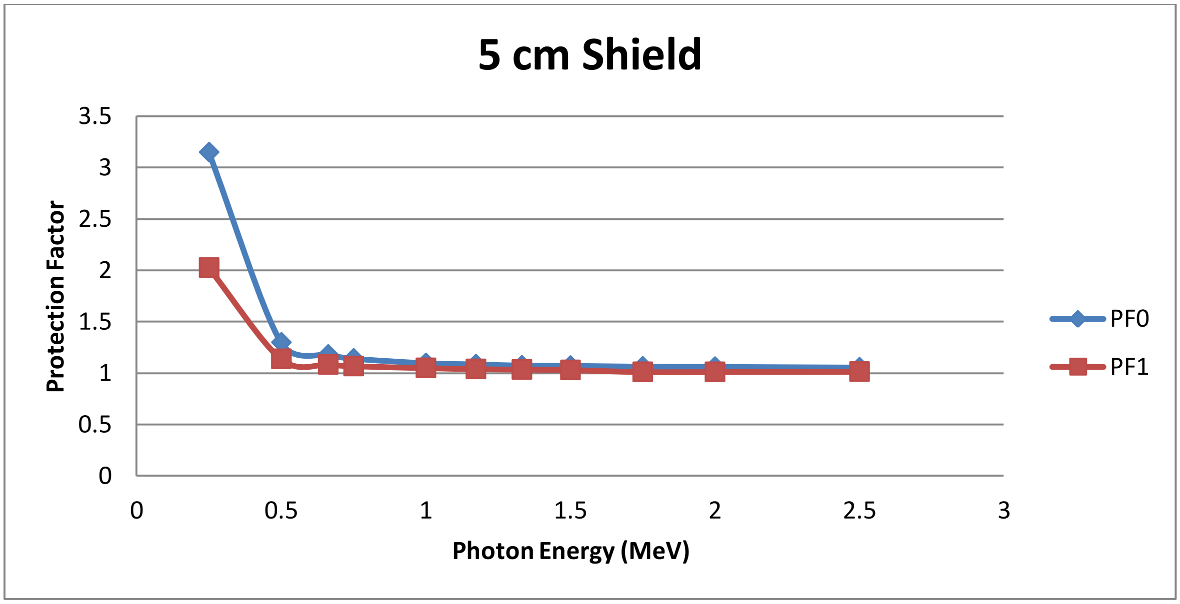

Appendix Figures Y: 5 cm Protection Factor to Photon Energy Curve

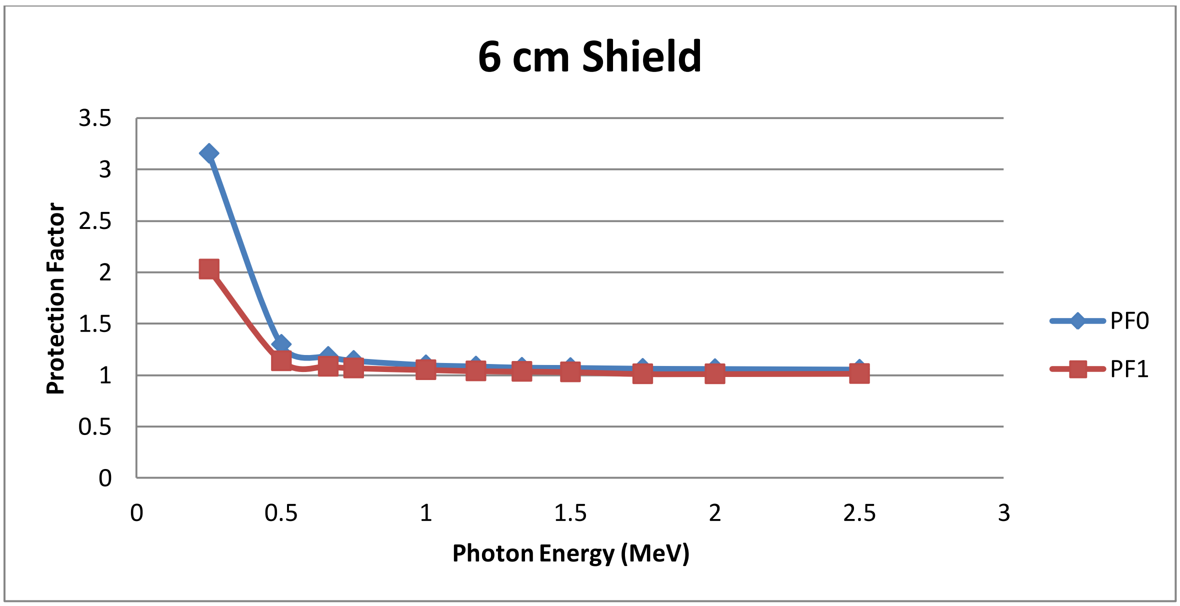

Appendix Figures Z: 6 cm Protection Factor to Photon Energy Curve

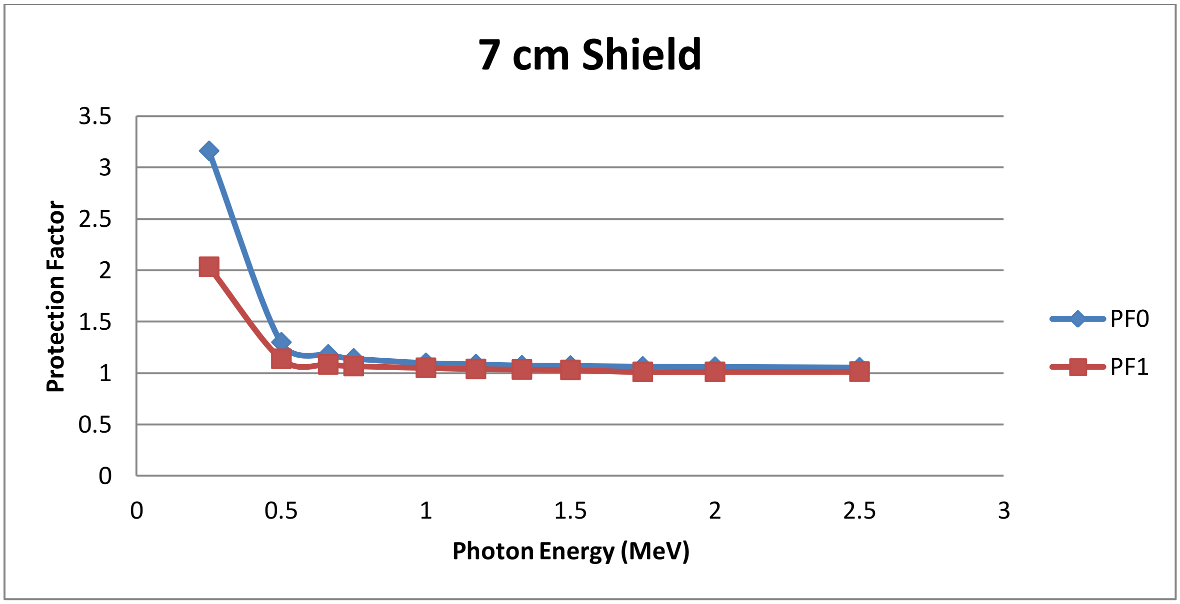

Appendix Figures AA: 7 cm Protection Factor to Photon Energy Curve

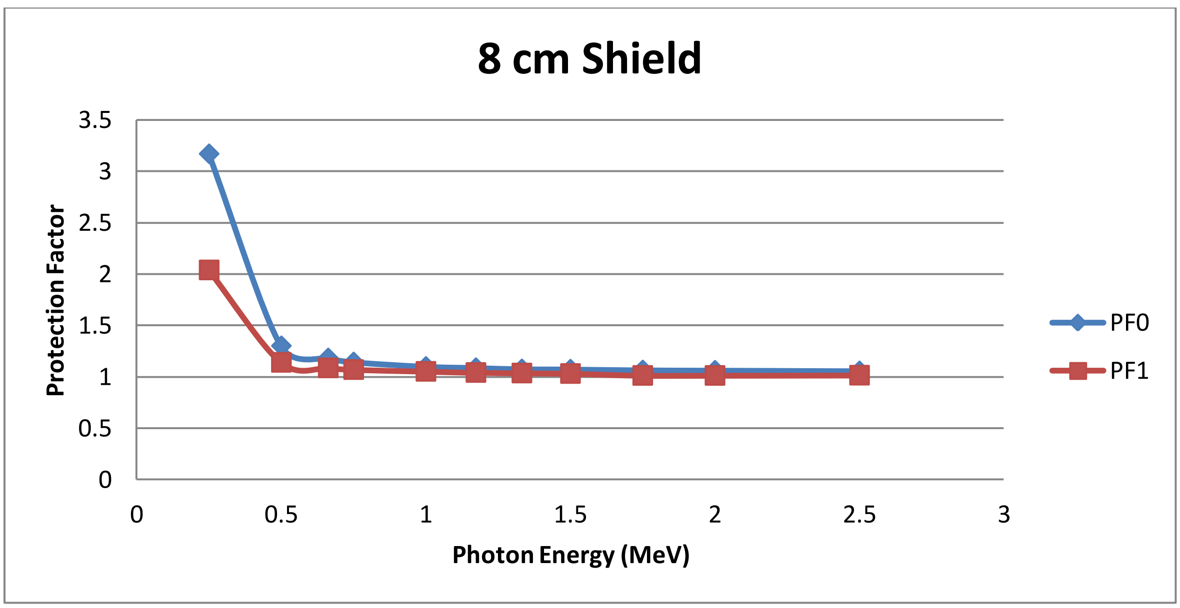

Appendix Figures BB: 8 cm Protection Factor to Photon Energy Curve

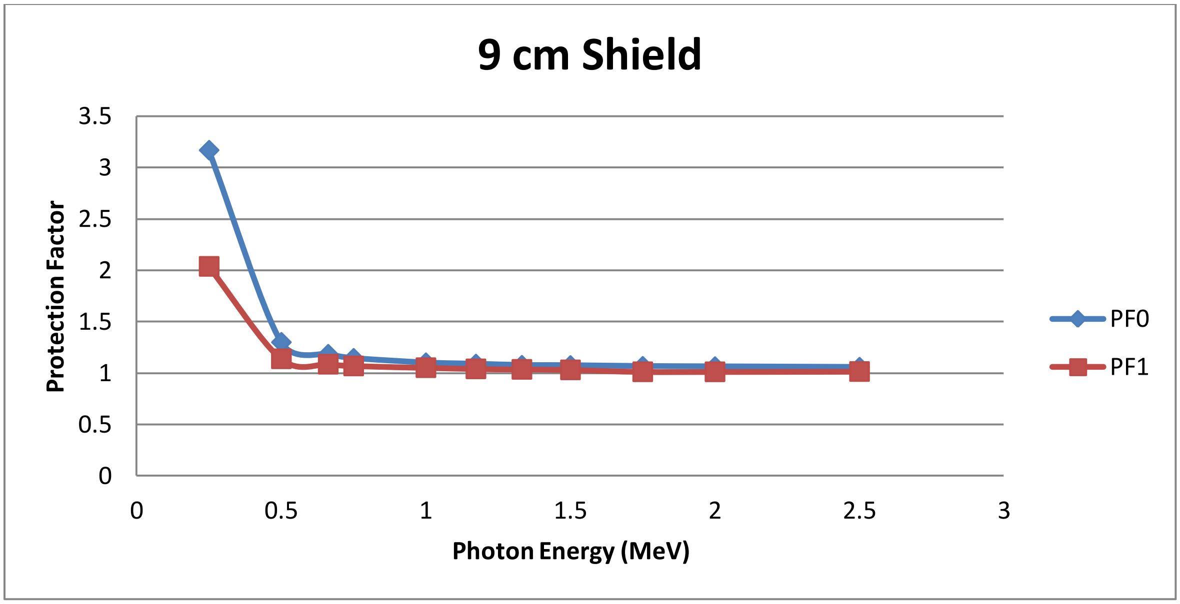

Appendix Figures CC: 9 cm Protection Factor to Photon Energy Curve

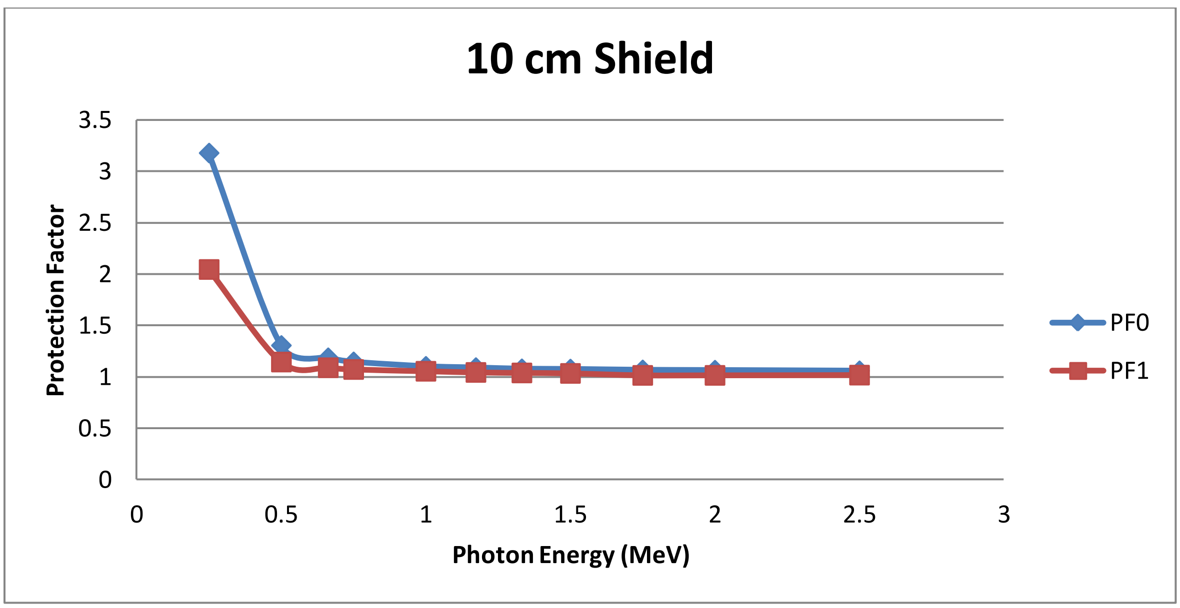

Appendix Figures DD: 10 cm Protection Factor to Photon Energy Curve

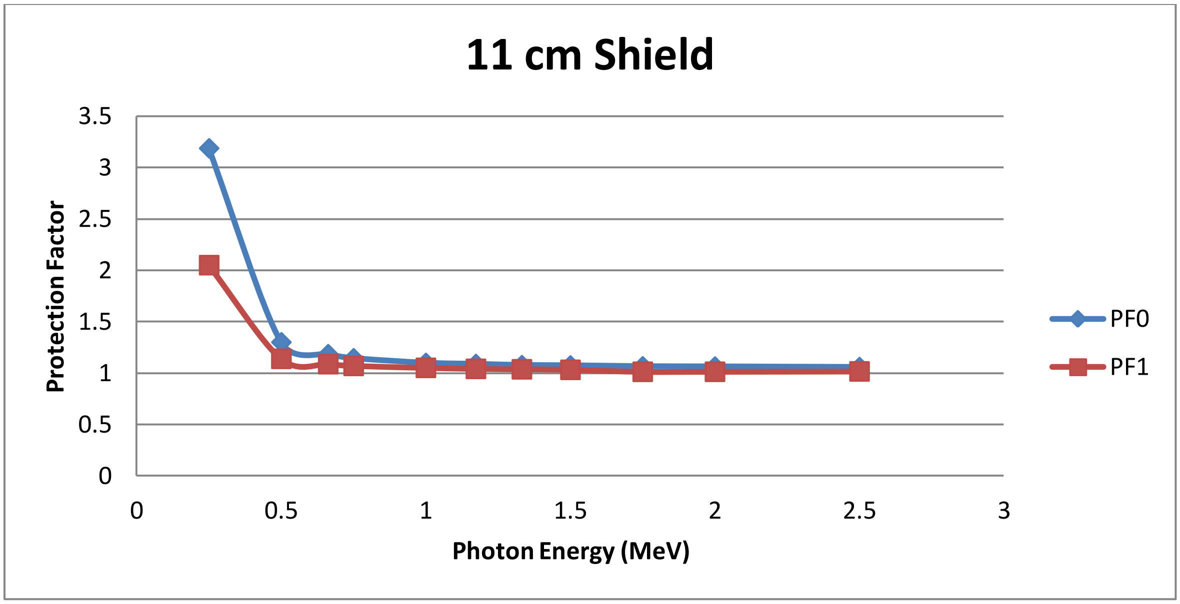

Appendix Figures EE: 11 cm Protection Factor to Photon Energy Curve

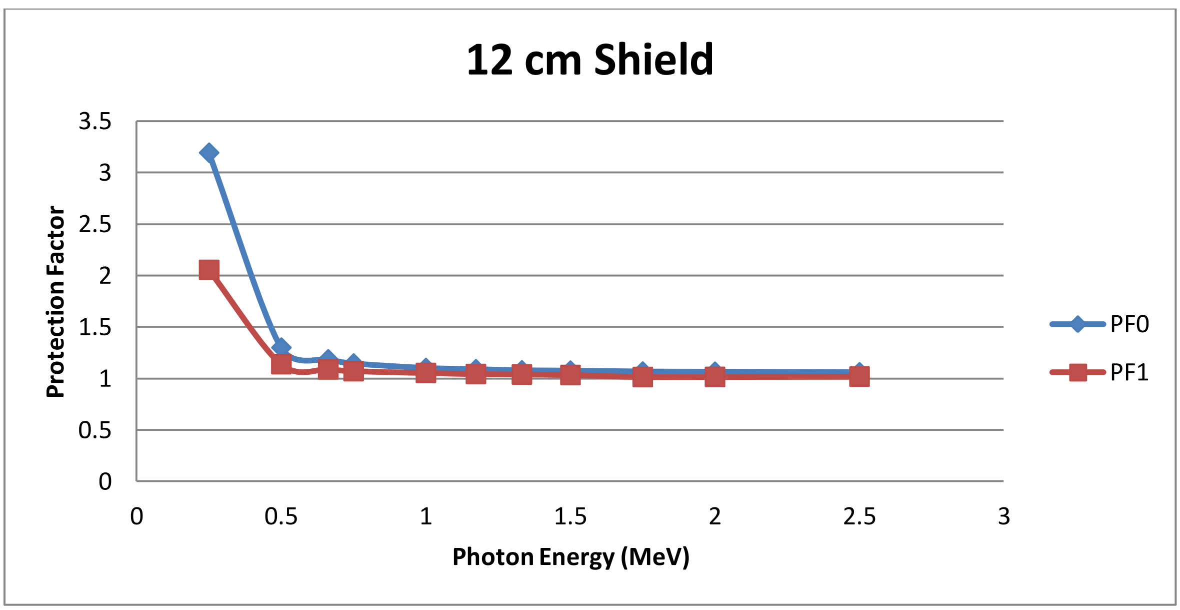

Appendix Figures FF: 12 cm Protection Factor to Photon Energy Curve

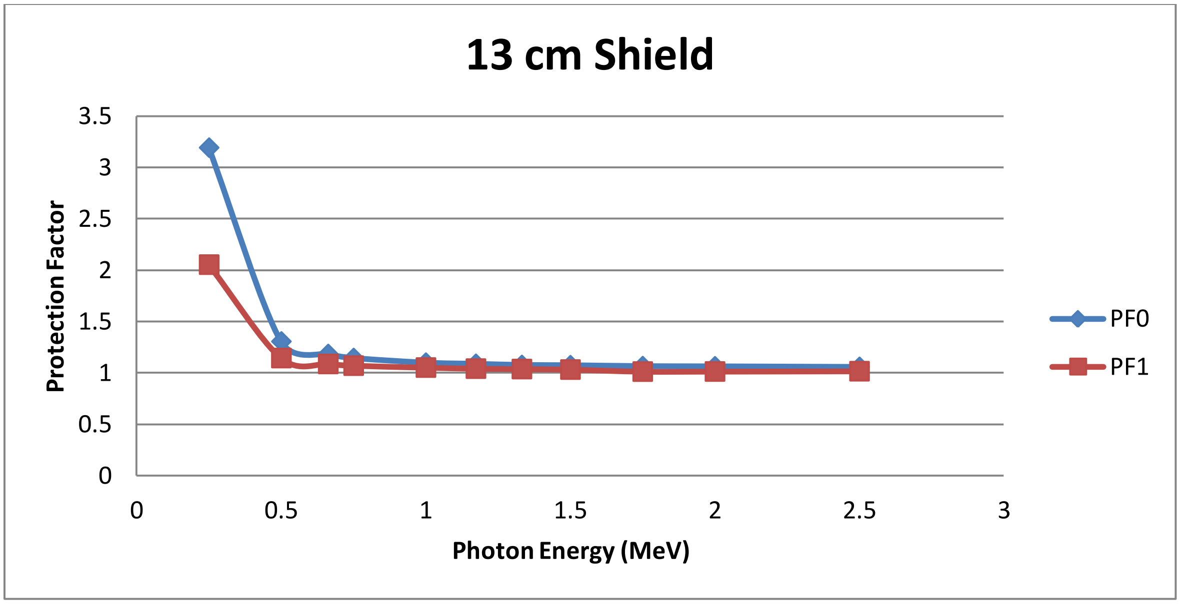

Appendix Figures GG: 13 cm Protection Factor to Photon Energy Curve

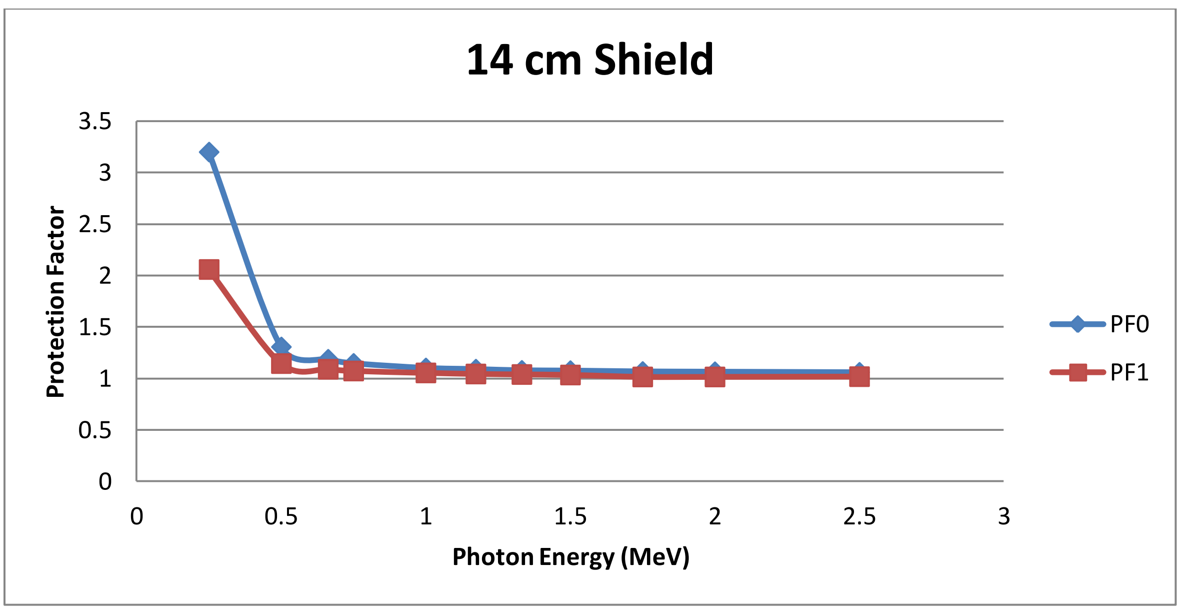

Appendix Figures HH: 14 cm Protection Factor to Photon Energy Curve

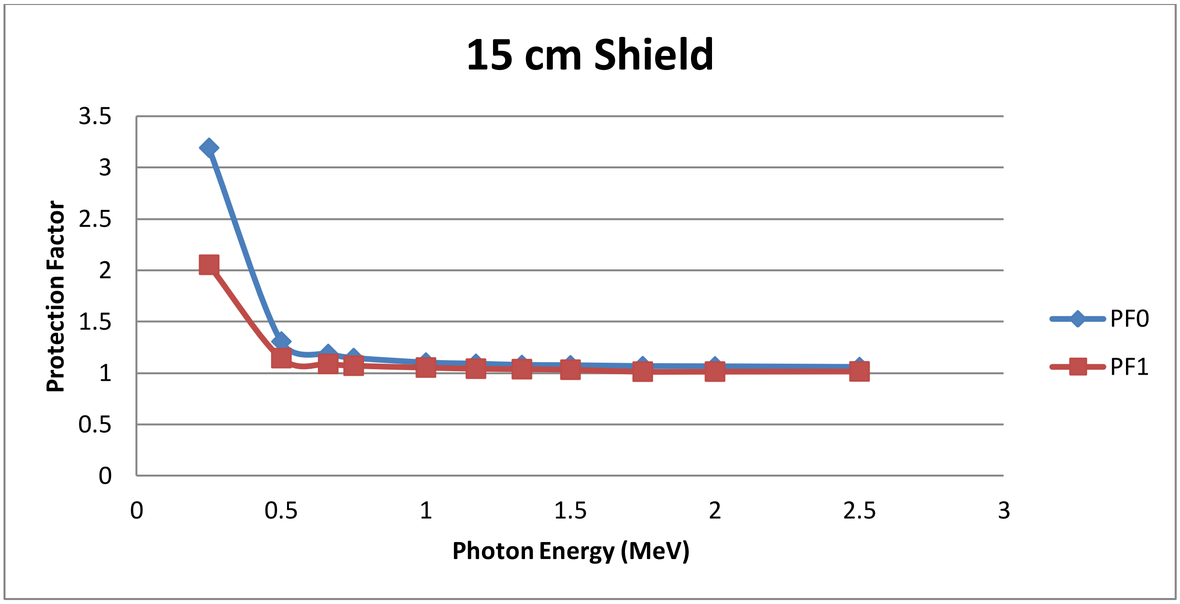

Appendix Figures II: 15 cm Protection Factor to Photon Energy Curve

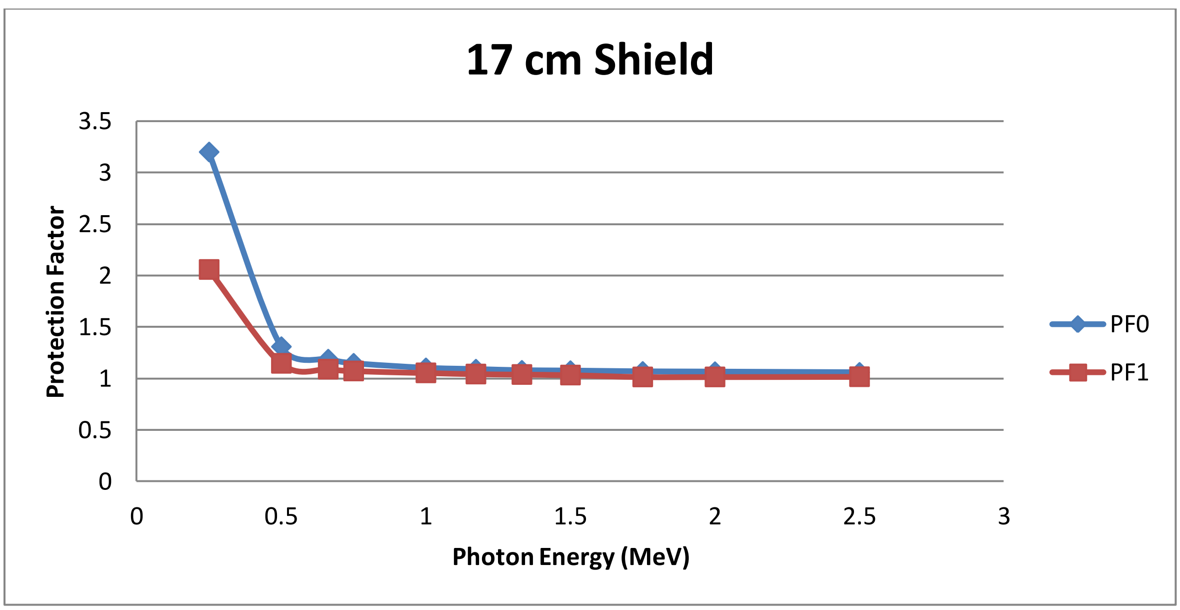

Appendix Figures JJ: 17 cm Protection Factor to Photon Energy Curve

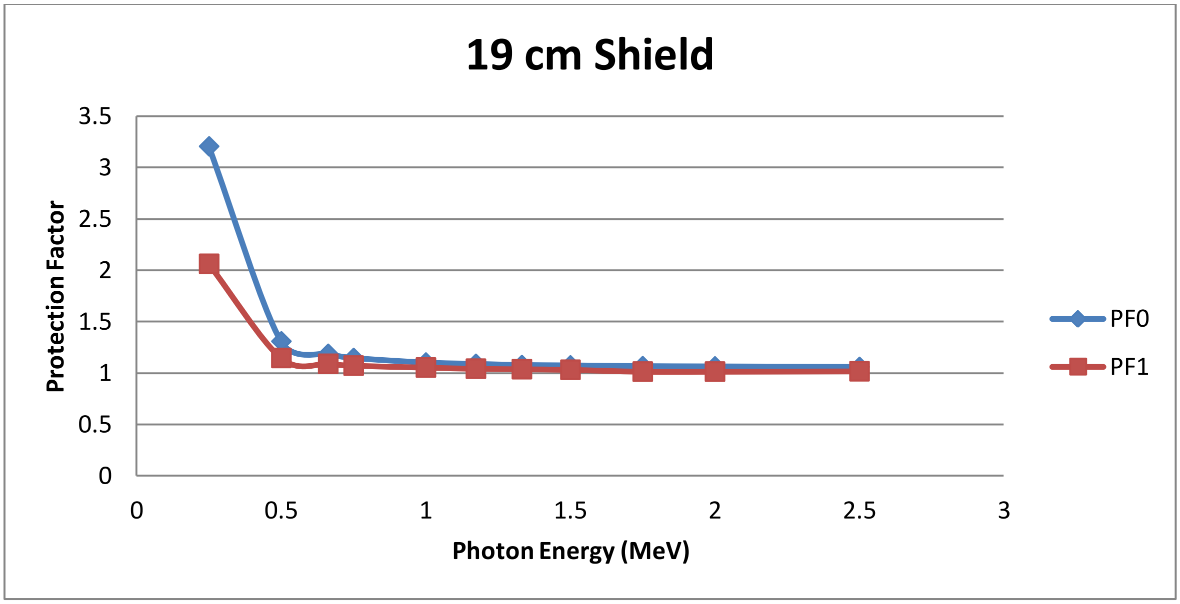

Appendix Figures KK: 19 cm Protection Factor to Photon Energy Curve

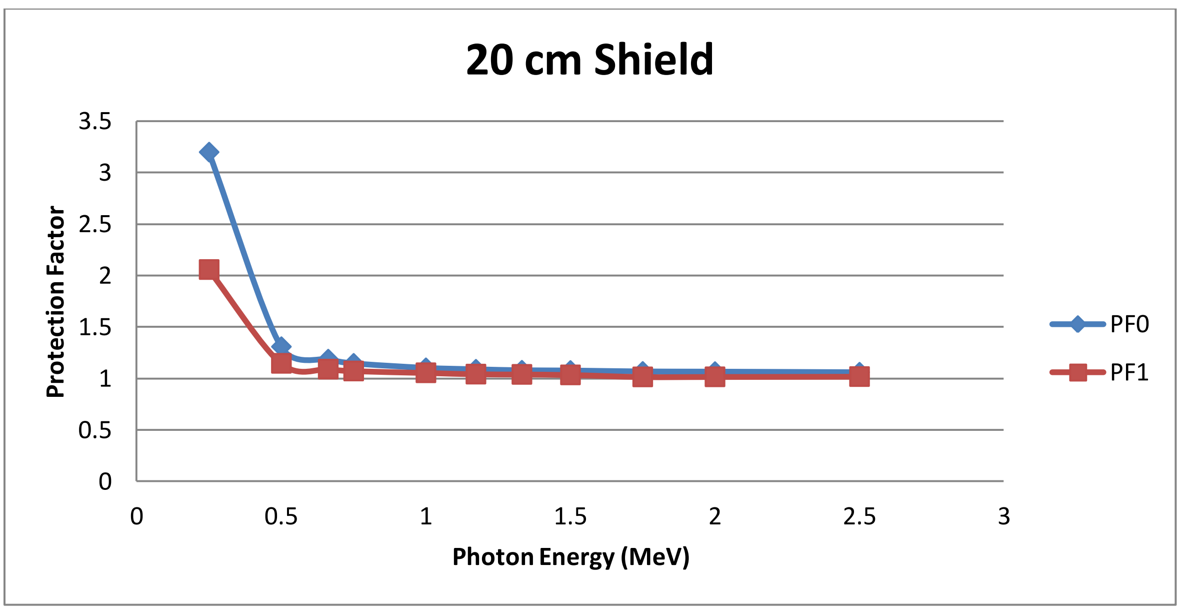

Appendix Figures LL: 20 cm Protection Factor to Photon Energy Curve

APPENDIX E

Protection Factor to Shield Placement Curve

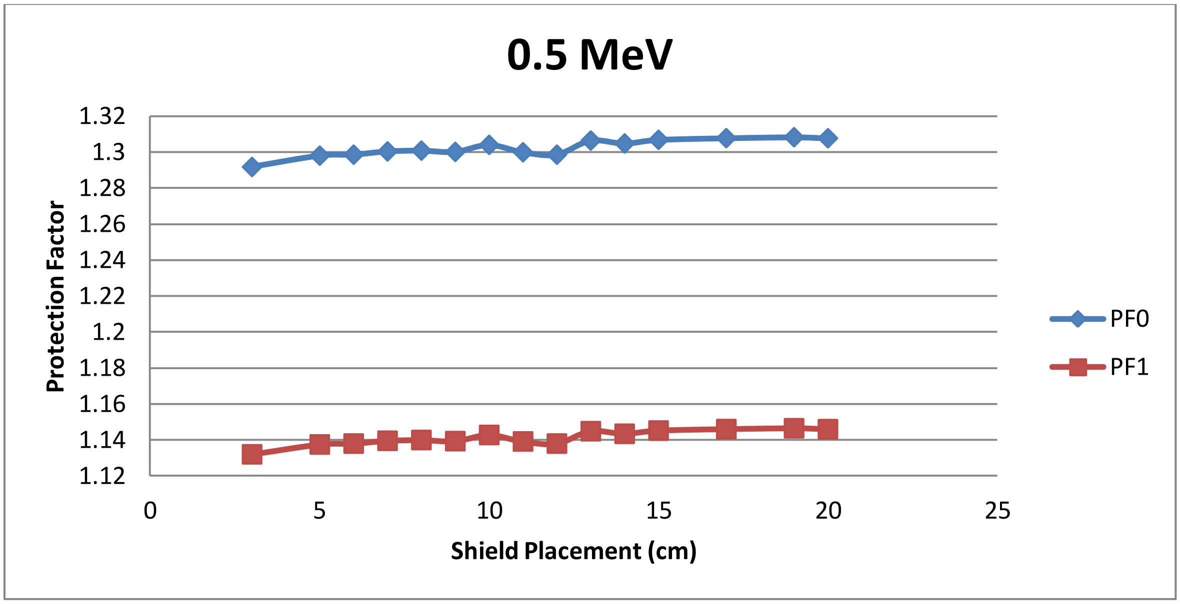

Appendix Figures MM: 0.5 MeV Protection Factor to Shield Placement Curve

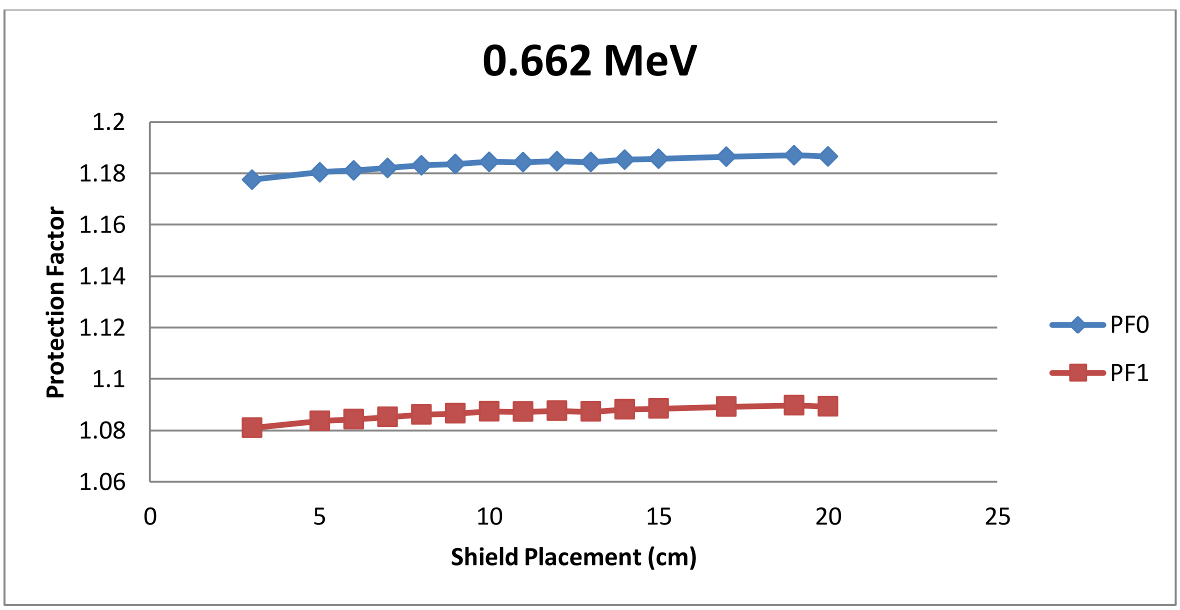

Appendix Figures NN: 0.662 MeV Protection Factor to Shield Placement Curve

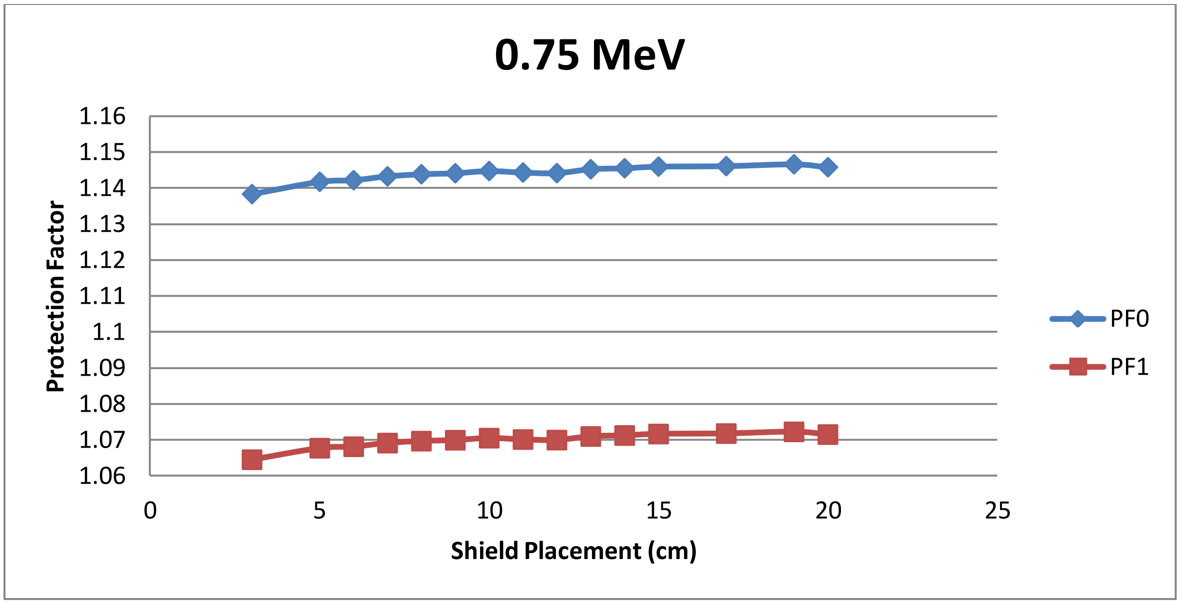

Appendix Figures OO: 0.75 MeV Protection Factor to Shield Placement Curve

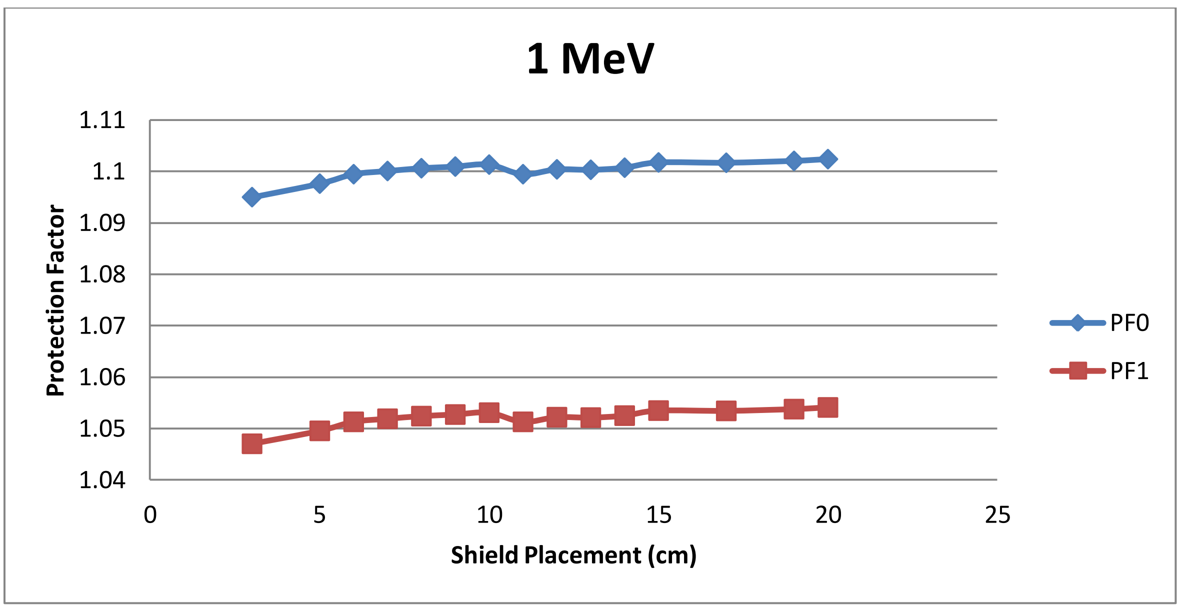

Appendix Figures PP: 1.0 MeV Protection Factor to Shield Placement Curve

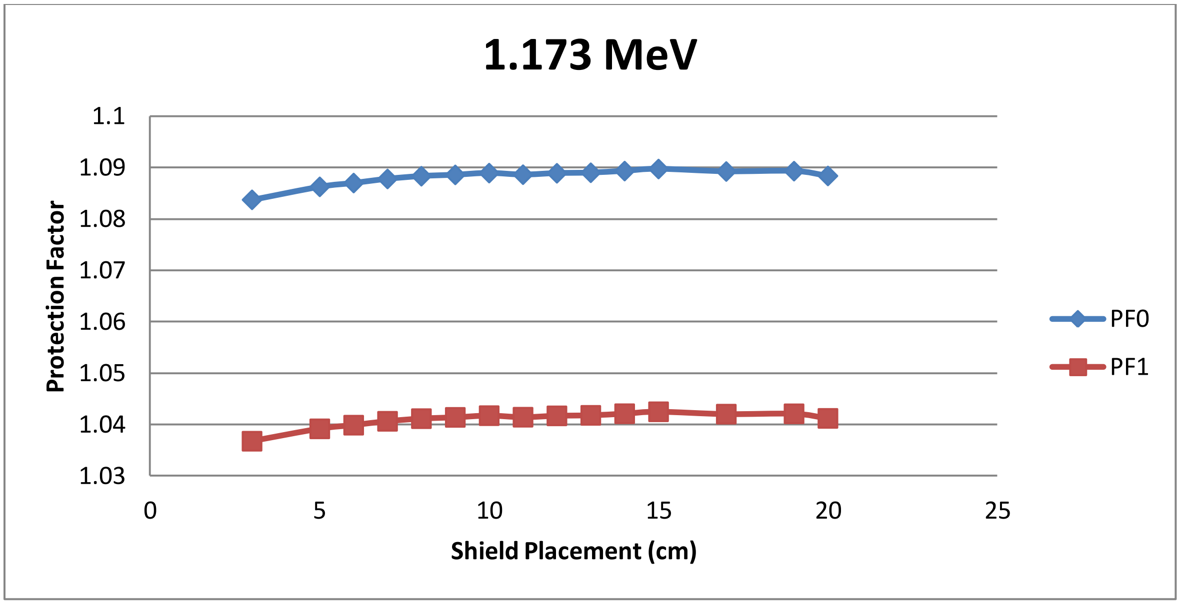

Appendix Figures QQ: 1.173 MeV Protection Factor to Shield Placement Curve

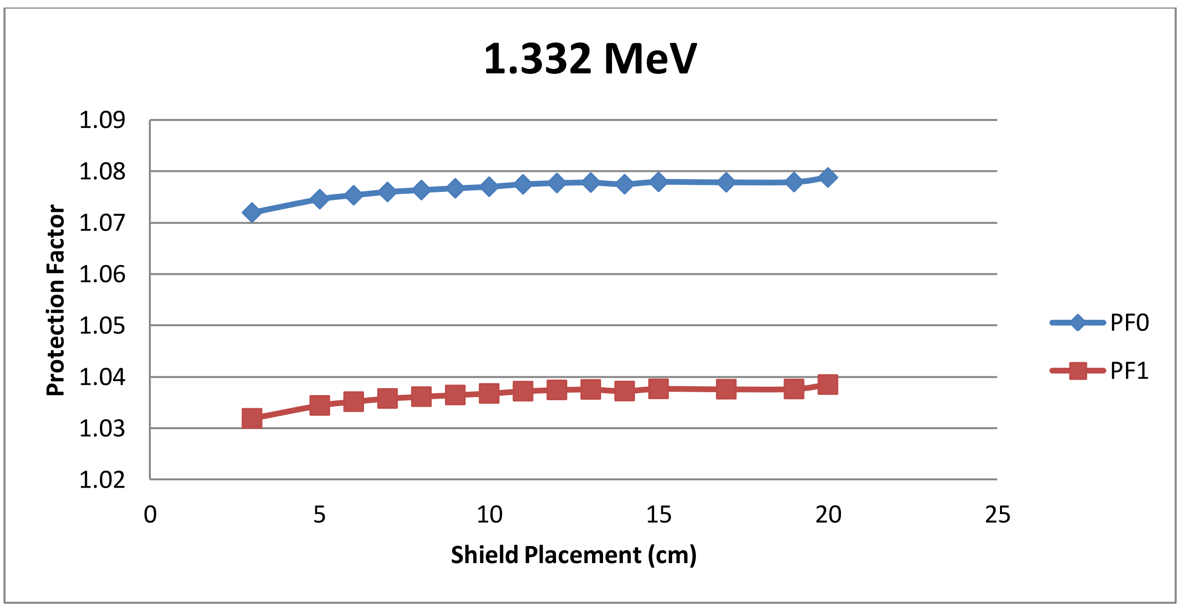

Appendix Figures RR: 1.332 MeV Protection Factor to Shield Placement Curve

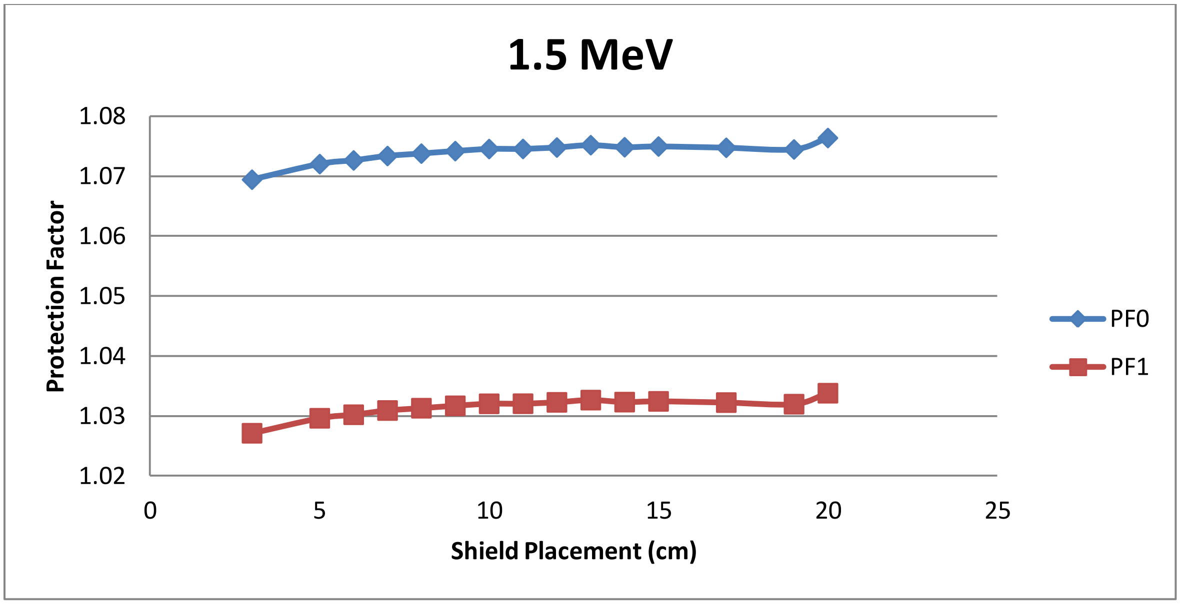

Appendix Figures SS: 1.5 MeV Protection Factor to Shield Placement Curve

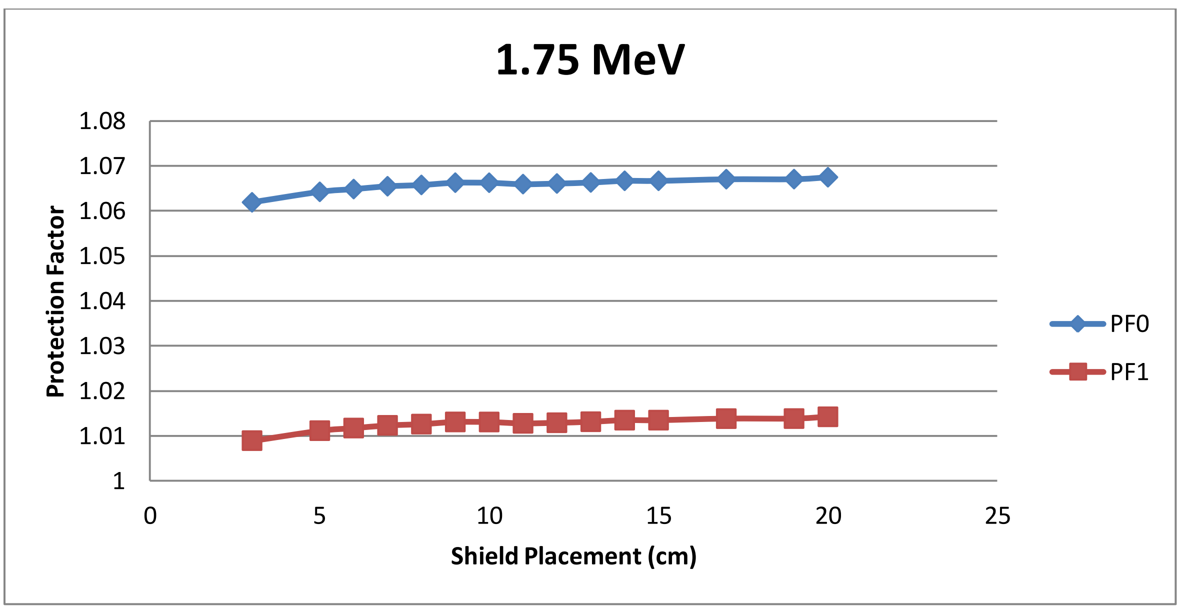

Appendix Figures TT: 1.75 MeV Protection Factor to Shield Placement Curve

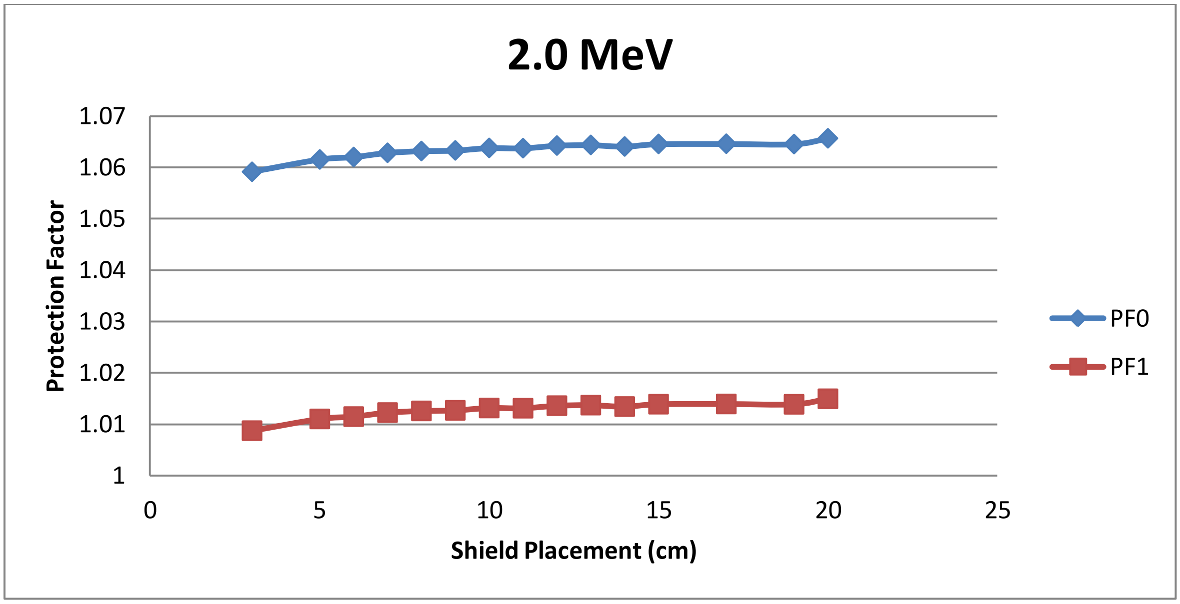

Appendix Figures UU: 2.0 MeV Protection Factor to Shield Placement Curve

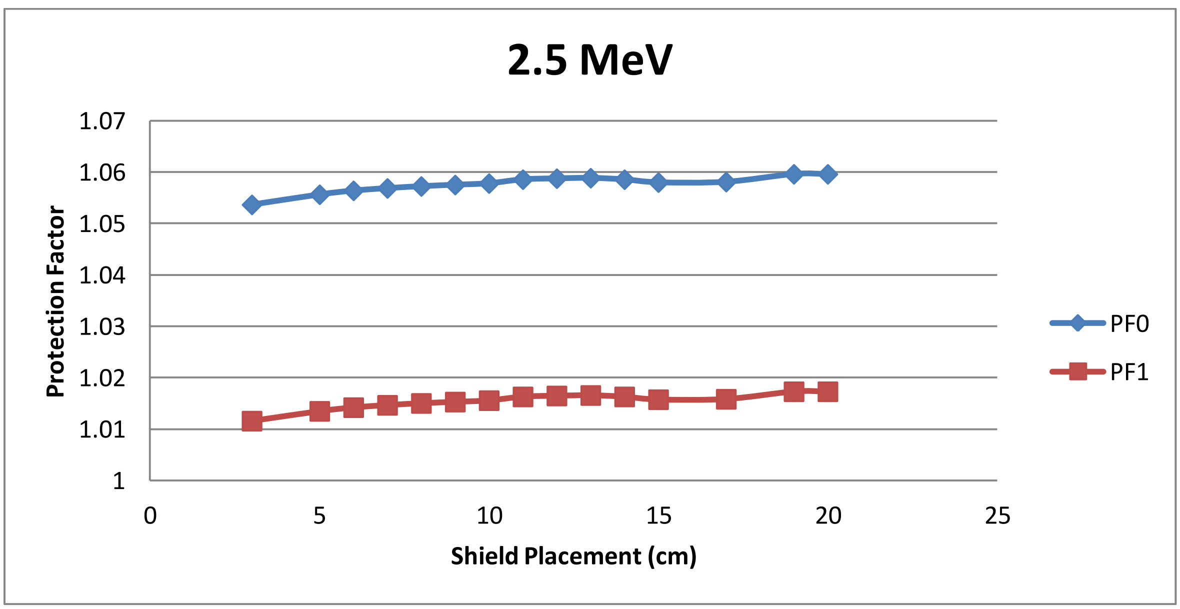

Appendix Figures VV: 2.5 MeV Protection Factor to Shield Placement Curve

APPENDIX F

MCNP Input File

The following MCNP6 input file can be modified to construct an input file for each shield configuration and photon energy. To change the dynamic shield, the user would change the y component of the TR 4 translation card. To change the photon energy, the user would change the ERG component of the SDEF card. Finally, to change the shield thickness to correspond with energy, the user would change the y extent of the macro-body that creates the shield.

```
C Head model based on ORNL phantom - Adult male (Eckerman et al., 1996)
C Cell Cards
C
C Tally Location for Left Eye (400 series)
400    32 -1.00    -400 vol 3.35103E-05
C Tally Location for Right Eye (300 series)
300      32 -1.00   -300 vol 3.35103E-5
C Eyelid
301      35 -1.09  (-311 302 -350):(350 -312 323 -351): &
             (351 -312 321 -352):(352 -313 321 -353 317): &
             (353 -313 317 -354):(354 -314 317 315): &
             (354 -314 317 -320) &
              vol 4.223800000   trcl 1
C
C Sclera
302      34 -1.07   (-301 -302 309):(301 -302 303 -350): &
             (350 -355 -323 303):(355 -351 -323 305): &
             (351 -310 305 -321)  &
              vol 1.072500000   trcl 1
C
C Choroid
303      34 -1.07   (-301 -309 303) &
              vol 0.173730000   trcl 1
C
C Retina
304      34 -1.07   (-301 -303 305):(301 -303 305 -355) &
              vol 0.181100000  trcl 1
C
C Cornea
305      31 -1.06   -317 319 321 &
              vol 0.110140000  trcl 1
C
C Iris
306      34 -1.07   -321 322 307 310 &
              vol 0.213670000  trcl 1
C
C Anterior Chamber
307      32 -1.00   (-319 321):(322 -321 -307 326) #300 &
              vol 0.163500000  trcl 1
C
C Insensitive volume of Lens
308      33 -1.07   -306 -325 -327 &
              vol 0.182930000  trcl 1
C
C Meridional Rows
309      33 -1.07   -318 327 -304 -316 -308 &
              vol 0.020104000  trcl 1
C
C Germinative Zone
310    33 -1.07    -318 324 -326 325 &
```

```
                 vol 0.004227900  trcl 1
C
C Transition Zone
311     33 -1.07     -318 -324 -327 325 &
                 vol 0.004761900  trcl 1
C
C  Central Zone
312     33 -1.07     -318 325 326 &
                 vol 0.003631000  trcl 1
C
C Vitreous Humor
313     32 -1.00     (-305 -310):(310 -322) #308 #309 #310 #311 #312 &
                 vol 4.403500000  trcl 1
C
C Eyelid
401     35 -1.09     (-411 402 -450):(450 -412 423 -451): &
                (451 -412 421 -452):(452 -413 421 -453 417): &
                (453 -413 417 -454):(454 -413 417 415): &
                (454 -413 417 -420) &
                 vol 4.146900000   trcl 2
C
C Sclera
402     34 -1.07     (-401 -402 409):(401 -402 403 -450): &
                (450 -455 -423 403):(455 -451 -423 405): &
                (451 -410 405 -421) &
                 vol 1.069900000   trcl 2
C
C Choroid
403     34 -1.07     (-401 -409 403) &
                 vol 0.173140000   trcl 2
C
C Retina
404     34 -1.07     (-401 -403 405):(401 -403 405 -455) &
                 vol 0.181150000   trcl 2
C
C Cornea
405     31 -1.06     -417 419 421 &
                vol 0.109460000   trcl 2
C
C Iris
406     34 -1.07     -421 422 407 410 &
                 vol 0.214940000   trcl 2
C
C Anterior Chamber
407     32 -1.00     (-419 421):(422 -421 -407 426) #400 &
                 vol 0.163750000  trcl 2
C
C Insensitive volume of Lens
408     33 -1.07     -406 -425 -427 &
                 vol 0.182250000  trcl 2
C
```

```
C Meridional Rows
409     33 -1.07     -418 427 -404 -416 -408 &
                vol 0.020234000  trcl 2
C
C Germinative Zone
410     33 -1.07     -418 424 -426 425 &
                vol 0.004121800  trcl 2
C
C Transition Zone
411     33 -1.07     -418 -424 -427 425 &
                vol 0.004522700  trcl 2
C
C  Central Zone
412     33 -1.07     -418 425 426 &
                vol 0.003696400  trcl 2
C
C Vitreous Humor
413     32 -1.00     (-405 -410):(410 -422) #408 #409 #410 #411 #412 &
                vol 4.387900000  trcl 2
C
C Area in front of Right Eye
600     2 -0.001205   #65 -600 601 -602 &
      #301 #302 #303 #304 #305 #306 #300 #307 #308 #309 #310 #311 #312 #313 &
      #501 &
                trcl 1 vol 19.466
C
C Area in front of Left Eye
700     2 -0.001205   #65 -600 601 -602 &
      #401 #402 #403 #404 #405 #406 #400 #407 #408 #409 #410 #411 #412 #413 &
      #501 &
                trcl 2 vol 19.466
C
C
C Outside of Phantom
5        2 -0.001205 #301 #305 #307 #401 #405 #407 #600 #700 &
      (9 -10 14 22 -12 2 -15 #65 #501 #502):(-22 21 9 -10 2 -15 #65 #501 &
      #502):(-21 2 -6 2 #65 #501 #502):(12 24 -15 9 -10 #65 #501 #502) &
      (2:7:-8:9:-10:-15 #65 #501 #502) &
               trcl 3
C
C Head and Neck
6        3 -1.04 ((-23 6 -22 114)):(-21 22 -622 114):((622 -12 -18 116) &
      #41 #43 #17 #301 #302 #313 #303 #304 #306 #401 #402 #403 #404 &
      #413 #406 #305 #300 #307 #308 #309 #310 #311 #312 #405 #400 #407 #408 &
      #409 #410 #411 #412 #412 #600 #700):((-524 12 116) #43 #42) &
                trcl 3 vol 2518.7
C
C Skin
7        3 -1.04 (-21 23 6 -22):(22 -622 21 -14):(-14 18 622 -12 #301 #302 &
      #303 #304 #305 #306 #300 #307 #308 #309 #310 #311 #312 #313 #401 #402 &
      #403 #404 #405 #406 #400 #407 #408 #409 #410 #411 #412 #413 #600 &
```

```
        #700):(12 -24 524) #600 #700 &
                trcl 3 vol 313.75
C
C Brain
17      3 -1.04      -45 &
                trcl 3 vol 1366.9
C
C Spine
41      5 -1.4       (6 -113 -114) &
                trcl 3 vol 232.4
C
C Skull-Cranium
42      5 -1.4 (-116 45 12 ):(-116 45 -12) &
                trcl 3 vol 617.67
C
C Facial Skeleton
43      5 -1.4       (118 -117 120 -121 -119 116 #301 #302 &
               #303 #304 #305 #306 #300 #307 #308 #309 &
               #310 #311 #312 #313 #401 #402 #403 #404 #405 #406 #400 &
               #407 #408 #409 #410 #411 #412 #413 ) &
                trcl 3 vol 170.84
C
C Faceplate Shield
501    82  -6.22    -501
C
502    LIKE 501 BUT  trcl 4
C
C Graveyard
65      0           -2:-7:8:-9:10:15   &
               trcl 3
C end of cell Cards

C Surface Cards for Stylized Head Model
600   ky   -4.500  0.0717967697 1
601   py    0.900
602   py    3.000
C
2     pz   69.000                                              $Universe Boarder
6     pz   70.000
7     px  -30.000                                              $Universe Boarder
8     px   30.000                                              $Universe Boarder
9     py  -75.000                                              $Universe Boarder
10    py   15.000                                              $Universe Boarder
12    pz   91.450
14    sq  100.000 64 0 0 0 0 -6400 0 0 0                       $head1-skin
15    pz  100.000                                              $Universe Boarder
18    sq   96.040 60.84 0 0 0 0 -5843.0736 0 0 0               $head1
21    cz    5.400
22    pz   78.400
622   pz   78.600
23    cz    5.200                                              $neck
```

```
24    sq 5112.250 3271.84 6400 0 0 0 -327184 0 0 91.45                          $head2
524   sq 4638.172 2938.72 5843.074 0 0 0 -282235.1 0 0 91.45                    $head2
45    sq 2445.3025 1440.2025 3221.6976 0 0 0 -106517.3769 0 0 91.45             $brain
C 37 pz    43.000
113   pz   84.800
114   sq    6.250 4 0 0 0 0 -25 0 1.45 0                                         $spine-upper
C  45 sq 2445.3025 1440.2025 3221.6976 0 0 0 -106517.3769 0 0 91.45             $skull-cranium
116   sq 3991.080625 2487.515625 5076.5625 0 0 0 -224498.28515625 0 0 91.45     $skull-cranium
117   sq   81.000 49 0 0 0 0 -3969 0 0 0                                         $facial skeleton
118   sq   57.760 31.36 0 0 0 0 -1811.3536 0 0 0                                 $facial skeleton
C 80 sq 5112.25 3271.84 6400 0 0 0 -327184 0 0 91.45          $the statements defining cranium
119   py    0.000
120   pz   82.400
121   pz   93.130
C
C Surface Cards for Stylized Eye Model
C Tally Locations
300   S    -3.000 -0.941 0.000  0.020
400   S     3.000 -0.941 0.000  0.020
C Eye Surfaces
301   PY    0.024
302   SO    1.174
303   SY    0.048  1.074
304   SY    0.759  0.5
305   SY    0.098  1.074
306   SY    1.291  0.8
307   CY    0.150
308   SY    1.0364012305223 0.6
309   SO    1.074
310   PY    0.42022
311   SO    1.399
312   SY    0.080  1.399
313   SY   -0.380  1.575
314   SY    0.466  1.000
315   P     0.000 -5.870  8.090 -2.18462
316   SY    0.433747228596   0.595
317   SY    0.466  0.775
318   SY   -0.339  1.25
319   SY    0.466  0.72
320   P     0.000  4.226 14.463 -2.75194
321   SY   -0.380  1.35
322   SY   -0.380  1.3
323   SY    0.080  1.174
324   PY    0.850
325   SY   -0.359  1.25
326   PY    0.8775
327   SY    0.759  0.45
350   PY    0.040
351   PY    0.33285
352   PY    0.418939130435   $ Intersection of 12 and 13
353   PY    0.76515
```

```
354   PY    0.918073877068558
355   PY    0.073
C
401   PY    0.024
402   SO    1.174
403   SY    0.048  1.074
404   SY    0.759  0.500
405   SY    0.098  1.074
406   SY    1.291  0.800
407   CY     0.150
408   SY    1.0364012305223  0.6
409   SO    1.074
410   PY    0.42022
411   SO    1.399
412   SY    0.080  1.399
413   SY   -0.380  1.575
414   SY    0.466  1
415   P    0.000 -5.870  8.090 -2.18462
416   SY    0.433747228596   0.595
417   SY    0.466  0.775
418   SY   -0.339  1.250
419   SY    0.466  0.720
420   P    0.000  4.226  14.463 -2.75194
421   SY   -0.380  1.350
422   SY   -0.380  1.300
423   SY    0.080  1.174
424   PY    0.850
425   SY   -0.359  1.250
426   PY    0.8775
427   SY    0.759  0.450
450   PY    0.040
451   PY    0.33285
452   PY    0.418939130435   $ Intersection of 12 and 13
453   PY    0.76515
454   PY    0.918073877068558
455   PY    0.073
501   BOX   -29 -3.1 -14  58 0 0  0 -0.15300243 0  0 0 27
C End Surface Cards

C Translation to put eye in correct place
IMP:p,e  1 38r 0
Area     0.0050265 1r
tr1 -3  0    0      1 0 0  0 -1 0  0 0 1
tr2  3  0    0      1 0 0  0 -1 0  0 0 1
C Translation to move head into alignment with eye
tr3  0  8  -85.5    1 0 0  0  1 0  0 0 1
C
C Translation to place shield 2
tr4  0  -5  0       1 0 0  0  1 0  0 0 1  1
C Material Cards
C
```

```
C Air (Dry, Near Sea Level) From Compendium
M2     6000  -0.000124
       7000  -0.755268    $ density=0.001205 g/cm3
       8000  -0.231781
      18000  -0.012827
C Soft tissue, from ORNL phantom - Adult male (Eckerman et al., 1996)
M3     1000   0.10454
       6000   0.22663
       7000   0.02490
       8000   0.63525
      11000   0.00112
      12000   0.00013
      14000   0.00030
      15000   0.00134
      16000   0.00204
      17000   0.00133
      19000   0.00208
      20000   0.00024
      26000   0.00005
      30000   0.00001
      40000   0.00001
C Skeleton, from ORNL phantom - Adult male (Eckerman et al., 1996)
M5     1000   0.07337
       6000   0.25475
       7000   0.03057
       8000   0.47893
       9000   0.00025
      11000   0.00326
      12000   0.00112
      14000   0.00002
      15000   0.05095
      16000   0.00173
      17000   0.00143
      19000   0.00153
      20000   0.10190
      26000   0.00008
      30000   0.00005
      37000   0.00002
      38000   0.00003
      82000   0.00001
C Cornea, den=1.06
M31    1000  -10.3    $ Hydrogen
       6000  -10.9    $ Carbon
       7000  -03.5    $ Nitrogen
       8000  -75.1    $ Oxygen
      16000  -00.2    $ Sulfur
C
C Anterior Chamber, Vitreous Humour, den=1.00
M32    1000  -11.2    $ Hydrogen
       8000  -88.8    $ Oxygen
C
```

```
C Lens, den=1.07
M33    1000  -09.06   $ Hydrogen
       6000  -19.5    $ Carbon
       7000  -05.7    $ Nitrogen
       8000  -64.6    $ Oxygen
      11000  -00.1    $ Sodium
      15000  -00.1    $ Phosphorous
      16000  -00.3    $ Sulfur
      17000  -00.1    $ Chlorine
C
C Retina, Choroid, Sclera den=1.07
M34    1000  -10.0    $ Hydrogen
       6000  -14.6    $ Carbon
       7000  -04.5    $ Nitrogen
       8000  -70.6    $ Oxygen
      16000  -00.3    $ Sulfur
C
C Eye Lid, den=1.09
M35    1000  -10.0    $ Hydrogen
       6000  -19.9    $ Carbon
       7000  -00.42   $ Nitrogen
       8000  -65.0    $ Oxygen
      11000  -00.2    $ Sodium
      15000  -00.1    $ Phosphorous
      16000  -00.2    $ Sulfur
      17000  -00.3    $ Chlorine
      19000  -00.1    $ Potassium
C
C Leaded Glass
M82    8000    0.156453 $Oxygen    6.22 g/cm3
      14000    0.080866 $Silicon
      22000    0.008092 $Titanium
      33000    0.002651 $Arsenic
      82000    0.751938 $Lead
C Source Cards
C
mode P E
SDEF  PAR=P ERG=0.5 POS 0 -25 0 VEC -3 24.059 0 DIR=D1   $5degreesfrom (0,-25,0) to (-3,-.941,0)
SI1 -1.00 0.9961946981   1.00
SP1  0.00 0.998097349 0.001902650954
SB1  0.00 0   1.00
C Tally Cards
C
C F5 Tally
F5:p       -3 -0.941 0 0.02
DE5 0.01 0.015 0.02 0.03 0.04 0.05 0.06 0.08 0.1 0.15 0.2 &
0.3 0.4 0.5 0.6 0.8 1.0 1.5 2.0 3.0 4.0 5.0 6.0 8.0 10.0
DF5 7.43e-10 3.12e-10 1.68e-10 0.721e-10 0.429e-10 &
0.323e-10 0.289e-10 0.307e-10 0.371e-10 0.599e-10 &
0.856e-10 1.38e-10 1.89e-10 2.38e-10 2.84e-10 &
3.69e-10 4.47e-10 6.14e-10 7.55e-10 9.96e-10 &
```

```
12.1e-10 14.1e-10 16.1e-10 20.1e-10 24.0e-10
C F25:P       -3 -0.941 0 0.02
C FM25        1.606725e-11 32 -5 -6 $Gy/source particle
C
C
C F6 Tally
C +F6        308 309 310 311 312 T
C FM6        1.60218e-10
C
NPS        1e7                       $run for 1e7 histories
PRDMP      1000000                   $print dump, updates output every 10000 particles
C STOP F5 0.005 NPS 1e8     $stop run when F5 tally reaches relative error of .5% or 1e8 histories
completed
C ctme 5000                           $Run until 5000 minutes
C Exponential Transform
EXT:p     0.7V1
VECT      V1 -3 -0.941 0
C
C Weight Windows
C WWG        5 0 0 J J J J 0      $Tally Number, 0 for MESH, 0 for 1/2 source weight, 0 for energy bins
WWP:P      4J -1                     $weight-window bounds are to be obtained from a file
MESH
      ref 0 -25 0
C     origin -33 -70 -17
C     axs 0 0 1
C     vec 0 1 0
C     IMESH 33
C     IINTS 75
C     JMESH 26
C     JINTS 75
C     KMESH 16
C     KINTS 75
```